

NUMERICAL STUDY OF FLUID FLOW AND HEAT TRANSFER IN RETICULATED POROUS MEDIA

Thesis

Submitted in partial fulfilment of the requirement for the degree of

DOCTOR OF PHILOSOPHY

by

SIDDAM RAMBABU

(Reg. No. 187111ME022)



**DEPARTMENT OF MECHANICAL ENGINEERING
NATIONAL INSTITUTE OF TECHNOLOGY KARNATAKA
SURATHKAL, MANGALORE – 575025**

AUGUST, 2023

**NUMERICAL STUDY OF FLUID FLOW
AND HEAT TRANSFER IN
RETICULATED POROUS MEDIA**

Thesis

Submitted in partial fulfilment of the requirement for the degree of

DOCTOR OF PHILOSOPHY

by

SIDDAM RAMBABU

(Reg. No. 187111ME022)

Under the guidance of

Dr PARTHASARATHY P

Assistant Professor



**DEPARTMENT OF MECHANICAL ENGINEERING
NATIONAL INSTITUTE OF TECHNOLOGY KARNATAKA
SURATHKAL, MANGALORE – 575025**

AUGUST, 2023

DECLARATION

I hereby declare that the Research Thesis entitled “**NUMERICAL STUDY OF FLUID FLOW AND HEAT TRANSFER IN RETICULATED POROUS MEDIA**” which is being submitted to the **National Institute of Technology Karnataka, Surathkal** in partial fulfillment of the requirements for the award of the degree of **Doctor of Philosophy in Mechanical Engineering** is a *bonafide report of the research work carried out by me*. The material contained in this thesis has not been submitted to any University or Institution for the award of any degree.

Register Number: **187111ME022**

Name of the Research Scholar: **SIDDAM RAMBABU**

Signature of the Research Scholar: 

Department of Mechanical Engineering

Place: NITK, Surathkal

Date: 22 | 08 | 2023

CERTIFICATE

This is to certify that the Research Thesis entitled “NUMERICAL STUDY OF FLUID FLOW AND HEAT TRANSFER IN RETICULATED POROUS MEDIA” submitted by Mr. SIDDAM RAMBABU (Register Number: 187111ME022) as the record of the research work carried out by him, *is accepted as the Research Thesis submission* in partial fulfilment of the requirements for the award of the degree of **Doctor of Philosophy**.

Research Guide

P. Parthasarathy 22/8/2023
Dr. PARTHASARATHY P

Assistant Professor
Department of Mechanical Engineering

Dr. H. C. W. 22.8.2023

Chairman-DRPC

Department of Mechanical Engineering
National Institute of Technology Karnataka
Surathkal, Mangalore - 575025



Dedicated to My beloved Parents

ACKNOWLEDGEMENT

A guru is someone who genuinely cares for their disciples without any selfish motives. He cares far more about the disciple than parents, who typically overlook the highest good in their haste to provide their kids with material comfort. I would bestow sincere thanks to my supervisor **Dr. Parthasarathy P**, for giving me this excellent chance to pursue a **Ph.D**. The interest, guidance, encouragement and academic insight of my advisor has been invaluable over the last four years. He has been very generous with his time and energy, and I have learnt enormous information from him. I have been privileged to work with him and I am extremely grateful to him.

My deepest gratitude to **Dr. Ratna Kishore V**, Associate Professor, Department of Mechanical Engineering, at Amrita Vishwa Vidyapeetham (Amrita University), Coimbatore, for providing necessary support and words of advice.

I am incredibly grateful to our honourable director **Prof. B Ravi**, for creating an attitude towards research for students. I sincerely thank our HOD **Prof. Ravikiran Kadoli**, for providing all facilities needed during research work. I would also like to thank RPAC members, **Dr. Arun M**, Associate Professor, Department of Mechanical Engineering and **Dr Rajasekaran B**, Assistant Professor, Department of Metallurgical and Materials Engineering, for providing valuable suggestions and extending support to me on aspects of completing this work. I also thank the secretary of DRPC, **Dr. Vasudeva Madav**, for helping in the smooth conduct of the presentations. I am thankful to all the Deans of NITK for providing facilities at NITK Surathkal.

Words cannot explain my gratitude to my mother **Smt. Padma S** for supporting me and her blessings helped me in my research work. I would also like to thank my elder brother **Mr Srinivas Rao S** and an elder sister-in-law **Smt. Subhashini** for taking

care of my parents during my stay in NITK, and elder sister **Mrs. Siva Kumari** and brother-in-law **Mr. Purna Chandra Rao** and their families for supporting me in my work and making my research process a pleasant one. I am incredibly thankful to my father-in-law **Shri. Durga Venkata Reddy** and mother-in-law **Smt. Chandra Kumari** for believing in me and encouraging me to pursue my passion.

My special thanks to my wife **Mrs. Sravani** for her valuable patience and constant support during my research time and lots of love to my kids **Praharshitha** and **Sahasra**.

I am grateful to the members of our research group **Sushanth, Shyam Raj, Ashok Patel**, for their unwavering support throughout my PhD studies. My heartfelt thanks to my close friends in NITK, **Ramprasad, Venkatapathy, Ashok Chakravarthy, Ramesh, Madan, Ganesh, Phani, Muthamil, Shane Gowd, Vikas Kumar** and list seems to be endless. I am extremely thankful to the department of Mechanical Engineering, NITK, Faculty and non- teaching staff, for providing all the facilities to carry out my research work. I want to thank all the other security, health care centre, quarters, and physical education and sports department.

I would like to thank all my relatives and friends who have who supported me in one way or the other and their best wishes were always there for me.

This thesis is specially dedicated to my beloved father Late **Shri. BUTCHIAIAH SIDDAM**.

I am blessed to pursue my education in National Institute of Technology Karnataka, Surathkal, which gave me immense exposure towards research and way of thinking and believing. Finally, I want to thank all those who helped me directly or indirectly at various stages of this research work.

SIDDAM RAMBABU

ABSTRACT

The transport of heat and mass in porous media have a significant influence on a wide range of engineering applications such as solar reactors, building thermal insulation, packed cryogenic microsphere insulation, combustors, chemical and biological reactors, etc. The reticulated porous media are heterogeneous systems consisting of several interconnected solid phases with continuous void/fluid space. It is well acknowledged that more efficient heat transfer technologies and novel materials are required to improve performance of energy and heat transfer devices while maintaining tolerable levels of power consumption, size, and cost. Reticulated porous structures are excellent candidates for enhancing the thermal efficiency of heat transfer devices while simultaneously enabling the use of smaller and lighter equipment. The present research work involved in studying the fluid flow, heat and mass transfer in open-cell reticulated porous structures with help of Direct Pore Level Simulations (DPLS). The reticulated porous structures are modelled based on the theoretical Kelvin model. The geometry of these structures are generated with the help of in-house code and visualisation tool kit (VTK) libraries. The ideal and randomized Kelvin structures are generated for different PPI & porosities. By varying the geometrical parameters, the influence of geometries on pressure drop, dispersion, and heat transfer between the flowing fluid and solid phase of open-cell foams are investigated. For this reason, the mass, momentum and energy equations in reticulated structures are solved using the standard CFD-FVM approach.

The simulation results are used to acquire the pressure drop across the structures. The pressure drop variation with respect to pore density, porosity, specific surface area, and randomization are analyzed. The fluid transport properties such as permeability and drag coefficient are calculated for various porous structures and a pressure drop

correlation with new values of viscous and inertial coefficients is proposed. Along with the fluid flow, the dispersion of a tracer is traced across the structures and analysed in terms of the effective diffusivity coefficient. Then the influence of dispersion on mass transfer is characterized by estimating the longitudinal dispersion coefficient. The effect of tortuosity on dispersion is also studied. The characteristic length dependent correlation is proposed in terms of strut diameter and flow tortuosity to relate the longitudinal Peclet number as a function of molecular Peclet number. Subsequent simulations are performed to evaluate the forced convective heat transfer coefficient for different fluids of Prandtl numbers (air, water & seawater). Based on the simulation outcomes, two new correlations are proposed to calculate the heat transfer coefficients in the reticulated porous structures. The proposed correlation is validated by comparing it with numerical and experimental data of real reticulated porous structures available in the literature.

Keywords: Open-cell foams, Kelvin cell model, Randomization, Direct pore level simulation, Pressure drop, Longitudinal dispersion coefficient, Tortuosity, Heat transfer, Forced convection, Generalized empirical correlations.

TABLE OF CONTENTS

ACKNOWLEDGEMENT	i
ABSTRACT	iii
LIST OF TABLES	ix
LIST OF FIGURES	xi
NOMENCLATURE	xv
1 INTRODUCTION	1
1.1 Background about idealized perodic open-cell foam structures . . .	4
1.2 Reticulated porous media characterization	7
1.2.1 Porosity	7
1.2.2 Pore density	8
1.2.3 Pore diameter	8
1.2.4 Specific surface area	9
1.2.5 Hydraulic diameter	9
1.3 Outline	10
1.4 Closure	11
2 LITERATURE REVIEW	13
2.1 Pressure drop in open-cell foams	13
2.1.1 Critical review on selection of characteristic length	22
2.1.2 Critical review on pressure drop correlations	23
2.2 Dispersion in open-cell foams	24

2.3	Forced convective heat transfer in open-cell foams	26
2.3.1	Critical review on HTC correlations	33
2.4	Scope and objectives of present work	35
2.4.1	Objectives of the present work	36
2.5	Expected output and outcome of the present work	36
2.6	Closure	37
3	GEOMETRICAL MODELLING OF KELVIN STRUCTURE	39
3.1	Procedure to construct Kelvin structure	40
3.2	Closure	44
4	FLUID FLOW IN RETICULATED KELVIN STRUCTURE	45
4.1	Introduction	45
4.2	Problem statement	46
4.3	Numerical setup and post-processing	47
4.3.1	Governing equations and boundary conditions	47
4.3.2	Grid independence study	48
4.4	Results and discussion	50
4.4.1	Simulation results	50
4.4.2	Determination of permeability, drag coefficient and Ergun constants for ideal Kelvin structure.	55
4.4.3	Comparison of present simulation results with correlation provided in the present work.	59
4.4.4	Comparison of present correlation with DPLS results of real structures.	62
4.4.5	Comparison of present correlation with experimental results of real structures.	64
4.5	Conclusion	70
4.6	Closure	71
5	LONGITUDINAL DISPERSION IN RETICULATED KELVIN STRUC-	

TURE	73
5.1 Introduction	73
5.2 Dispersion in RPS	75
5.3 Problem statement	76
5.4 Numerical setup	76
5.4.1 Numerical procedure	77
5.5 Results and discussions	82
5.5.1 Simulation results	82
5.5.2 Determination of flow tortuosity	93
5.5.3 Comparison of Kelvin porous structures with real porous structures	95
5.6 Conclusion	97
5.7 Closure	98
6 CONVECTIVE HEAT TRANSFER COEFFICIENT IN RETICULATED KELVIN STRUCTURE	99
6.1 Introduction	99
6.2 Problem statement	101
6.3 Numerical setup and post-processing	101
6.3.1 Governing equations and boundary conditions	101
6.3.2 Numerical procedure	103
6.3.3 Grid generation	103
6.4 Results and discussions	105
6.4.1 Determination of heat transfer coefficient(HTC)	105
6.4.2 Heat transfer correlation based on Re	109
6.4.3 Comparison of the proposed correlation with DPLS results.	117
6.4.4 Comparison of the proposed correlation with available experiments in the literature.	121
6.4.5 Heat transfer correlation based on Hg	124
6.4.6 Comparison of Heat transfer correlations	125

6.5	Conclusion	130
6.6	Closure	131
7	CONCLUSION AND FUTURE SCOPE	133
7.1	Future Scope	135
7.2	Closure	136
	APPENDICES	136
I	Numerical results of pressure drop	137
II	Numerical results of dispersion coefficient	143
III	Numerical results of heat transfer coefficients	146
	REFERENCES	153
	LIST OF PUBLICATIONS	171

LIST OF TABLES

2.1	Pressure drop correlations proposed by different authors for open-cell foams.	20
2.2	Heat transfer correlations proposed by different authors for open-cell foams.	34
3.1	Structures that are considered for simulations	44
4.1	Pore densities, porosities, specific surface area, permeability and drag coefficient of ideal structures.	59
4.2	Comparison of RMSD values between the correlated Hagen number and experimental investigations (few of the authoress's specific surface area values collected from Dietrich 2012).	69
5.1	The simulated LDC results of various structures used in this study.	89
5.2	Tortuosity values of different foam structures determined using DPLS.	94
6.1	Comparison of Nusselt number RMSD values with numerical and experimental investigations in the literature	129
I.1	Pressure drop results of ideal structures.	137
I.2	Pressure drop and specific surface area results of Randomized structures (10 PPI 80% porosity).	138
I.3	Pressure drop and specific surface area results of Randomized structures (10 PPI 85% porosity).	139
I.4	Pressure drop and specific surface area results of Randomized structures (10 PPI 90% porosity).	141
II.1	Longitudinal dispersion coefficient values of ideal structures.	143
II.2	Longitudinal dispersion coefficient values of Randomized structure (10 PPI 80% porosity).	144

II.3	Longitudinal dispersion coefficient values of Randomized structure (10 PPI 85% porosity).	144
II.4	Longitudinal dispersion coefficient values of Randomized structure (10 PPI 90% porosity).	145
III.1	Heat transfer coefficient values of ideal structures (fluid of $Pr = 0.7$).	146
III.2	Heat transfer coefficient values of ideal structures (fluid of $Pr = 2$).	147
III.3	Heat transfer coefficient values of ideal structures (fluid of $Pr = 6$).	148
III.4	Heat transfer coefficient values of Randomized structure of 10 PPI 80% porosity (fluid of $Pr = 0.7$).	149
III.5	Heat transfer coefficient values of Randomized structure of 10 PPI 85% porosity (fluid of $Pr = 0.7$).	150
III.6	Heat transfer coefficient values of Randomized structure of 10 PPI 90% porosity (fluid of $Pr = 0.7$).	151

LIST OF FIGURES

1.1	(a) Open-cell foam (b) Closed cell foam (adopted from Sathurusinghe <i>et al.</i> 2012.	2
1.2	5 x 5 array of Kelvin structures: (a) ideal structure, (b) randomized structure (only scale factor) and (c) randomized structure (both scale and centroid factor).	3
1.3	Periodic open-cell foam models: (a) Lord Kelvin model, (b) Weaire-Phelan model, and (c) Voronoi model (adopted from Cunsolo <i>et al.</i> 2015; Das <i>et al.</i> 2018).	5
1.4	Reconstruction of reticulated porous structure through computer tomography (adopted from Ackermann <i>et al.</i> 2014).	6
1.5	Photo of real sponges: (a) 10 ppi, (b) 20 ppi, (c) 45 ppi and (d) 45 ppi of light microscopy picture (Dietrich <i>et al.</i> 2009).	8
3.1	Reticulated real and ideal open-cell foam samples	40
3.2	(a) Sample sphere constructed in VTK (b) Sample strut constructed in VTK.	42
3.3	Kelvin modelled porous structures : (a) Ideal Kelvin structure (b) Randomized Kelvin structure (both scale and centroid factor)	43
4.1	Ideal Kelvin structure's grid generated using ICEM CFD and imposed boundary conditions.	48
4.2	Grid independence study for 30 PPI 80% porosity ideal structure at Re=10	49
4.3	Grid independence study for 30 PPI 80% porosity ideal structure at Re=750	50
4.4	Nondimensionalized pressure profiles along the flow field in 30 PPI 85% porosity ideal structure for different Reynolds numbers.	51
4.5	Nondimensionalized pressure profiles for Re=750 for all randomized cases of 10 PPI 90% porosity (comparison between ideal and randomized structures).	51

4.6	Pressure drop versus velocity for ideal structures at 80% porosity with different PPI.	52
4.7	Pressure drop versus velocity for ideal structures at 30 PPI with different porosities.	53
4.8	Pressure drop versus velocity for randomized structures at 10 PPI with different porosities.	53
4.9	Comparison of pressure drop between ideal and randomized structures at 10 PPI 90% porosity.	54
4.10	a) Ideal Kelvin structure (b) Randomized Kelvin structure [70-65-40] velocity vector contour plots on a 2-D cut plane with same porosity 90%, pore density 10 PPI and $Re=750$	56
4.11	a) Ideal Kelvin structure (b) Randomized Kelvin structure [70-65-40] pressure contour plots on a 2-D cut plane with same porosity 90%, pore density 10 PPI and $Re=750$	57
4.12	Streamlines: (a) Ideal Kelvin structure (b) Randomized Kelvin structure [70-65-40] with same porosity 90%, pore density 10 PPI and $Re=750$	58
4.13	Hagen number versus Reynolds number of ideal Kelvin structures compared with present correlation (Eq. 4.10) at different porosities and pore densities.	60
4.14	Hagen number versus Reynolds number for randomized Kelvin structures compared with present correlation (Eq. 4.10) at different porosities and pore densities (scale factor:65%, centroid factor:40%).	61
4.15	Comparison of pressure drop results between DPLS and Eq. (4.10) at 80% porosity of different ideal Kelvin structures.	61
4.16	Comparison of pressure drop results between DPLS and Eq. (4.10) at 10 PPI 90% porosity of ideal & randomized structures.	62
4.17	Comparison of pressure drop values calculated using Eq. (4.10) with DPLS results of real structures (10, 20 & 30 PPI Al_2O_3 open-cell foams at 80% porosity).	63
4.18	Hagen number versus Reynolds number (DPLS results of real structure vs present correlation).	63
4.19	Comparison of pressure drop values calculated using Eq. (4.10) with experimental results of real structures (20, 30 & 45 PPI Alumina ceramic open-cell foams with total porosities 80.8, 80.6 and 80.8%, respectively).	65

4.20	Comparison of pressure drop values calculated using Eq. (4.10) with experimental results of real structures (10, 20 & 30 PPI SSiC ceramic open-cell foams with total porosities 87.8, 89.6 and 88.5%, respectively).	65
4.21	Comparison of pressure drop values calculated using Eq. (4.10) with experimental results of real pore structures (45, 60 & 100 PPI Ni metallic open-cell foams with total porosities 97.8, 97.5 and 97.3%, respectively).	66
4.22	Comparison of pressure drop values calculated using Eq. (4.10) with experimental results of real pore structures (45, 60 & 100 PPI Ni metallic open-cell foams with total porosities 97.8, 97.5 and 97.3%, respectively).	66
4.23	Comparison of experimental pressure drop results with calculated pressure drop using Eq. (4.10).	67
4.24	Hagen number versus Reynolds number between experimental results of real porous structures and present study correlation.	68
5.1	(a) Evolution of the transition zone with time (adopted from Fried 1975) (b) mixing and spreading of tracer concentration	74
5.2	Final grid sample of 30 PPI 80% porosity.	77
5.3	Constant tracer concentration at $Y = 0.5$ (light gray) pass on into a foam geometry (dark gray).	79
5.4	Instantaneous tracer concentration profiles at 5 time steps (a) Ideal structure of 30 PPI and 80% porosity (b) Randomized structure of 10 PPI and 80% porosity.	80
5.5	Instantaneous tracer concentration gradient profiles at 5 time steps (a) Ideal structure of 30 PPI and 80% porosity (b) Randomized structure of 10 PPI and 80% porosity.	81
5.6	Dispersion coefficients and the time evolution of the mass fraction gradients (a) Ideal structure of 30 PPI and 80% porosity (b) Randomized structure of 10 PPI and 80% porosity.	83
5.7	(a) & (b) Ideal & randomized structure of 10 PPI with different porosities (c) Comparison of longitudinal dispersion coefficient with porosity and molecular Peclet number.	87
5.8	Ideal Kelvin structures of 10, 20, 30 PPI with constant (90%) Porosity.	87
5.9	The LDC Comparison of ideal and randomized Kelvin structures at 10 PPI 80% porosity.	88

5.10	Longitudinal dispersion between Kelvin structures vs packed beds (gaseous flow data adopted from Delgado 2006).	88
5.11	The DPLS results of longitudinal dispersion of all foam structures used in this study.	90
5.12	Comparison of longitudinal Peclet number in ideal and randomized Kelvin structures versus correlation provided for packed beds, where Pe calculated based on strut diameter (data adopted from Delgado 2006).	92
5.13	Comparison of longitudinal Peclet number with pore and strut diameter.	92
5.14	Comparison of modified molecular Peclet number versus longitudinal dispersion of gaseous flow in ideal and randomized Kelvin structures.	94
5.15	Modified longitudinal Peclet number versus modified molecular Peclet number of ideal and randomized Kelvin structures (using correlated characteristic length given by Eq. 5.16).	95
5.16	Peclet number calculated with the modified characteristic length correlation (Eq. 5.16) using present study tortuosity values (refer Table 5.2) and Habisreuther <i>et al.</i> 2009 tortuosity value ($\tau = 1.08$).	96
6.1	The grid of an ideal Kelvin structure was created using ICEM CFD and boundary conditions applied.	102
6.2	Grid study of 30 PPI 80% (a) Re=100 (b) Re=750	104
6.3	Local Nusselt numbers and fluid bulk temperature distribution along the flow direction (a) Ideal Kelvin structure 30 PPI 90% porosity (b) Randomized Kelvin structure 10 PPI 90% porosity[50-75-40] at Re =500 and Pr =0.7	107
6.4	Effect of PPI (a) Pr=0.7, (b) Pr = 2 (c) Pr =6	109
6.5	Effect of porosity (a-d) Ideal Kelvin structure of different working fluids (Pr=0.7, Pr=2 and Pr =6) and (d) randomized Kelvin structure (Pr = 0.7)	111
6.6	The VHTC for the ideal and randomized structure's comparison at 10 PPI 90% porosity (Pr =0.7).	112
6.7	The comparison of all foams used in this study according to their DPLS results (Pr =0.7)	112
6.8	Temperature field contours (a) Ideal Pr =0.7 (b) Ideal Pr =6 and (c) Randomized Pr =0.7 of 10 PPI 90 % porosity at Re = 10	114

6.9	Temperature field contours (a) Ideal Pr =0.7 (b) Ideal Pr =6 and (c) Randomized Pr =0.7 of 10 PPI 90 % porosity at Re = 750	115
6.10	Comparing Nusselt number with Reynolds number for different porosities and PPI of ideal Kelvin structures (Pr = 0.7)	116
6.11	Comparison of Nusselt number DPLS data with current study correlation (Eq. 6.7) at various porosities and PPI. (a) Ideal structure (b) Randomized structure (Pr =0.7)	118
6.12	Nusselt number comparison with present work correlation at different working fluids (Pr =2, and 6) dashed lines indicates $\pm 15\%$ error band	119
6.13	Comparison of HTC results between DPLS and Eq. (6.7) for different working fluids (a) Air Pr = 0.7, (b) salt water Pr = 2 and (c) Water Pr = 6	120
6.14	Comparison of HTC values computed using Eq. (6.7) against experimental outcomes of real porous structures (10, 20, 30 and 40 PPI Al_2O_3 metal foams with total porosities 0.926, 0.93 and 0.926, respectively).	122
6.15	Comparison of HTC values computed using Eq. (6.7) against experimental outcomes of real porous structures (10, 20, 30 and 40 PPI Al_2O_3 metal & ceramic foams with different porosities , respectively). . .	122
6.16	Comparison of HTC values computed using Eq. (6.7) against experimental & numerical outcomes of real porous structures at 40 PPI & 94% porosity (Cu metal foams)	123
6.17	Comparison of experimental HTC results with calculated HTC using Eq. (6.7).	123
6.18	Validation of the present work correlation.	124
6.19	Comparison of Nusselt number DPLS data with current study correlation B (Eq. 6.10) at various porosities and PPI. (a) Ideal structure (b) Randomized structure (Pr =0.7)	126
6.20	Nusselt number comparison with present work correlation at different working fluids (Pr =2, and 6) dashed lines indicates $\pm 15\%$ error band	127
6.21	Validation of the present work correlation.	127

Nomenclature

Roman

A	[-] constant
a, b	[-] coefficients
A_o	[m ²] outer surface area
B	[-] constant
c_F	[-] drag coefficient
c_p	[JKg ⁻¹ K ⁻¹] specific heat capacity
D	[m] size of the square rod
d_{window}	[m] window diameter
d_C	[m] cell diameter
d_h	[m] hydraulic diameter
D_L	[m ² /s] longitudinal dispersion coefficient
D_m	[m ² /s] molecular diffusion coefficient
d_n	[m] nominal diameter
D_p	[m] particle or equivalent diameter of sphere
d_{pore}, d_p	[m] pore diameter
d_s	[m] strut diameter
\dot{D}	[m ² /s] dispersion tensor
\dot{q}	[Wm ⁻²] heat flux
dp	[Pa] pressure drop
dx	[m] length of the structure
f	[-] friction factor

f'	[-] friction coefficient
F_o	[-] Forchheimer number
h, h_{sf}	$[Wm^{-2}K^{-1}]$ heat transfer coefficient
h_v	$[Wm^{-3}K^{-1}]$ Volumetric heat transfer coefficient
h_l	$[Wm^{-2}K^{-1}]$ local heat transfer coefficient
Hg	[-] Hagen number
K	$[m^2]$ permeability
K_1	$[m^2]$ permeability coefficient of the viscous term
K_2	$[m]$ permeability coefficient of the inertial term
k_f	$[Wm^{-1}K^{-1}]$ thermal conductivity of a fluid
L	$[m]$ total length of domain
L^+	[-] normalized length
m, c	[-] constants
Nu	[-] Avg. Nusselt number
Nu_l	[-] local Nusselt number
Pe_L	[-] Peclet number $(\frac{ud}{D_L})$
Pe_m	[-] Peclet number $(\frac{ud}{D_m})$
Pr	[-] Prandtl number $(\frac{\mu c_p}{k_f})$
Re	[-] Reynolds number
S_v, a_c	$[m^{-1}]$ specific surface area
T	$[K]$ temperature
t	$[sec]$ time
T_i	$[K]$ inlet temperature of fluid
T_o	$[K]$ outlet temperature of fluid
T_w	$[K]$ temperature of solid
u	$[m/s]$ internal bulk velocity

u_s	[m/s] superficial velocity
$\overline{x_{sim}(t)}$	[m] mean distance
Y	[kg/kg] tracer mass fraction

Greek

σ^2	[-]variance
μ	[Ns/m ²] fluid dynamic viscosity
ν	[m ² /s] fluid kinematic viscosity
ρ	[kg/m ³] fluid density
τ	[-] tortuosity
ε_o	open porosity
ζ, η	coefficients

Abbreviations

CAD	computer adided design
Calc	calculated
CFD	computational fluid dynamics
CT	computer tomography
DPLS	direct pore level simulation
CDS	central difference scheme
Exp	experimental
GLE	Generalized L�ev�eque Equation
HTC	heat transfer coefficient
LMTD	log mean temperature difference
LTE	local thermal equilibrium

LTNE	local thermal non equilibrium
MRI	magnetic resonance imaging
PPI	pores per inch
RMSD	root mean square deviation
RPS	reticulated porous structure
Sim	simulation
VHTC	volumetric heat transfer coefficient
VTK	visualization tool kit
WHTC	wall heat transfer coefficient
DNS	direct numerical simulation
LBM	lattice boltzmann method
LDC	longitudinal dispersion coefficient
OpenFoam	open-source field operation and manipulation
SEBM	selective electron beam melting

CHAPTER 1

INTRODUCTION

The transport of heat and mass in porous media have a significant influence on a wide range of engineering applications such as solar reactors, building thermal insulation, packed cryogenic microsphere insulation, combustors, chemical and biological reactors, etc. The porous media are heterogeneous systems consisting of several interconnected solid phases with continuous void/fluid space. Within the fluid region, the conservation equations can be used to describe the transport phenomena within the pores.

Recently, there has been a greater emphasis on using advanced materials to enhance effectiveness of energy transfer and reduce the weight cum volume required in energy transfer systems. Reticulated porous structures (RPS) are one type that will come under this novel category of geometries & materials, because of their prominent features such as high specific surface area, good permeability, higher porosity, as well as good mixing and low-pressure drop compared to the packed beds. Furthermore, due to the continuous solid phase, which offers a good capacity for heat transfer augmentation. In general, these structures are named as foams, and it can be differentiate in two ways: if the voids are interconnected with each other, it can be named as “open-cell foam “ (refer Figure 1.1a). If voids are isolated from one another, it is often called as “closed-cell foam” (refer Figure 1.1b). Most of the earlier studies done to understand the pressure drop in porous media were performed taking packed bed type of porous media. The emergence of RPS as an alternative to the packed beds in various industrial applications such as catalytic converters, groundwater treatment, geothermal energy harvesting, porous pre-heaters & flame stabilizers, radiant porous burners, natural gas production (Kaviany 1995), in the biomedical field, jet engine application and solar applications (Ortega 2013; Azzi *et al.* 2007; Rashidi *et al.* 2017), it becomes necessary to study the fluid flow and heat transfer accurately in RPS to improve the efficiency and design of the

above mentioned engineering systems and applications.

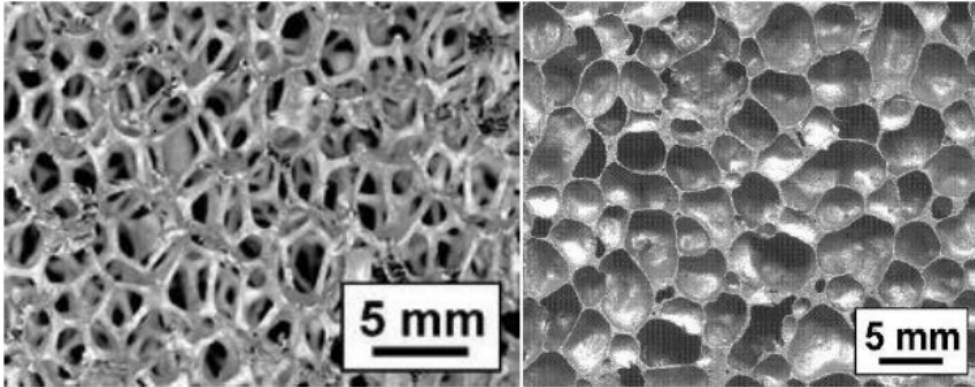


Figure 1.1: (a) Open-cell foam (b) Closed cell foam (adopted from Sathurusinghe *et al.* 2012).

Generally, the porous domain in engineering applications is much bigger than the pore size, and continuum models are used to solve the conservation equations (Kaviany 1995; Bear 1988). According to continuum models, the effect of the porous material and the structural parameters on the transport phenomena are described through the effective transport properties (Kaviany 1995; Bear 1988). For example, in high-temperature applications like radiant porous burners or porous combustors, the precise estimation of heat and species transport inside the porous domain plays an essential role in designing and optimizing such engineering applications. In general, the effective transport properties are calculated using either an approximate analytical method or by experimental method. Due to the intricate shape of foam geometries, the analytical method is quite inaccurate, while experimental measurements are time-consuming and subject to measurement uncertainties and inaccuracies. To overcome those uncertainties and accurately capture the specific geometrical characteristics, alternatively, many studies proposed numerical simulations at the pore level (Das *et al.* 2018). Economically, this method is cheaper than the experimental. Moreover, numerical simulations can precisely control the flow conditions and arbitrary material properties. Typically, the fluid flow and heat transfer in porous media are calculated with the help of numerical simulations by two approaches: (1) a macroscopic approach i.e. volume-averaged

method and (2) a microscopic approach i.e. Direct Pore Level Simulations (DPLS). In the first approach, small-scale details are omitted, and the knowledge that is thus lost is represented in the governing equations by an engineering model. In the second approach, the exact morphology of the porous structure is taken into account to simulate the small-scale flow characteristics. In this work, DPLS approach is used to analyze the fluid flow and heat transfer in reticulated open-cell foam. The reticulated porous structures are modelled based on the theoretical Kelvin model, representing the real porous structures that are shown in Figure 1.2. The geometry of these structures are generated with the help of in-house code and visualisation tool kit (VTK) libraries (detailed procedure explained in chapter 3). The ideal and randomized Kelvin structures are generated for different PPI (pores per inch) & porosities. By varying the geometrical parameters, the influence of geometries on heat transfer between the flowing fluid and solid phase of open-cell foams are investigated. Based on the simulation outcomes, new correlations are proposed to calculate the pressure drop, dispersion, and heat transfer coefficients in the reticulated porous structures.

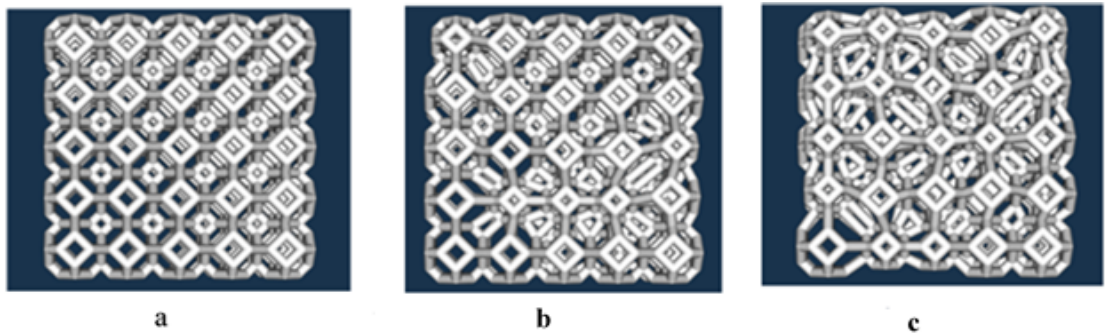


Figure 1.2: 5 x 5 array of Kelvin structures: (a) ideal structure, (b) randomized structure (only scale factor) and (c) randomized structure (both scale and centroid factor).

1.1 Background about idealized periodic open-cell foam structures

The quantitative description of transport phenomena in reticulated porous structures are thus far restricted to semi-empirical correlations. Moreover, these correlations were usually derived for different structure types and are therefore applicable only with reduced accuracy on the investigated porous structures. In the attempted analytical modelings, simplified reticulated structures such as unit cell structures are studied (Nieh *et al.* 2000; Plessis and Masliyah 1988). Such simplified cell structures include, for example, an octahedron model, a stretched cubic cell shape or square channels which are each perpendicular to each other. One has more in reality the reticulated porous structures resemble a Kelvin structure (William 1887) (as a basic monomeric unit cells Ref. Figure 1.3a). This has long been regarded as the best description for real open cell reticulated structures. It is described in detail in the literature and has been applied to the analysis of porous structures (Kusner *et al.* 1996, Roberts and Garboczi 2001). A newer, more complex model is based on the Weaire-Phelan (Ref. Figure 1.3b)(Weaire and Phelan 1996) structure as a monomer unit. This unit consists of eight cells with two basic types: an irregular pentagonal dodecahedron and a tetrakaidehedra with twelve pentagonal and two hexagonal faces. Models of this kind help to clarify the key structural features and their influence and physical and chemical phenomena, but the regular monomeric units in reality are not capable of describing the physical significance of more statistically irregular, complex porous microstructure of reticulated porous structures and have only limited relevance. This unit cell models are not in a position to account for the typical, natural variations in the microstructure of monolithic reticulated porous structures (Zhu *et al.* 2000). To incorporate this structural disorder, many authors use models that work on the basis of Voronoi mosaics (Ref. Figure 1.3c) and a random distribution of seed points in space. A cell is defined by the space that is closer to a specific start point as on all others. The amount of disorder of such a structure will depend on the spatial distribution of the starting points (Roberts and Garboczi 2002, 2001; Grenestedt

and Tanaka 1999; Zhu *et al.* 2000; Huang and Gibson 2003). Another model, which works on the basis of a Gaussian random field was applied in (Roberts and Garboczi 2002) for determining the elastic properties of three-dimensional porous monoliths. A serious drawback of these structures is however, in the topology of the Voronoi cells that are created, in comparison with real structures per node, Voronoi cells too often have high a number of connecting bridges. For obvious reasons, this does affect both the mechanical stability of the structure as well as their thermal transport properties.

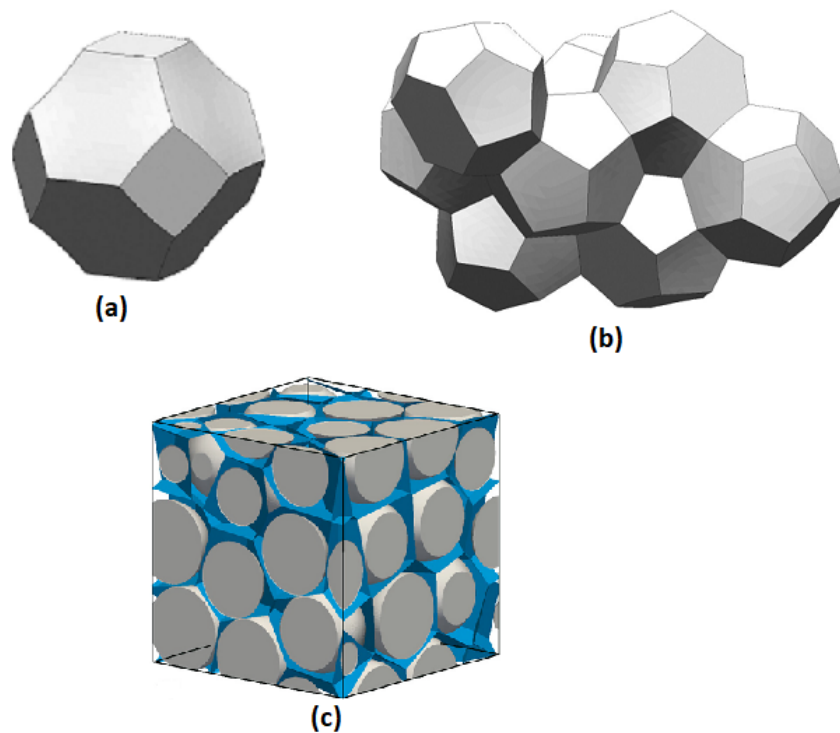


Figure 1.3: Periodic open-cell foam models: (a) Lord Kelvin model, (b) Weaire-Phelan model, and (c) Voronoi model (adopted from Cunsolo *et al.* 2015; Das *et al.* 2018).

For the numerical simulation of fluid transport processes in the micro-structure of various materials cells, particular principal methods of calculation are available. One way of calculation is the complicated Lattice-Boltzmann Method (LBM)(Chen and Doole 1998), in which the molecular-kinetic is simulated directly by statistical methods (applied to porous media such as in Coles *et al.* 1998; Bernsdorf *et al.* 2000; Humby *et al.* 2002). General description of the flow processes could also be solved by the numerical methods such as finite element modeling (FEM) and the finite volume model (FVM) in

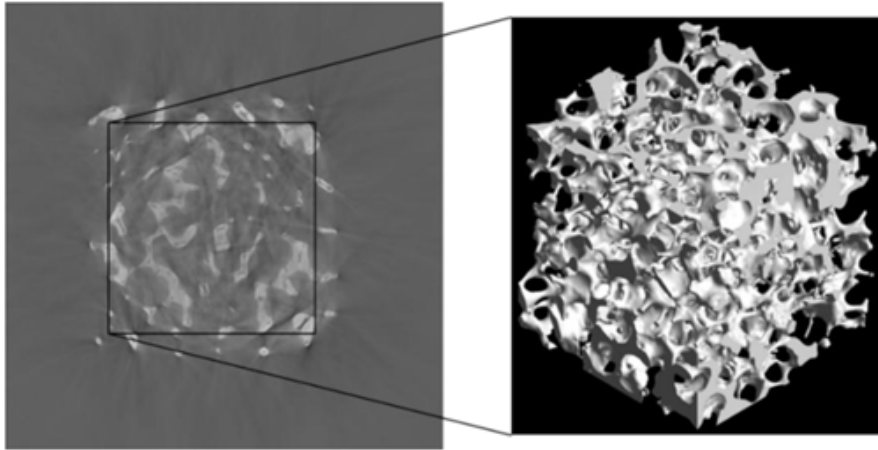


Figure 1.4: Reconstruction of reticulated porous structure through computer tomography (adopted from Ackermann *et al.* 2014).

which case both are available in commercial CFD (computational fluid dynamics) and open source programs. Regardless of which method of numerical simulation is chosen, it is necessary to discretize the porous microstructure, and thus bringing the geometrical structure of the simulation as input available. A more realistic possibility for the detailed mapping of the microstructure of a porous media is the application of digital, imaging procedures given such as computer tomography or X-ray scanning (Ref. Figure 1.4). Through the reconstruction of these highly randomized porous structures using computer tomographic scans (e.g., Humby *et al.* 2002; Petrasch *et al.* 2007; Diani *et al.* 2015; Parthasarathy 2016); Nie *et al.* 2017), one could be able to define the effective properties of the investigated porous structures accurately. But it is well known that these correlations are usually valid only for the investigated geometry and are therefore applicable only with reduced accuracy on other porous structures. In order to develop precise generalised semi-empirical correlations for the effective transport properties, It is necessary to thoroughly investigate the effects of each and every geometrical parameter on the transport properties. Well-defined structures (e.g. Kelvin structures and randomized Kelvin structures) could be used to perform direct pore level simulations. This will help in studying the influence of the geometrical properties of the structures on the heat and mass transfer properties in great detail.

1.2 Reticulated porous media characterization

In order to develop accurate generalized semi-empirical correlations for the effective transport properties, the evaluation of each and every geometrical property is needs to be studied in detail. The crucial geometrical parameter includes porosity, pore diameter, pore density (PPI), specific surface area, tortuosity, and hydraulic diameter.

1.2.1 Porosity

Porosity(ε) is the one of main geometrical property of porous media and it is define as, the ratio of pore volume V_P (void space) occupied in the material to the total volume V_T . Where the total volume includes both pore volume and solid volume V_S . Porosity measures the percentage of empty void space in a porous media. If an object is of high porosity, it has a great ability to hold fluid within itself. For example, sponges, wood, rubber, and some rocks are consider under natural porous materials. Ceramics, composite materials, and high-porous metallic foams are examples of man-made porous media. Generally, two types of porosities are defined for the open-cell fomas i.e., total porosity and open porosity. Total porosity counts all kinds of the pore space, like macroscopic pores and also microscopic pores that are present in the struct. But the open porosity counts only the macroscopic pore space. Most of the cases the total and open porosities are nearly same due to additive manufacturing capabilities that are available in present days. In this study, only open porosities are considered because these are more relevant in the study of fluid flow and heat transfer. Initially the open porosity is given as input for the generation of geometry, later the open porosity values are checked by using the volume of the elements in the computaional grids. i.e., to calculate open porosity, the total pore volume is calculated by adding all the tetrahedral volumes of void spaces that are obtained from computational grids. Therefore, the open porosity is obtained by dividing the total pore volume with the total volume of the porous media.

1.2.2 Pore density

The number of pores in a given length/volume is called pore density (PPI). In this study, it is defined as number of pores in one linear inch and the unit Kelvin structures are scaled based on pore densities like 10, 20, 30 PPI.

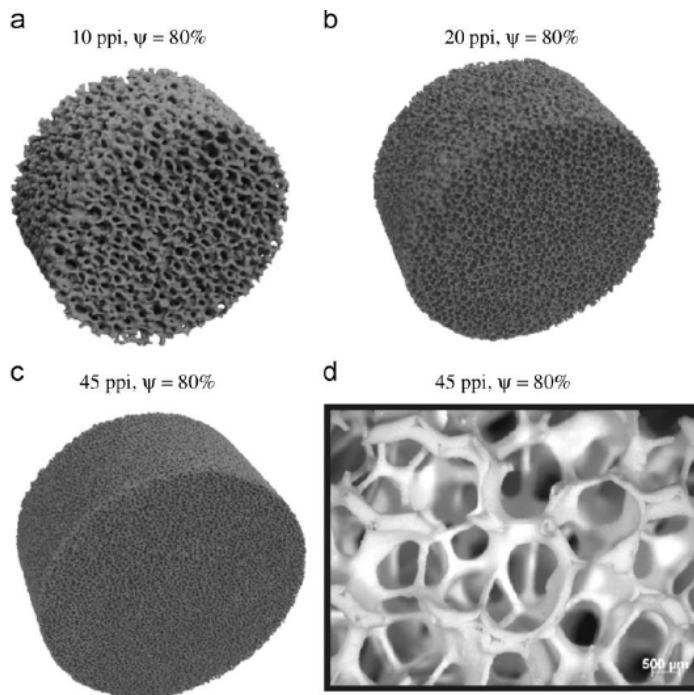


Figure 1.5: Photo of real sponges: (a) 10 ppi, (b) 20 ppi, (c) 45 ppi and (d) 45 ppi of light microscopy picture (Dietrich *et al.* 2009).

1.2.3 Pore diameter

The pore diameter (d_{pore}) is calculated from the pore densities using the relation $d_{pore} = 0.0254/PPI$ (Hackert *et al.* 1996). A high PPI number is equivalent to a small pore size. The PPI number of the real pore sponges shown in Figure 1.5 ranges from 10 to 45 PPI (Dietrich *et al.* 2009).

1.2.4 Specific surface area

While dealing problems with fluid and heat transport through foams, specific surface area (S_V) is one of the important geometrical parameter, it can be used to differentiate and compare with other porous structures as honeycombs and packed beds. In general, it is define as the ratio of external struct surface area to the entire volume of the sponge. Moreira *et al.* (2004a) measured the specific surface area by image analysis. In recent publications, Grosse *et al.* (2009) and Incera Garrido *et al.* (2008) used MRI and CT to measure the specific surface area of ceramic foams. Dietrich (2012) proposed a correlation for the specific surface area from the experimental results as follows,

$$S_v = 2.87 \cdot \frac{1}{d_{struct} + d_{window}} \cdot (1 - \varepsilon)^{0.25} \quad (1.1)$$

In this study, the total surface area of the solid region is found by adding all surfaces of the triangular surface elements, and total volume of the reticulated porous media is calculated by adding all their volume elements. The specific surface area is obtained by dividing the total surface area by the total volume of the reticulated porous media. The porosity and specific surface area values of each sponge used in this work is reported in Table 4.1.

1.2.5 Hydraulic diameter

In order to define the friction in the porous media, the concept of hydraulic diameter (d_h) is used as a characteristic length and it define as

$$d_h = 4 \cdot \frac{\text{cross section area avialble for fluid flow}}{\text{wetted perimeter}} = 4 \cdot \frac{A_F}{P} \cdot \frac{L}{L} = 4 \cdot \frac{V_F}{A_S} \cdot \frac{V_T}{V_T} = \frac{4\varepsilon}{S_v} \quad (1.2)$$

Where, ε represents the open porosity. The hydraulic diameter of different structures used in this study are calculated and tabulated in Table 4.1.

Along with these structural properties, the hydraulic and thermal transport properties such as; permeability, drag coefficient, pressure drop, dispersion and convective heat transfer coefficients are studied and explained in the next chapters.

1.3 Outline

The structure of this thesis is organised based on the topics in seven chapters and an appendix.

In chapter 1, the introduction about reticulated porous media and methods used to determine morphological parameters are discussed. A brief introduction to predict the performance of porous media using the volume averaging method and pore level simulation is addressed.

In chapter 2, a comprehensive review of the literature on earlier works based on various topics are presented. The scope, motivation and objectives of the present study are addressed.

In chapter 3, the construction of 3D geometry of the ideal and randomised Kelvin structure using a program algorithm is thoroughly described.

Chapter 4 deals with the methodology used to determine the pressure drop in reticulated porous media. The grid independence study, boundary conditions and governing equations related to flow calculations are provided. The method used to determine new values of viscous and inertial coefficients is documented. And also, a relation between the Hagen number and the Reynolds number is presented.

Chapter 5 provides the study of the longitudinal dispersion in reticulated porous media. Discussion on a parametric study to understand the influence of geometrical parameters on dispersion is provided. The methodology used to determine flow tortuosity is discussed. And also presented is a new characteristic length correlation to determining the longitudinal Peclet number.

In Chapter 6, the methodology used to predict the forced convective heat transfer coefficient for various working fluids is documented. The influence of pore size and porosity

on the volumetric heat transfer coefficient is described thoroughly. And also provided is an empirical correlation to calculate the Nusselt number with the use of Hagen number.

Finally, a conclusion and the future scope of the present study is discussed in Chapter 7. In the appendix (I, II and III) all the simulation results obtained in this study are tabulated.

1.4 Closure

A brief introduction to reticulated porous media and its morphological parameters was addressed in this chapter. A detailed description of idealized periodic open-cell foams was also reported. The literature review conducted for the present work is presented in the next chapter.

CHAPTER 2

LITERATURE REVIEW

A comprehensive review of experimental and numerical analysis of fluid flow and heat transfer in reticulated porous structures is given below.

2.1 Pressure drop in open-cell foams

The fluid flow in porous media is analogous to that of pipe flow. The flow behaviour is described in terms of the Reynolds number and various flow regimes have been recognised and are connected with changes in the friction coefficient and pressure drop. However, because of the vast surface area, complicated interior structures, and inherent variance in the media, there is a significant amount of experimental scatter, and there are variations in the definition of the characteristic length. As a result, comparing the flow characteristics of various porous media is challenging. Here, several studies of pressure drop results in open-cell foams using experimental and numerical methods are reviewed precisely.

Moreira and Coury (2004*b*) conducted experiments to study the effect of structural parameters in the measurement of permeability using SiC and Al_2O_3 ceramic foams. The ceramic foams with various pore sizes (PPI) were employed. Water was used as the flowing fluid in the measurement of permeability. The authors reported that the estimated permeability scatters significantly with the investigated parameters. Further, the experimental data were fitted with an Ergun type correlation, the correlation is able to capture the permeability of the media in all foams under the investigated experimental conditions.

Liu *et al.* (2006) conducted experiments to determine the pressure drop of seven kinds of aluminum foams and ceramic foams with different porosities (80.2%-95.8%)

and pore densities (5 PPI-65 PPI). Based on experimental outcomes, the authors executed a regression evaluation to correlate the empirical equation in terms of friction factor. These correlations have been used to calculate flow friction characteristics in metal foams especially in regimes with greater Reynolds numbers. To extend the applicability of developed correlation, the authors combined the data provided by Richardson *et al.* (2000) and again performed regression analysis and compared towards experimental data. It is reported that the developed empirical equation is appreciably good with the experimental results. Further comparison was made with the experimental records of Du Plessis *et al.* (1994). From the comparison, the authors reported that the experimental values of Du Plessis *et al.* (1994) were smaller than the correlated values because of discrepancies between measured spherical diameter versus calculated spherical diameter.

Dukhan (2006) measured pressure drop in nine samples of aluminium open-cell foams having different porosities (67.9% to 92.3%) and pore densities (10, 20 and 40PPI). The authors conducted experiments through a steady-state approach, where the air was used as a working fluid. The authors compared nine samples of pressure drop results with each other and noticed a high-pressure drop in the low-porosity foams. The investigation mainly focused on developing correlations for permeability and drag coefficient with porosity. The author concluded that the permeability correlation was better able to predict some of the previous results of Hwang *et al.* (2002) and Antohe *et al.* (1997).

A variety of correlations found in the literature were listed by Edouard *et al.* (2008) and compared to their experimental results. The authors noticed that the standard deviation between the experimental and analytical pressure drops reached 100%, proving that no model can accurately estimate the pressure drop. Additionally, the authors also reported that the method developed by Du Plessis (1994) and Lacroix *et al.* (2007) provided a reliable estimate of pressure drop, with the majority of experimental results in published studies falling within a $\pm 30\%$ error range.

Dietrich *et al.* (2009) proposed an Ergun kind of pressure drop equation (one used in this study, Eq. 4.5) with the help of experiments on real porous ceramic sponges of 10, 20, 30 and 40 PPI with nominal porosity 75% to 85%. By modeling the experimental data, the two constants of the Ergun equation were determined. The authors reported that those constants are unbiased of the material, porosity and pore density (PPI). The developed correlation also enables the calculation of a hydraulic diameter of sponges based on pressure drop measurements. To study the applicability of this correlation, Dietrich (2012) made an in-depth assessment of various sets of experimental records (almost 25 authors) of various varieties of sponge materials, fluids and Reynolds numbers $10^{-1} < Re < 10^5$. The author concluded that the developed correlation is applicable for predicting the non-dimensional pressure drop (Hagen number) in a single-phase flow within a RMSD of $\pm 40\%$.

Mancin *et al.* (2010) conducted experiments on six distinctive aluminum open-cellular foams with specific pore sizes 5, 10, 20 and 40 PPI, specific porosities between 0.903 to 0.956 and relative densities between 9.7% to 4.4%, under a broad range of air flow rate. The collected data from experiments were analyzed and compared with reference models available in the literature. The authors reported that the models proposed by Bhattacharya *et al.* (2002) and Du Plessis *et al.* (1994) provide a good match for their experimental data. Based on experimental outcomes, the authors proposed a new simple pressure drop model and it was compared with their own experimental data and reported that a relative deviation of 0.99%, a mean absolute deviation of 3.1% and a standard deviation of 3.5%.

Tetrakaidecahedrons are an ideal structure, and Inayat *et al.* (2011b) investigated the pressure drop in this configuration. The ideal structure was manufactured using selective electron beam melting (SEBM) method for which geometry was designed using Computer Aided Design (CAD) software, and pressure drop was then experimentally determined. For the viscous and inertial coefficients of the Ergun equation, non-empirical relations are given. According to the authors, the proposed coefficients

are able to predict the pressure drop in both idealised structures and densely packed beds. In the next investigation, Inayat *et al.* (2011a) used previously proposed coefficients to determine the pressure drop in ceramic sponges. The authors noticed that those correlations overestimated the pressure drop inside the ceramic sponges. Then the authors modified the previous coefficients with empirical exponent values; it is now possible to determine the pressure drop inside sintered SiC sponges with a deviation of less than 5%.

The effects of pressure drops in open-cell foams have also been analyzed using numerical simulations based on Computational Fluid Dynamics (CFD), which has been shown to be an excellent tool for estimating pressure drops in porous media. To perform such numerical simulations, many authors modelled the foam 3d geometry using idealised unit cells, tomographic reconstruction foam models, and artificially created foam models. Those kinds of studies are briefly reviewed below.

Diani *et al.* (2014) performed a sensitivity evaluation to maintain the no. of pores required for accomplishing fully developed flow in open-cell foams. Initially, the simulations were performed on the 40 PPI sample by placing different pores (5, 10 and 20 pores) in the flow field. From the results of a simulation, the pressure drop was calculated in each case, and it was compared and reported that the pressure drop of 5 pores sized sample has a large difference (-15.7%) with 10 pores sized sample. Similarly, the pressure drop difference in 20 pores and 10 pores sized samples is only -3.2%. Therefore, the authors stated that to achieve a fully developed flow in open-cell foams, the domain size has to be maintained around 10 pores in the direction of flow. Further, the pressure drop results of 5, 10, 20, and 40 PPI samples were analyzed and compared against experimental data of Mancin *et al.* (2013), and it was reported good compatibility with a mean relative deviation of -3.8% and absolute deviation of 5.4%, respectively.

Regulski *et al.* (2015) investigated the pressure drop in open-cell foam of samples 10, 20 and 30PPI with different porosities (75% to 79%). The study includes experimental and numerical simulations using the Lattice Boltzmann Method (LBM) method,

where sponge geometries are constructed through image analysis. The authors mainly focused on establishing the pressure drop correlations that will be exclusively based on the geometrical properties of those kinds of foams, and image analysis plays a crucial role in this case. The acquired results were further compared with data of other researchers and with few pressure drop correlations.

Ambrosio *et al.* (2016) studied the impact of strut shape on the pressure drop in open-cell foams analytically by adding a parameter that describes the strut's shape. Initially, the authors measured the geometrical parameters by reconstructing the real porous foams by CT scans. Later, the ideal Kelvin model foams were created with the same geometry parameters of real foam using the surface evolver software. The authors performed simulations on both ideal and real porous foams. Then the authors compared both simulation results and reported that except for the entrance, pressure drop in the ideal foam shows good agreement with real foam. It is also noted that the convex shape of the strut reduces pressure drop for any porosity and flow rate.

Parthasarathy *et al.* (2016) performed direct pore level simulations on reconstructed reticulated porous structures made of two different materials (Al_2O_3 & SiSiC) and porosities of 75%, 80% & 85% with pore densities of 10, 20, 30, and 45 PPI. The authors proposed new values for viscous and inertial coefficients for the Ergun equation to obtain the pressure drop in the open-cell sponge and compared the simulation results against experimental results provided by Dietrich *et al.* (2009). It is reported that there is a good agreement between the correlated pressure drop results and the experimental results, but in the case of Al_2O_3 45 PPI 80% porosity sponges, there was a considerable deviation in results because of larger specific surface area and closed pores. The authors also proposed a new pressure drop correlation while considering the effect of tortuosity in the flow direction.

Nie *et al.* (2017) reviewed the theoretical background of the pressure drop for open-cell foams and reported the different types of empirical correlations which is obtained from literature. Most of these correlations have a lack of general applicability due to

involvement of sponge specific empirical coefficients and another reason is presumably that inconsistency in the geometrical parameters used. However, only a limited set of correlations fit the experimental data. The authors investigated the foam porosities from 70% to 95% with a pore density of 10, 20, 30, 40 and 50 PPI. The 3D foam geometrical model was generated by using the Laguerre-Voronoi tessellation (LVT) model and numerical simulations were performed using ANSYS fluent for flow velocities between 0.5 m/s to 20 m/s. The simulated pressure drop results were compared and reported that there is good consistency with theoretical predictions developed by Inayat *et al.* (2016), experimental results by Dietrich *et al.* (2009) & Mancin *et al.* (2012).

de Carvalho *et al.* (2017) carried out a numerical investigation of pressure drop by making use of the pore-scale methodology on five specific open-cell metallic foams. The authors investigated the flow in the turbulent regime i.e., every flow through porous media is not a laminar, high-speed flows will occur and cause to the onset of turbulence within the pore space. RANS models are used to evaluate the turbulence within the pore space. The authors also conducted experiments on the samples to calculate the transport properties, with the same input data as that of simulations. From the results of numerical and experimental studies, the authors noticed that a smaller sample thickness would lead to a higher pressure drop in the flow directions. Similar results were found by Baril *et al.* (2008) and Dukhan and Patel (2010). Based on their experiments, de Carvalho *et al.* (2017) proposed the critical thickness of the sample should lie between 25 and 50 times d_{pore} for which pressure drop results converge asymptotically towards a constant value.

Kumar and Topin (2017) reported various relations available in the literature and indicated that the expressions of friction factor and Reynolds number vary from author to author because of different characteristic lengths which depend on foam morphology. To avoid these morphological ambiguities & discrepancies in the characteristic length, the authors proposed a new Forchheimer number (F_o) correlation in the form of equivalent Reynolds number where intrinsic characteristic length as a Darcian permeability and Forchheimer inertia coefficient. From the correlation, the authors distinguish the

flow regimes in open-cell foam as follows, if (F_o) less than 0.1 the flow remains within the Darcy regime, similarly the weak inertia regime occurs when (F_o) is greater than 1 and transition regime takes place in between 0.1 and 1. The authors compared and concluded that there was an excellent agreement between the derived empirical correlations of hydraulic properties and friction factor data against numerical/experimental flow data of Kumar and Topin (2014*b*) & Kumar and Topin (2014*c*).

Bracconi *et al.* (2019) performed a systematic investigation to estimate pressure drop in open-cell foams through numerical and experimental approaches. The foam geometries are constructed virtually and printed using additive manufacturing techniques. The authors performed a comprehensive analysis leading to a better understanding of how the interaction between the fluid flow and the structure is affected by geometrical characteristics such as cell size, porosity, and strut shape. Based on simulation outcomes, the authors reported that the pressure drop across the structures are decreased by increasing the cell diameter or void fraction. The authors noted that the average strut size is the major parameter impacting the pressure drop of gas flow within the open-cell foams. Further, the authors proposed an Ergun kind of pressure drop correlation by considering the cross-section of the struct shape like cylindrical and triangular and validated with their experimental results.

In recent publications, Yang *et al.* (2021) summarized the theoretical models of pressure drop in open-cell foams. The authors reviewed various models of foam geometries and provided improvements for a few models to achieve accurate prediction of pressure drop compared to experimental observations. Further, by adopting the Calmidi (1998)'s permeability model, the authors established two empirical correlations of permeability and suggested it for open-cell metal foams. Then the proposed correlations are compared with the experimental results of other authors and found relatively consistent within the 100% relative error.

Table 2.1: Pressure drop correlations proposed by different authors for open-cell foams.

Authors	Characteristic length(C_L)	Correlation for predicting the pressure drop
Lu <i>et al.</i> (1998)	$d_s = d_p \left(\frac{2}{\sqrt{3\pi}} \right) [1 - 6]^{1/2}$	$f = \left[0.044 + \frac{0.008(d_p/d_s)}{(d_p/d_s - 1)^{0.43 + 1.13(d_s/d_p)}} \right] Re^{-0.15}$
Giani <i>et al.</i> (2005)	$d_s = d_p \left[\frac{4}{3-t} (1 - \varepsilon) \right]^{1/2}$	$\frac{\Delta P}{L} = 13.56 \frac{d_p^3}{2(d_p - d_s)^4 d_s} \mu u + 0.87 \frac{d_p^3}{2(d_p - d_s)^4} \rho u^2$
Liu <i>et al.</i> (2006)	$D_p = \frac{6(1 - \varepsilon_o)}{s_v}$	$\frac{\Delta P}{L} = 22 \frac{(1 - \varepsilon)^2}{\varepsilon^3 d_p^2} \mu u + 0.22 \frac{(1 - \varepsilon)}{\varepsilon^3 d_p} \rho u^2$
Innocentini <i>et al.</i> (1999)	$D_p = \frac{6(1 - \varepsilon_o)}{s_v}$	$\frac{\Delta P}{\Delta x} = 150 \frac{(1 - \varepsilon_o)^2}{\varepsilon_o^3} \frac{\mu V}{D_p^2} + 1.75 \frac{(1 - \varepsilon_o)}{\varepsilon_o^3} \frac{\rho V^2}{D_p}$
Richardson <i>et al.</i> (2000)	d_p	$\frac{\Delta P}{\Delta x} = \frac{E_1}{36} \frac{1}{\varepsilon_o^3} a_c^2 \mu V + \frac{E_2}{6} \frac{1}{\varepsilon_o^3} a_c \rho V^2$ $E_1 = 973 d_p^{0.743} (1 - \varepsilon_o)^{-0.0982}$ $E_2 = 368 d_p^{-0.7523} (1 - \varepsilon_o)^{0.07158}$
Du Plessis (1994) & Fourie and Du Plessis (2002)	$d_s = d_p \left(\frac{2}{3 - \tau} - 1 \right)$	$\frac{\Delta P}{\Delta x} = \frac{36\tau(\tau - 1)(3 - \tau)^2}{4\varepsilon_o^2 d_p^2} \mu V + \frac{2.05\tau(\tau - 1)}{2\varepsilon_o^2 d_p} \rho V^2$

Tadrist <i>et al.</i> (2004)	d_s	$\frac{\Delta P}{\Delta x} = c_1 \frac{(1-\varepsilon_o)^2}{\varepsilon_o^3} \frac{\mu V}{d_s^2} + c_2 \frac{(1-\varepsilon_o)}{\varepsilon_o^3} \frac{\rho V^2}{d_s}$
		$100 \leq c_1 \leq 865 \text{ and } 0.65 \leq c_2 \leq 2.6$
Moreira <i>et al.</i> (2004b)	d_p	$\frac{\Delta P}{\Delta x} = 1.275 \times 10^9 \frac{(1-\varepsilon_o)^2}{\varepsilon_o^3 d_p^{-0.05}} \mu V + 1.89 \times 10^4 \frac{(1-\varepsilon_o)}{\varepsilon_o^3 d_p^{-0.25}} \rho V^2$
Topin <i>et al.</i> (2006)	d_s	$\frac{\Delta P}{\Delta x} = \frac{1}{1.391 \times 10^{-4}} \frac{(1-\varepsilon_o)^2}{\varepsilon_o^3} \frac{\mu V}{d_s^2} + 1.32 a_c \rho V^2$
Inayat <i>et al.</i> (2011b)	$D_p = \frac{6(1-\varepsilon_o)}{a_c}$	$\frac{\Delta P}{\Delta x} = \frac{E_1}{36} \frac{1}{\varepsilon_o^3} a_c^2 \mu V + \frac{E_2}{6} \frac{1}{\varepsilon_o^3} a_c \rho V^2$ $E_1 = \left[\left(\frac{1-0.971(1-\varepsilon_o)^{0.5}}{0.6164(1-\varepsilon_o)^{0.5}} \right) \varepsilon_o \right]^{-1}$ $E_2 = \left[\left(\frac{1-0.971(1-\varepsilon_o)^{0.5}}{0.6164(1-\varepsilon_o)^{0.5}} \right) (1 - \varepsilon_o) \right]$
Dietrich <i>et al.</i> (2009)	$d_h = \frac{4\varepsilon}{S_v}$	$\frac{\Delta P}{\Delta x} = 110 \frac{1}{\varepsilon_t} \frac{\mu V}{d_h^2} + 1.45 \frac{1}{\varepsilon_t^2} \frac{\rho V^2}{d_h}; Hg = \frac{\Delta P}{\Delta x} \frac{d_h^3}{\rho V^2}$ $Hg = 110 Re + 1.45 Re^2 \text{ with } Re = \frac{\mu d_h}{\varepsilon_t \nu}$
Kumar and Topin (2014a)	$d_h = \frac{4\varepsilon}{a_c}$	$\frac{\Delta P}{\Delta x} = E_1 \frac{(1-\varepsilon_o)^2}{\varepsilon_o^3} a_c^2 \mu V + E_2 \frac{(1-\varepsilon_o)}{\varepsilon_o^3} a_c \rho V^2$ $E_1 = \frac{\varepsilon_t \cdot d_h^2}{K_D} \cdot \varepsilon_o (\alpha/\beta)^{-1}; E_2 = C_{For} \cdot \varepsilon_t^2 \cdot d_h \cdot \varepsilon_o (\alpha/\beta)^{-1}$

2.1.1 Critical review on selection of characteristic length

In the literature, many of authors proposed different kind of correlations to predict the pressure drop in open-cell foams (a few of the author's correlation data are presented in Table 2.1). But it is well known that these correlations are usually valid only for the investigated geometry and are therefore applicable only with reduced accuracy on other porous structures. This is primarily due to the complexity of the foam morphology and discrepancies in the selection of foam geometry parameters. In that, characteristic length is one of the essential parameters in characterising the friction factor-Reynolds number (f-Re) relation in open-cell foams. This relationship is extensively dispersed throughout the literature and arises primarily due to the various choices of geometry parameters (D_p , d_s , d_p , and d_h) that can be used in characteristic length scales. Generally, this length scale is related to the flow regimes (viscous, transition or inertia regime) and may vary depending on the type of parameters used. As an illustration, Ref. Table 2.1, different authors have chosen different kind of characteristic length scales.

Initially, many authors (Liu *et al.* 2006; Innocentini *et al.* 1999; Inayat *et al.* 2011b) used to represent the analogy between solid foam and spherical particles with equivalent particle diameter (D_p) in terms of specific surface area and porosity. It leads to $D_p = \frac{6(1-\varepsilon_0)}{a_c}$. Due to the fact that open-cell foams do not have the same geometry as a packed bed of spherical particles, a relationship like this cannot be drawn because pore size and pore density change with manufacturing methods (also see Dukhan and Patel 2008). Hence it is not possible to apply this kind of relations directly to open-cell foams since they exhibit significant errors in the prediction of pressure drop.

Further, few authors (Richardson *et al.* 2000; Moreira *et al.* 2004b; Boomsma and Poulikakos 2002) were used to define characteristic length scale with pore diameter (d_p) because it can quantify easily with 3-D tomography pictures. By evaluating a substantial collection of correlations and experimental data from the literature, Edouard *et al.* (2008) demonstrated that it was inappropriate to use the d_p of the foam as a characteristic length. This is because of different ways to measure pore diameter, which

leads to inconsistencies when comparing various data from the literature. In general, the definition and measurement of d_p differ and vary depending the author and the methodology being used. By using 3-D scanned pictures, d_p can be calculated by taking the average diameter of discs covering the same area as d_p (Xu *et al.* 2008), or by taking the diameter of a sphere occupying the same volume as d_p (Kumar and Topin 2014c). And also few authors used to measure with the help of $d_p = 2.54/PPI$ expression.

Further many authors emphasised their inherent interest in using strut diameter (d_s) (Lu *et al.* 1998; Giani *et al.* 2005; Tadrist *et al.* 2004; Topin *et al.* 2006) or hydraulic diameter (d_h) (Dietrich *et al.* 2009; Kumar and Topin 2014a; Parthasarathy *et al.* 2016). Where hydraulic diameter (d_h) consists of both porosity(ε) and specific surface area(S_v) and thus includes the influence of strut shape. These elements are entirely measurable structural parameters. Then measuring those structural parameters is as precise as possible. In general, S_v could be measured with various methods e.g. BET technique (Richardson *et al.* 2000) and MRI technique (Dietrich *et al.* 2009). Recently, it can be measured easily by reconstructing the 3-D foam with micro CT scanned images (Parthasarathy *et al.* 2009). In this work, to account for the effect of strut shape, hydraulic diameter (d_h) is considered as the characteristic length in terms of ε and S_v . And it leads to $d_h = \frac{4\varepsilon}{S_v}$, and the measuring procedure of S_v is explained in chapter 1.

2.1.2 Critical review on pressure drop correlations

In the literature majority of the pressure drop correlations were carried out by using the Ergun type approach (Ref. Table 2.1). Few of the authors, e.g. Innocentini *et al.* (1999) and Lacroix *et al.* (2007) employed original values of Ergun coefficients (E1=150 and E2=1.75), which were originally derived for packed bed structures. On the other hand, some of the authors (e.g. Dietrich *et al.* 2009; Lu *et al.* 1998; Moreira *et al.* 2004b) proposed new Ergun coefficients (E1 & E2) by conducting experimental and numerical analysis on variety of foam samples with different pore sizes. Besides, many authors argued and proposed various kinds of Ergun coefficients, which vary in

the range of 100 to 865 and 0.65 to 2.65, respectively (see Table 2.1). Additionally, specific authors (Mancin *et al.* 2013 and Dukhan and Patel 2008) attempted to correlate the properties of the flow law with the geometrical parameters of the foam structure without using an Ergun type approach.

However, Numerous associations' relevance and validity have already been explored in the work of Edouard *et al.* (2008); thus, they are not covered in detail in the current work. The authors (Edouard *et al.* 2008) reported that the standard deviation between the experimental and analytical pressure drops reached 100%, proving that no model can accurately estimate the pressure drop. Bracconi *et al.* (2019) reported that among all existing correlations, the one given by Dietrich *et al.* (2009) are regarded as the most suitable estimates for pressure drop in open-cell foams where the authors have been verified using the huge collection of literature data with a range of Re as 0.1 to 10^5 . Therefore, in this study, the pressure drop correlation of Dietrich *et al.* (2009) has been taken as the reference to develop a pressure drop correlation for ideal kelvin structures.

2.2 Dispersion in open-cell foams

So far, the longitudinal dispersion through open-cell foams has been described only in a few publications. Recently, Hutter *et al.* (2011) conducted tracer pulse experiments to analyse the liquid dispersion coefficient in metal foams and laser sintered structures at various porosities (83%-86%) and pore densities (20 and 30 PPI). The authors performed experiments on two different column lengths (i.e., long and short tubes). They observed that the foam element's length played a significant role in the dispersion results, which is a well-known effect from the literature (Han *et al.* 1985). Dispersion coefficients (D_L) were observed in the range of 1.3×10^{-4} to $6.7 \times 10^{-3} m^2/s$ and reported that they follow the same trend as typical packing materials and a packed bed. Further, the authors proposed an empirical correlation for D_L as a function of Re. It is reported that the experimental data fit very well at low Re, but deviations were noticed at high $Re > 700$, and were discussed through increasing measurement error at higher

pore velocities.

Parthasarathy *et al.* (2013) performed DPLS to calculate the gaseous axial dispersion coefficient values in reticulated porous media. It is proposed that the axial mixing length could be used as the characteristic length in defining the Peclet number for reticulated porous structures with the help of Prausnitz (1958) mixing-length model. A correlation to calculate the characteristic length based on the geometry of porous media is provided.

Afshari *et al.* (2018) investigated dispersion numerically by performing DPLS in 2-D packing circular grains. The numerically generated concentration profiles were fitted to the analytical solution of the convection-dispersion equation to calculate the Longitudinal Dispersion coefficient (LDC). The authors particularly examined how heterogeneity and viscous fingering affected the miscible fluids in porous media. The authors divide the flow pattern of the miscible fluid in two ways, like stable and unstable displacement. During the flow, in the stable displacement, the LDC increases until reaching an asymptotic value, but in unstable displacements, LDC always behaves asymptotically. Last but not least, the authors also observed that the magnitude of the LDC decreased as the viscosity ratio increased to higher negative values.

More recently, V. Chandra *et al.* (2019) performed DNS on open-cell solid foams to acquire hydrodynamic dispersion. The authors modeled the open-cell solid foams by idealised Kelvin structures. In the numerical approach, the Immersed Boundary (IB) method was utilised to impose the proper fluid-solid interface boundary conditions. And the authors performed the parametric study by changing the structure's orientation at different porosities and mass flow rates. Then reported that the orientation of structure greatly influences hydrodynamic dispersion and also noted that the dispersion enhanced with the increasing flow rate due to magnified velocity fluctuations.

2.3 Forced convective heat transfer in open-cell foams

In the past decades, several researchers studied the fluid flow and heat transfer in porous media using packed bed kind of porous media and reticulated porous structures. For example, Wakao and Noriaki (1982) conducted experiments on packed beds and developed the most comprehensive correlation for Nusselt number as:

$$Nu = \frac{h_{sf} \cdot d_p}{k_f} = 2 + 1.1Re^{0.6}Pr^{0.33} \quad (2.1)$$

where, $Re = \rho d_p u_s / \mu$. Similarly, Whitaker (1983) proposed an empirical correlation for packed beds as

$$Nu = 2 + (0.4Re_d^{0.5} + 0.2Re_d^{0.66})Pr^{0.4} \quad (2.2)$$

where, $Re_d = \frac{\rho d_p u_s}{\mu(1-\varepsilon)}$, $Nu = \frac{h_{sf} \cdot d_p}{k_f} \frac{\varepsilon}{(1-\varepsilon)}$ and $d_p = \frac{6 \cdot V_p}{A_p}$.

Eq. (2.1) and (2.2) valid only in packed beds within the porosity of nearly 0.4. For higher porosities (≈ 0.9), Kuwahara *et al.* (2001) established a new correlation (Eq. 2.3a) from a series of numerical investigations based on a 2-dimensional periodic model. Later, Nakayama (2014) corrected (Eq. 2.3a) and proposed new correlations Eq. (2.3b). The authors assumed isothermal square rods as obstacles and arranged them in a regular pattern, and solved a set of governing equations. From numerical investigations, the authors suggested the need for 2-Energy equation model i.e., LTNE (Local thermal non-equilibrium) instead of LTE (Local thermal equilibrium) model. Because, while dealing with single-phase fluid flow through porous media, when assuming the LTE model, the solid and fluid phases are treated like one continuum, and the temperature is assumed to be the same. But, when it comes to heat transfer enhancement applications, the conductivity ratio between the solid and fluid phases is quite high, and thus LTE is not sufficient. Whereas, LTNE assumes a finite temperature difference between solid and fluid phases to define the heat transfer in the bulk porous structure. So, for engineering applications solving using the LTNE model is the most convenient solution. However, Pallares and Grau (2010) numerically studied the same arrangement of

staggered square rods that are used by Kuwahara *et al.* (2001). The authors proposed a new correlation (Eq. 2.3c) by multiplying a factor of two with the right hand side of Eq. (2.3a). Therefore, the results of both the studies are consistent and, in addition, are consistent with the experimental results collected by Wakao and Noriaki (1982).

$$Nu = \frac{h_{sf} \cdot D}{k_f} = \left(1 + \frac{4(1 - \varepsilon)}{\varepsilon}\right) + \frac{1}{2}(1 - \varepsilon)^{1/2} Re^{0.6} Pr^{0.33} \quad (2.3a)$$

$$Nu = \frac{h_{sf} \cdot D}{k_f} = \left(2 + \frac{12(1 - \varepsilon)}{\varepsilon}\right) + (1 - \varepsilon)^{1/2} Re^{0.6} Pr^{0.33} \quad (2.3b)$$

$$Nu = \frac{h_{sf} \cdot D}{k_f} = \left(2 + \frac{8(1 - \varepsilon)}{\varepsilon}\right) + (1 - \varepsilon)^{1/2} Re^{0.6} Pr^{0.33} \quad (2.3c)$$

In the literature, it is observed that there are two techniques for measuring heat transfer coefficient (HTC) in open-cell foams: One is a steady-state and another a transient (single-blow) method. Younis and Viskanta (1993) adopted the transient single-blow method to measure the volumetric heat transfer coefficients (VHTCs) of ceramic open-cell foams. The authors conducted experiments on different foam materials such as alumina foams of pore densities 10 PPI to 66 PPI at 85% porosity and a cordierite foam with 20 PPI of 85% porosity. From the experimental HTC results, the authors correlated the Nusselt number as function of Reynolds number for each ceramic foam ($Nu = CRe^m$). The authors observed that the exponent of the Reynolds number is decreasing while decreasing the pore diameter.

Fu *et al.* (1998) conducted experiments to estimate HTC in cellular ceramics by single-blow technique. The authors adopted the VHTC concept and defined the Nusselt number in terms of VHTC and it leads to $Nu_v = h_v l_c^2 / k$. The author performed experiments on different pore sizes of PPC (4-26), thickness (6-12mm) and Reynolds number in the range of 2-863. From the experimental outcomes, the authors performed curve-fitting regression and proposed a new volumetric Nusselt number (Nu_v) correlation to estimate VHTC. Further, the proposed correlation was compared with existing corre-

lation data and noticed a more significant deviation. The main cause of the deviation reported that due to the difference in choosing of characteristic length and also massive variation in specimen thickness.

Calmidi and Mahajan (2000b) studied the effect of thermal dispersion in high porosity metal foams. The authors conducted experiments and simulations with aluminum metal foams using air as a working fluid. The authors performed simulations with and without considering the thermal dispersion and compared it with experimental results. From the results, it was reported that the thermal dispersion term show no significant effect on the total heat transport. The authors also demonstrated that it is impossible to accurately quantify dispersion effects when the conductivity of a solid-phase material is much greater than its liquid-phase counterpart. Therefore, for the sake of simplification, dispersion terms are not included in the present study.

Hwang *et al.* (2002) examined the combined effect of porosity and flow Reynolds numbers by conducting experiments on aluminum open-cell foam. While inserting aluminum foam in a duct, the interfacial HTC's are calculated using a transient single blow technique. From the experimental results, the authors noticed that for a given Reynolds number, the interfacial HTC increases with decreasing porosity. A characteristic length based on mean pore diameter is chosen to define Nu and Re. Finally, the authors derived different empirical correlations for the Nusselt number as a function of Reynolds number, for various porosities. The correlation data provide a good agreement with Younis and Viskanta (1993) and Ichimiya. (1999) data. The authors also postulated that the convective heat transfer was significantly influenced by the shape and surface area of the flow passage. Kamiuto and Yee (2005) derived the Nusselt number versus Peclet number correlation by utilizing the experimental data of several researchers. The correlation was derived using only the porosity and nominal cell number density as parameters, and the developed correlation is able to reproduce the of experimental data in open-cell foams with error less than that of $\pm 40\%$.

To expose the metal foam as an excellent heat sink device, Hsieh *et al.* (2004) con-

ducted experiments on six types of aluminium-foam heat sinks. The authors adopted the LTNE approach and performed a parametric study to optimize the better heat transfer foam. From the results, the authors noted that for increasing higher Reynolds numbers, the convective heat transfer rate increases, causing a decrease in temperatures in the solid phase and gas phase of the aluminium foam. In addition, the authors observed that the effectiveness of cooling was influenced by both porosity and pore density. Further, the authors proposed a correlation for each aluminium foam in the form of $Nu = aRe^b$. Where the constants a and b increased with increasing porosity and pore density.

Fuller *et al.* (2005) conducted experiments on open-cell foams using a steady-state method and compared it with the transient method. The authors reported that the HTC obtained from the steady-state approach inherently depends upon the foam thickness and thermal conductivity because of the heat source positioned on the channel's side surface. In contrast, the transient method is assumed independent of foam thermal properties. As a result, the conduction effect is not a problem. The authors also proposed two different mechanisms which enhance the heat transfer in open-cell foams. One is the increase of heat transfer from the bounding substrate walls by making the flow more turbulent. Sometimes it referred to as 'thermal dispersion'. Another mechanism is that open-cell foams offer extended surface area, which consequently enhances the heat transfer.

Wu *et al.* (2011) have performed a sensitivity analysis on ceramic foams to obtain HTC. The authors represented the ceramic foams by idealized tetrakaidecahedron structure. By performing the numerical simulations, the local wall HTC was determined. The authors noticed that the HTC is significantly affected by cell size, velocity and was poorly affected on porosity. Based on simulation results, a correlation for the VHTC was developed between air and open-cell ceramic foam. The main intention of their correlation is to design a volumetric solar air receiver. Thus, the developed correlation was compared with the experimental results of Younis and Viskanta (1993) and reported that the comparison shows good agreement.

Bianchi *et al.* (2013) performed experimental and numerical analysis to determine the WHTC in a catalyst reactor where the open-cell foam material was tight-packed in the tubular reactor. The foam samples used for the experiments were made up of FeCrAlY or aluminium with a pore size of 10 to 40 PPI and porosities of 89-95%. The authors specially focused on the interaction between the reactor wall and the foam packing, allowing N_2 or He at a flow rate of 15 to 35 NI/min (normal liter per min). For that, the authors collected longitudinal and lateral temperature profiles along the tested samples and the reactor wall within a range of 400 to 800 K. Then they determined the WHTC and effective conductivity for each run using nonlinear regression, as well as a pseudo-homogeneous 2D heat transfer model. From the results, the authors reported that the WHTC resistance was highly influenced by the gas conductivity and the foam shape and weakly influenced by the flow velocity. Further, the authors derived a new WHTC correlation relating to foam structural parameters (see Table 2.2). The proposed correlation compared with Edouard *et al.* (2010) data and reported that even though it's a different material, the correlation matches well with Edouard *et al.* (2010) results.

Dietrich (2013) conducted experiments to evaluate the HTC in various ceramic sponges at different porosity and pore size. The authors observed a significant impact of flow velocity and foam geometry properties on heat transfer. Based on the experimental outcomes, the authors correlated the Nu-Re analogy to predict the HTC (see Table 2.2). Further, the authors adopted the GLE approach (Eq. 2.4) and proposed a new Nu correlation in terms of non-dimensional pressure drop i.e., the Hagen number (shown in Table 2.2).

$$Nu = 0.4038 \cdot \left(2 \cdot x_{\text{friction}} \cdot Hg \cdot Pr \cdot \frac{d_h}{L} \right)^{\frac{1}{3}} \quad (2.4)$$

Where x_{friction} denotes the fraction of total pressure drop, L is the characteristic length, and d_h is the hydraulic diameter. In general, the GLE approach was developed to find heat transfer in packed beds and heat exchangers with the help of pressure drop data. The author utilised that advantage and proposed a universal correlation for predicting

heat transfer in ceramic foams with available pressure drop data. Further, Parthasarathy (2016) also proposed a similar kind of correlation (see Table 2.2) by replacing the 'L' with axial mixing length by incorporating the mixing length theory.

Kamath *et al.* (2013) studied convective heat transfer in a vertical tube that was filled with aluminium and copper metal foams. The study was conducted using three different metal foam thicknesses of 10, 20 and 30 mm with the same PPI (10 and 20) but various porosities, respectively. From the experimental results, the authors observed that the foam thickness has a significant impact on heat transfer and finally the authors concluded that copper metal foams were shown to have better heat transfer performance than aluminium foams by 4 %.

Zafari *et al.* (2015) investigated numerically fluid flow and heat transfer in open-cell foams. The authors reconstructed the foam geometry with microtomography images and performed simulations of a foam having higher porosities of 85-95%. The simulation results reported that the existence of a high thermal gradient at the inlet of the porous causes density changes in the inlet region, resulting in an acceleration of airflow up to 1.7 times that of the inlet velocity. In addition, within a short distance, this process leads to establishing thermal equilibrium between the foam strut and air. Further, the authors compared the simulation results with the existing results of experiments and reported a good agreement. Based on the simulation results, the authors proposed a new Nu correlation in terms of foam porosity and Re, as shown in Table 2.2. The authors strictly reported that the proposed correlation is valid within the range of Re as 2-20 and porosities of 85 to 95%.

Lin Xia *et al.* (2017) conducted experiments to analyze heat transfer behaviour in open-cell foam through forced airflow convection. The authors performed experiments on various foams materials of Cu, Ni and SiC with different pore diameters and high porosities (0.87 to 0.97). The foam samples are heated by allowing hot air in the range of velocity 2.0 to 9.0 m/s. By applying inverse analysis, the authors computed the VHTC with the help of transient temperature data. The authors noticed that the VHTCs

increase with a decrease in porosity and decrease as PPI decreases vice versa. Thus, the experimental results were compared with seven different data available in the literature. Out of seven data, the author's experimental data well fits with the correlation of Dietrich (2013). Additionally, based on experimental results, the authors proposed a simple correlation to estimate the VHTCs. The consistency of correlation was examined by comparing it with the author's own and other author's experimental data. Therefore, the author concluded that the proposed correlation matched reasonably with existing experimental data with error of $\pm 40\%$.

Sinn *et al.* (2021) performed quantitative structure-heat transport analysis on periodic open-cell foams. The authors performed CFD simulations on five different Kelvin-cell lattice structures. The authors specially focused on the heat generation in a solid strut. From the simulation results, the authors observed that the strut diameter and thermal conductivity are the dominant structural characteristics to govern heat removal in periodic open-cell foams. In contrast, the authors also noticed that the cell diameter does not affect that heat removal, but fluid velocity has a significant influence only on materials with low solid thermal conductivity. Based on the results, the authors derived the structural versus heat transport relation that could help to use in catalyst carriers.

Sepehri and Siavashi (2022) presented a pore-scale analysis of fluid flow and convection conduction heat transport in open-cell metal foams. Using the Laguerre–Voronoi tessellations (LVT) algorithm, the authors constructed geometries with the same pore density of 20 PPI and different porosities (76.6%, 84.4%, and 93.8%). The snappy-HexMesh tool was used to build the computational grid. Next, heat transfer and flow analysis were carried out using the OpenFOAM open-source library and examined the influence of porosity, foam material, and flow rate. From the pore-scale results, the authors reported that decreased porosity causes subsequent increases in heat transfer and pressure drop. Finally, the significance of conduction through the porous structure in the total heat transfer rate was determined by solving problems with and without conduction in solid matrix. From that, the authors noticed that the conductive heat transfer

through the porous matrix significantly affects the total heat transfer rate, particularly in high Reynolds numbers. Further, the authors validated the numerical results with existing empirical and experimental data.

2.3.1 Critical review on HTC correlations

The 3-Dimensional and random structure has significantly constrained the experimental research of the HTC for open-cell foams. In the literature, numerous correlations were reported to estimate the heat transfer in open-cell foams. A few available correlations are listed in Table 2.2. It is observed that few authors (Younis and Viskanta 1993; Hwang *et al.* 1995; Kamiuto and Yee 2005; Lin Xia *et al.* 2017) correlated the Nusselt number as a function of the Reynolds number using a generalized form of power law i.e., $Nu = CRe^m$. On the other hand, few authors adopted the GLE approach (Dietrich (2013); Parthasarathy 2016), and others attempted to derive based on geometry parameters (Bianchi *et al.* 2013; Zafari *et al.* 2015; Wu *et al.* 2011). Besides, few authors Bianchi *et al.* 2013 proposed to predict wall heat transfer coefficient. It is well known that these correlations are valid to their respective geometry and, therefore only somewhat accurate when applied to other porous structures. As discussed previously, this diversification is mainly observed due to the complexity of foam geometry and differences in the selection of characteristic lengths.

However, the real porous structures are manufactured using the Schwarzwalde process (Achenbach 1995; Fu *et al.* 1998; Ichimiya. 1999; Calmidi and Mahajan 2000b; Richardson *et al.* 2003; Kamath *et al.* 2013; Mancin *et al.* 2013) etc. But, due to the complexity of geometry, the manufacturing process is challenging to reproduce the same structures. For example, in the manufacturing process, even if the same PPI, there are open pores, closed pores, and partially open and partially closed pores. Due to their closed and partially closed pores, the specific surface area will get affected, and it leads to diminishing the efficacy of convective heat transfer. As a result, the foam structure can affect the flow path, flow structure and the HTC of the porous media.

Table 2.2: Heat transfer correlations proposed by different authors for open-cell foams.

Authors	Characteristic length(C_L)	Correlation for predicting the heat transfer coefficient
Younis and Viskanta (1993)	d_p	$Nu_v = 0.819 [1 - 7.33 (d_p/L)] Re_d^{0.36[1+15.5(d_p/L)]}$
Hwang <i>et al.</i> (1995)	$D_p = 20.346(1 - \varepsilon)\varepsilon^2/a_{sf}$	$h_{sf} = \begin{cases} 0.004 \left(\frac{4\varepsilon}{d_{pr} a_{is}} \right)^{0.35} \left(\frac{k_f}{d_{par}} \right) Re_{p\ par}^{1.35} Pr^{1/3}, & Re_{par} \leq 75 \\ 1.064 \left(\frac{k_f}{d_{px}} \right) Re_{par}^{0.59} Pr^{1/3}, & Re_{par} \geq 350 \end{cases}$
Kamiuto and Yee (2005)	$d_s = 2d_n C / \sqrt{\pi}$ $C = 0.5 + \cos [(1/3) \cos^{-1}(2\varepsilon - 1) + 4\pi/3]$	$h_v d_s^2 / k_f = 0.124 (\rho_f u d_s / \mu_f Pr)^{0.791}$
Wu <i>et al.</i> (2011)	d_{Cell}	$Nu = 2.0696 \cdot Re^{0.438} \cdot \varepsilon^{0.38}$ $Nu = \frac{h \cdot d_{Cell}}{k_F}, Re = \frac{u_0 \cdot d_{Cell}}{\nu_F}$
Dietrich (2013)	$d_h = \frac{4\varepsilon}{S_v}$	$Nu = h_{sf} d_h / k_f = 0.31 \cdot Hg^{\frac{1}{3}} \cdot Pr^{\frac{1}{3}}$
Bianchi <i>et al.</i> (2013)	d_C	$h_W = \frac{k_f}{d_C} (7.18 + 0.029 Re_{d_C}^{0.8}); 4 < Re_{d_C} < 255$
Zafari <i>et al.</i> (2015)	\sqrt{K}	$Nu_K = 0.016 + 0.16 \times \varepsilon^{-3} \times Re_K^{0.28}$
Parthasarathy (2016)	$d_h = \frac{4\varepsilon}{S_v}$	$Nu = 0.17 (Pr d_h / L_d Hg)^{1/3},$ <i>where</i> $L_d = l_l$
lin Xia <i>et al.</i> (2017)	d_p	$Nu_v = h_v d_p^2 / k_f = 0.34 \varepsilon^{-2} Re_d^{0.61} Pr^{1/3}$

In addition, it is difficult to measure accurate geometrical parameters (such as porosity, pore diameter, specific surface area, and flow tortuosity). To overcome those ambiguities, in this study, well-defined structures i.e., ideal and randomized Kelvin structures are used to study the fluid flow, and heat transfer in detail.

2.4 Scope and objectives of present work

To numerically calculate the fluid and heat transport phenomena in the solid and the fluid phase together require the exact geometrical description of the solid bounding phase. The difficulty in describing the solid phase geometry and the requirement of high computational memory and processing power to solve the conservation equations within the porous domain necessitated a macroscopic continuum approach to describe the transport process. The effect of the solid phase on the transport process within the voids is defined mainly through semi-empirical correlations. The semi-empirical correlations are influenced by the accuracy in which the solid phase geometry is described and thus affects the accuracy of the continuum approach. However, in the literature, there have so many correlations available based on randomized porous structures that are manufactured using processes like the ‘Schwarzal process’. But it is well known that these correlations are usually valid only for the investigated geometry and are therefore applicable only with reduced accuracy on other porous structures. This is primarily due to the complexity of the inner morphology of open-cell porous foams. In order to develop accurate generalized semi-empirical correlations for the effective transport properties, the influence of each and every geometrical property on the fluid and heat transport properties needs to be studied in detail. In order to perform such analysis, in this study, well-defined structures i.e., ideal and randomized Kelvin structures (See Figure 3.3) are used to run simulations of different PPI of 10, 20 and 30, and porosities (80%, 85%, and 90%) considering various working fluids (air, water & saltwater). The geometry of these structures is constructed with the aid of in-house code and visualization tool kit (VTK) libraries. By varying the geometrical parameters, the influence

on pressure drop and heat transfer characteristics between the flowing fluid and solid phase of foams are investigated. For this reason, the momentum and energy equations for forced convection in reticulated structures are solved by the standard CFD-FVM approach. Based on the simulation outcomes, a new correlations are proposed for the ideal Kelvin structure, and it was compared with numerical and experimental results of real porous structures that are available in the literature.

2.4.1 Objectives of the present work

1. To develop the micro structure of reticulated porous media based on ideal Kelvin structure and to discretize the domain to obtain computational grids. To calculate the flow and heat transfer within the structures with the help of a CFD software.
2. To study the effect of geometric parameters such as pore density, porosity and specific surface area on the pressures drop, convective heat transfer, longitudinal dispersion with the help of CFD simulation results.
3. To study the effect of random orientation of the struts on the transport properties of the reticulated porous media with the help of simulations.
4. Based on the above mentioned studies, the final expected outcome is to develop generalized nondimensionalized correlations for
 - (a) Pressure drop (Hagen number as a function of Reynolds number)
 - (b) Convective heat transfer (Nusselt number in terms of Hagen number and Prandtl number)
 - (c) Longitudinal dispersion coefficient (Longitudinal Peclet number in terms of molecular Pectel number).

2.5 Expected output and outcome of the present work

The research output from the proposed work would be significant in contributing towards a comprehensive understanding of the effect of reticulated porous structure ge-

ometry on the transport properties of porous media. The project aims in developing accurate models to calculate the heat and mass transfer through porous media. Accurate non-dimensional correlations or models would help in studying various applications where porous media are used and will help in developing efficient engineering applications such as porous combustors and volumetric solar reactors.

2.6 Closure

A comprehensive literature review on fluid flow and heat transfer in open-cell foams with existing correlations was reported in detail in this chapter. The scope and objectives of the present research work were presented at the end of this chapter. The geometry modelling of the Kelvin structure is explained in the next chapter.

CHAPTER 3

GEOMETRICAL MODELLING OF KELVIN STRUCTURE

In the literature, there are three different approaches available for the calculation of the heat transfer and pressure drop in porous media. The first one is an experimental method. The HTC estimated by allowing a stream of hot air/fluid into a metallic/ceramic foam (manufactured) at varying velocity, porosity, and pore density values using the transient method (Dietrich 2013; Younis and Viskanta 1993; Mancin *et al.* 2013; Hwang *et al.* 2002; Lin Xia *et al.* 2017) and also steady-state method (Calmidi and Mahajan 2000b; Fuller *et al.* 2005). The second method is like reconstructing the real foams through computer tomography, or 3D imaging technique, i.e., a digital representation of physical samples are used to perform numerical solutions (Nie *et al.* 2017; Diani *et al.* 2015; Parthasarathy 2016; Meinicke *et al.* 2017). The second method is more economical than the experimental method, but problems persist in accurately representing the real structure. Finally, the third method is based on computationally constructed through computer code or using 3D modelling software (Kopanidis *et al.* 2010; Moon *et al.* 2018; Cunsolo *et al.* 2015; Wu *et al.* 2011). This method is well suitable for representing ideal geometry as the real foam geometry as best as possible. However, in the literature, many idealized foam geometry models are available, such as, cubic cell model (Ghosh 2009; Lacroix *et al.* 2007), body centered model, face centered model (Krishnan *et al.* 2006), Weaire-Phelan's model and Kelvin's tetrakaidekahedra models (Boomsma *et al.* 2003; Cunsolo *et al.* 2015) were used to analyse the pressure drop and convective heat transfer in open-cell foams numerically. In theory, Wu *et al.* (2011) reported that among all existing models, the Weaire-Phelan's model and Kelvin cell models are better able to representing prototypical geometries of real porous structures. Due to the complexity in generating Weaire-Phelan's model, the authors suggested us-

ing the Kelvin cell model. Similarly, Cunsolo *et al.* (2015) analysed and compared both models at equal cell size and suggested that the Kelvin model, which is less complicated than the Weaire–Phelan model, can be employed without compromising accuracy. Therefore, in this study, reticulated porous structures are modeled using the theoretical Kelvin model, representing the real porous structures as shown in Figure 3.1. The modeling of geometries are done using an in-house code along with the use of visualization tool kit (VTK) libraries with the following procedure.

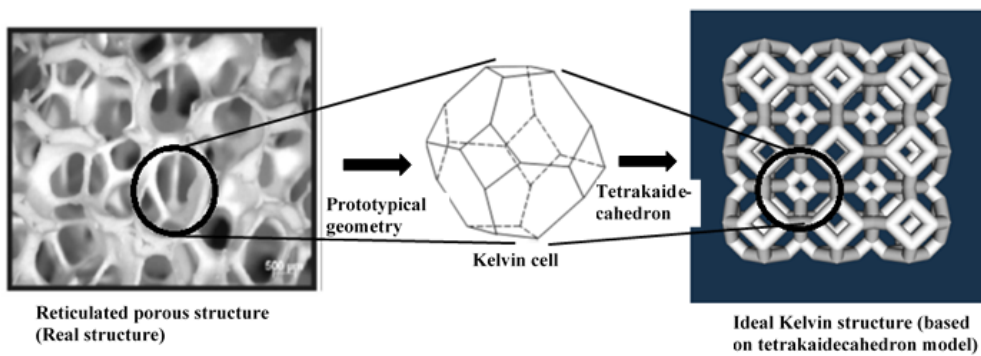


Figure 3.1: Reticulated real and ideal open-cell foam samples

3.1 Procedure to construct Kelvin structure

The Kelvin cell geometry (truncated octahedron) consists of 14 faces and the vertices (intersection nodes) are modeled as spheres and the struts as cylinders with the following steps.

1. Initially, the struts are generated using `vtkTubeFilter` (see Figure 3.2b). By defining the start and end points for the given line and tube radius, the `vtkTubeFilter` will generate the tubes around the specified line.

2. Further, the spheres are constructed with the help of `vtkSphereSource`. It generates a sphere with a specified radius that is centred at the origin and represented by polygons (see Figure 3.2a) and also needs to specify the resolution in both latitude (ϕ) and longitude (θ) directions. The radius of the spheres is defined 5% larger than the

radius of the struts.

3. By providing the open porosity as input, the program creates a unit Kelvin structure. Then the unit Kelvin structure is scaled based on PPI.

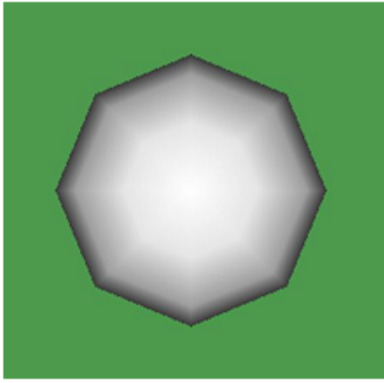
4. The pore diameter is calculated from the PPI using the relation $d_{pore} = 0.0254/PPI$ (Hackert *et al.* 1996) and a cube that encloses the Kelvin structure is made. The volumes of all the 24 spheres and 36 cylinders are calculated using an initial guess radius. By equating the solid volume calculated for the enclosing cube with the porosity value, and the solid volume calculated using the volumes of both cylinders and spheres. The radius of the struts is found up to a 7 decimal point accuracy using an iterative bisection method.

5. By providing number of cells as input in all three directions the basic Kelvin structure is mirrored as per input to create an ideal reticulated Kelvin structure having the required number of cells.

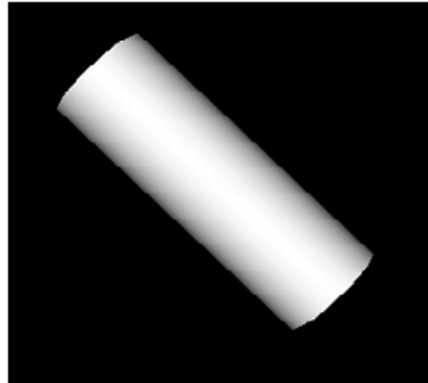
6. The next step is to randomize the ideal structures. In order to mimic the real structure the idealized Kelvin structure is randomized, but the geometrical parameters such as PPI, porosity and specific surface areas will be kept the same as ideal structures. This will help in studying the influence of randomization on transport properties.

7. The percentage of randomization is a factor that determines the percentage of individual Kelvin structures in the array that will be affected by the scale and centroid factors with respect to the original position. Real structures have a range of pore sizes. So in order to mimic those conditions, the upper and lower limit of pore sizes can be specified, and the program assigns a random size in between the aforementioned range to each pore. Moreover, the percentage of pores that need to be scaled can be controlled.

8. The displacement of the centroids of each pore is similarly governed by the maximum and minimum percentage of displacements allowed. A cell is allowed to move in the voids created if the cell's size or the size of any of the cells in its vicinity is reduced. The amount of displacement is restricted according to the percentages men-



(a)

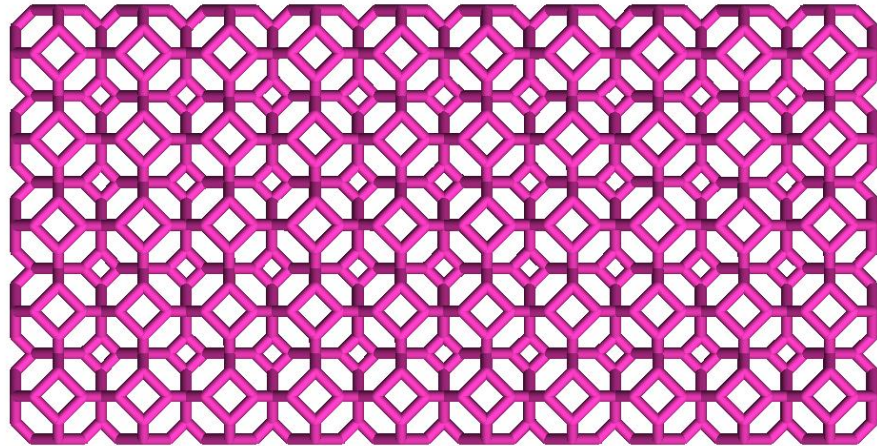


(b)

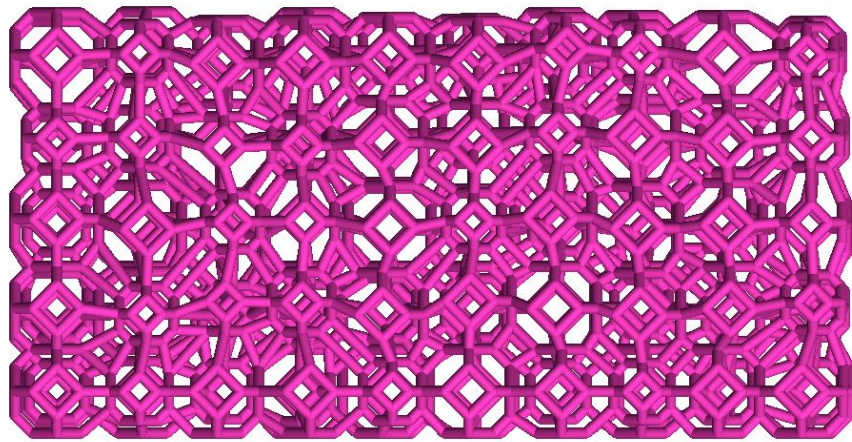
Figure 3.2: (a) Sample sphere constructed in VTK (b) Sample strut constructed in VTK.

tioned. The program assigns random displacement to the centroid from the given range, and different randomized structures are generated (Ref. Figure 3.3b).

Therefore, the modeled RPS structure of ideal and randomized Kelvin structures are shown in Figure 3.3. After developing the Kelvin structure, the surface data of each structure will be imported to a grid generating software to generate the computational grids. The expected no. of grid points is around 10-40 million for a structure size of $5\text{cm} \times 2.5\text{cm} \times 2.5\text{cm}$. The structures that are created for the study are provided in Table 3.1.



(a)



(b)

Figure 3.3: Kelvin modelled porous structures : (a) Ideal Kelvin structure (b) Randomized Kelvin structure (both scale and centroid factor)

Table 3.1: Structures that are considered for simulations

Ideal structure	
Pore density (PPI)	Porosity
10 PPI	80%
	85%
	90%
20 PPI	80%
	85%
	90%
30 PPI	80%
	85%
	90%
Randomized structure	
10 PPI	80%
	85%
	90%

3.2 Closure

The geometry selection and modelling procedure using a program algorithm were thoroughly described in this chapter. Further, the constructed computational geometry was used to analyze pressure drop, dispersion and heat transfer coefficient which are discussed in the next chapters.

CHAPTER 4

FLUID FLOW IN RETICULATED KELVIN STRUCTURE

4.1 Introduction

Looking into the theoretical background, the fluid flow in porous media has a greater flow resistance in comparison to fluid flow through the channels or tubes of the same dimension. The first measurement of increase in resistance to the fluid flow through porous media was experimentally measured by Darcy (1856). Darcy's experiments show that flow velocity at low Reynolds number ($Re < 1$), the pressure drop inside a porous domain is dependent on the geometry of the porous matrix. The pressure drop equation is given by Darcy

$$\frac{dp}{dx} = -\frac{\mu}{K}u_s \quad (4.1)$$

Flow at high Reynolds number ($Re > 1$), the inertial resistance can also become significant because of the nonlinear behavior of pressure gradient versus flow velocity (Bejan and Poulikakos (1984)). To account for the increase in pressure drop the inertial term is added along with the viscous term, then Darcy's Eq. (4.1) is modified as

$$\frac{dp}{dx} = -\frac{\mu}{K}u_s - c_F K^{-0.5} \rho u_s^2 = -\frac{\mu}{K_1}u_s - \frac{\rho}{K_2}u_s^2 \quad (4.2)$$

The last phrase in the Eq. (4.2) is known as the Forchheimer term, and the total equation is called a Darcy-Forchheimer equation. Where K_1 and K_2 are termed as permeability coefficients i.e., the measure of flow conductance in porous media and the drag, respectively. Where, u_s is the superficial velocity and defined by dividing the volume flow rate of fluid by total cross-sectional area of the porous domain.

In the literature, the majority of the pressure drop studies (Parthasarathy *et al.* 2016; Kumar and Topin 2017; Dietrich *et al.* 2009; Moreira *et al.* 2004a; Lacroix *et al.* 2007; Liu *et al.* 2006; Richardson *et al.* 2000) on reticulated porous structure were carried by using Ergun correlation.

General Ergun correlation for pressure drop in packed bed is expressed as:

$$\frac{\Delta p}{L} = 150 \left(\frac{\mu u_s}{d_p^2} \right) \frac{1 - \varepsilon^2}{\varepsilon^3} + 1.75 \left(\frac{\rho u_s^2}{d_p} \right) \frac{1 - \varepsilon}{\varepsilon^3} \quad (4.3)$$

In packed beds, the correlation of pressure drop is described from the fundamental theory of friction factor (Ergun 1952; Bird 2002; Dietrich *et al.* 2009)

$$f = \frac{\Delta p \varepsilon^2 d_h}{\Delta x \rho u_s^2} = A/Re + B \quad (4.4)$$

And with $Re = \rho \cdot u_s \cdot d_h / \varepsilon \cdot \mu$ in Eq. (4.4), the pressure drop equation for RPS is proposed by Dietrich *et al.* (2009):

$$\frac{\Delta p}{\Delta x} = A \cdot \frac{\mu}{\varepsilon d_h^2} u_s + B \cdot \frac{\rho}{\varepsilon^2 d_h} u_s^2; Hg = A \cdot Re + B \cdot Re^2 \quad (4.5)$$

where $d_h = \frac{4\varepsilon}{S_v}$ in Eq. (4.5). A similar pressure drop equation is used by Parthasarathy *et al.* (2016):

$$\frac{\Delta p}{\Delta x} = \zeta \cdot \frac{\mu S_v^2}{\varepsilon^3} u_s + \eta \cdot \frac{\rho S_v}{\varepsilon^3} u_s^2 \quad (4.6)$$

where S_v is the specific surface area, ζ and η are the viscous and inertial coefficients and Eq. (4.6) is the basic equation of Ergun and Orning (1949).

4.2 Problem statement

From the literature review, it was observed that different authors proposed different kinds of pressure drop correlations with large errors because of the complex shape of open-cell foam geometry, materials and discrepancies in the selection of open-cell foam geometry parameters. In this chapter, the ideal and randomized Kelvin structures at

different poroisties and pore densities are used to study the pressure drop and to seek the possibility of using the existing correlation (Dietrich *et al.* 2009) to calculate the pressure drop in porous media and to compare the results with existing experiments results of real porous structures.

4.3 Numerical setup and post-processing

4.3.1 Governing equations and boundary conditions

As reported by Diani *et al.* (2014), to achieve a flow to be fully developed, the domain size has to maintain nearly 10 pores in the direction of flow in DPLS. Therefore, in the present study, the domain size of a minimum 10 and maximum of 15 pores are maintained in the flow direction to attain a fully developed flow condition. The simulations are performed using ANSYS CFX solver with the following conditions. The working fluid is assumed as incompressible air, steady-state and isothermal condition (298 K) are considered. The flow is calculated by solving the governing equations of continuity and momentum

$$\frac{\partial}{\partial x_j}(\rho u_j) = 0 \quad (4.7)$$

$$\frac{\partial}{\partial x_j}(\rho u_j u_k) = -\frac{\partial p}{\partial x_k} + \frac{\partial}{\partial x_j} \left(\mu \frac{\partial u_k}{\partial x_j} \right) \quad (4.8)$$

where u denotes the superficial velocity in the direction of j or k and x denotes the Cartesian coordinate direction, p is the pressure, ρ is the density of air, μ stands for the dynamic viscosity of air. The properties of air are considered at 1 atmospheric pressure and temperature of 298 K, with density of 1.185 kg/m^3 and the dynamic viscosity of $1.8311 \times 10^{-5} \text{ Ns/m}^2$. The governing equations are solved using commercial CFD software (ANSY CFX) by finite volume discretization approach with a hybrid interpolation scheme. The boundary conditions specified in the current work is shown schematically in Figure 4.1 and is discussed below:

1. The inlet boundary condition defined is uniform velocity at the entry of the

domain.

2. Static pressure-outlet with zero gradient condition at the exit of the domain.
3. The lateral aspects of the domain is specified with periodic boundary conditions.
4. The interface between the fluid and solid domain is defined by a wall with no-slip boundary condition.

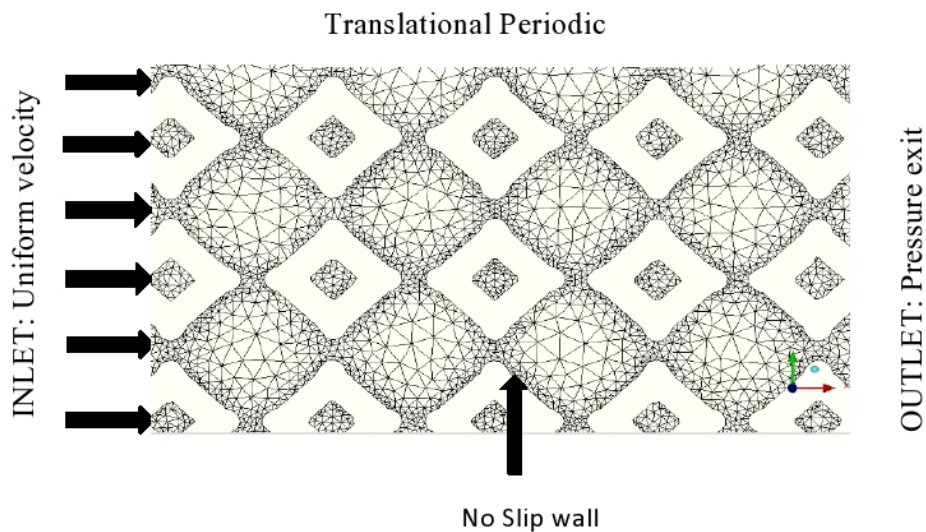


Figure 4.1: Ideal Kelvin structure's grid generated using ICEM CFD and imposed boundary conditions.

Further, the flow conditions are assumed to be laminar for the selected Reynolds numbers. Della Torre *et al.* (2014) performed simulations for Reynolds number range between 0.1 to 1000 with three different modeling approaches like DNS, laminar steady-state and RANS steady-state with a $k-\omega$ SST turbulence model. The authors observed and reported that pressure drop predictions are same in three approaches and suggested that the simulations in open-cell foam can be addressed by use of simple laminar flow for Reynolds number below 1000. In this study, laminar flow models have been used.

4.3.2 Grid independence study

The in-house code generates surface data of the geometries, and the data are imported to a commercial grid generating software (ICEM CFD) to obtain the computa-

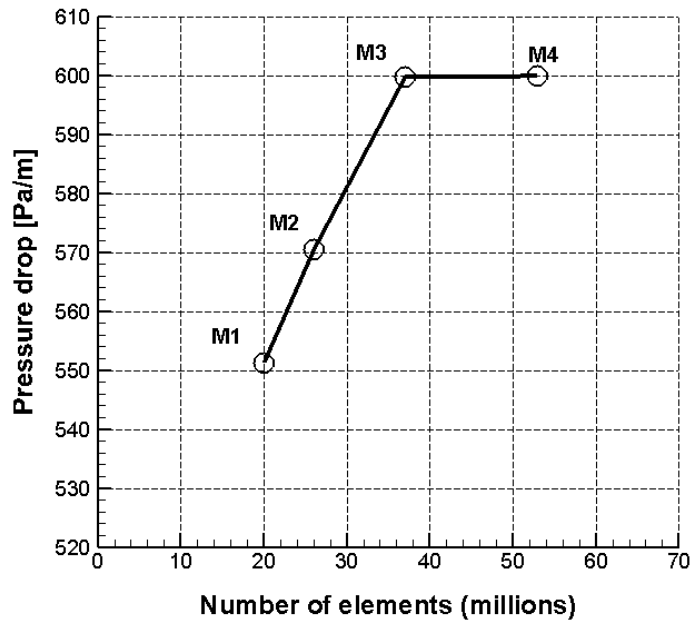


Figure 4.2: Grid independence study for 30 PPI 80% porosity ideal structure at $Re=10$

tional meshes. In order to reduce the computational time and numerical errors, grid independence studies are carried out for four different grid sizes (M1, M2, M3 and M4) at two different Reynolds numbers (750 & 10) shown in Figure 4.2 & 4.3. As the no. elements are increased in the simulation domain, the difference in pressure drop results approach the minimum. In Figure 4.2 & 4.3, the pressure drop values are plotted against no. of elements to check the variation with each grid. Among four grids, M3 and M4 simulation results are independent of the mesh resolution. Looking into M3 & M4, M3 has a fewer number of elements. Therefore, in order to reduce the computational time in this study, 37 million elements (M3) grids are used for further simulations. Similar studies has been done for other porous structures.

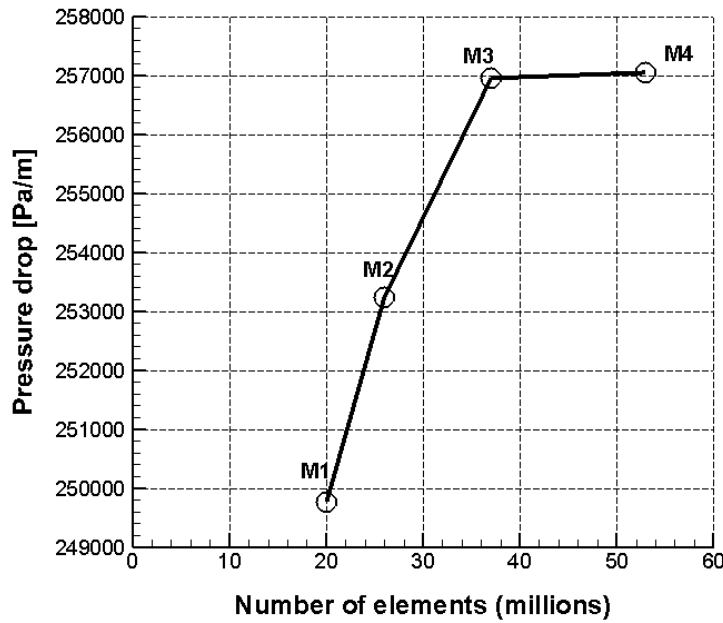


Figure 4.3: Grid independence study for 30 PPI 80% porosity ideal structure at $Re=750$

4.4 Results and discussion

4.4.1 Simulation results

The DPLS analysis are carried out for Reynolds numbers 10, 100, 500 and 750 (within laminar range) and the Reynolds numbers ($Re = \rho d_h u_s / \varepsilon \mu$) are calculated using the hydraulic diameter ($d_h = 4\varepsilon / S_v$) as the characteristics length. As an example, nondimensionalized pressure profiles along the flow direction are shown in Figure 4.4. As expected, it can be observe that the pressure drop increases with Reynolds number. For very low Reynolds numbers, the curve tended down indicating the Darcy regime. Similar result exhibit in the case of randomized structures shown in Figure 4.5. In Figure 4.5, the naming is done in the format i-j-k, where i: percentage randomization, j: scale factor (65: 60-65% and 75: 70-75%) and k: centroid factor (30: 20-30% and 40: 30-40%). Even though there is a rise in the pressure drop with randomization, almost all cases exhibit a pressure drop in a relatively close range.

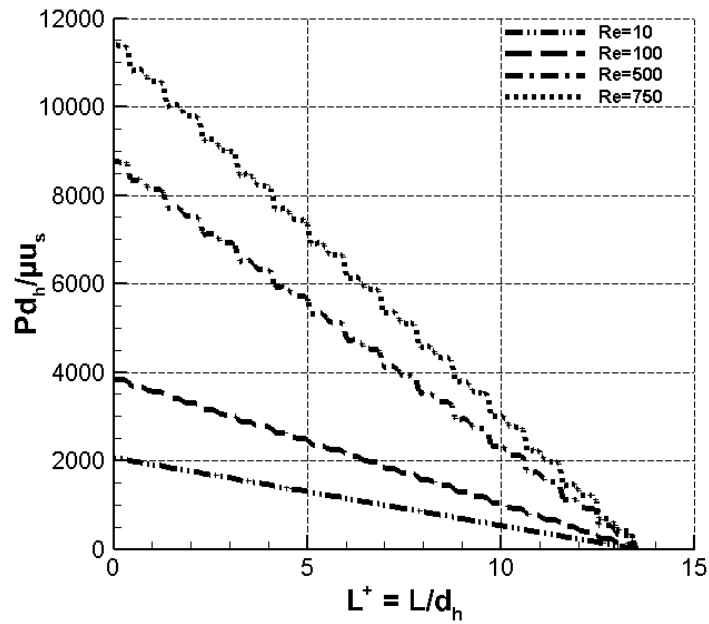


Figure 4.4: Nondimensionalized pressure profiles along the flow field in 30 PPI 85% porosity ideal structure for different Reynolds numbers.

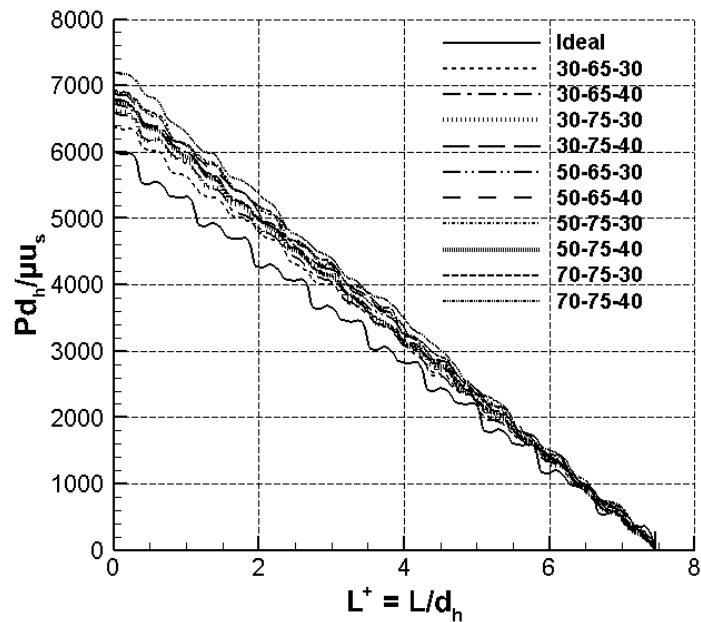


Figure 4.5: Nondimensionalized pressure profiles for $Re=750$ for all randomized cases of 10 PPI 90% porosity (comparison between ideal and randomized structures).

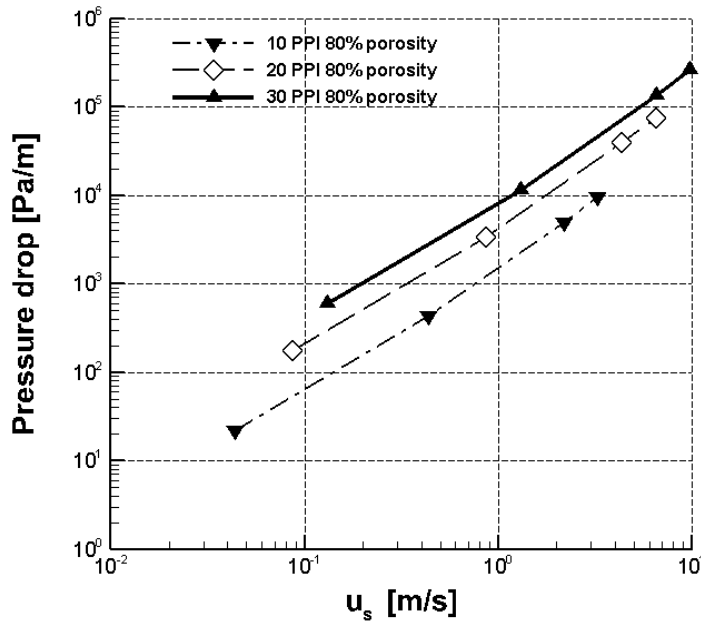


Figure 4.6: Pressure drop versus velocity for ideal structures at 80% porosity with different PPI.

From Figure 4.6, it is seen that for a constant porosity, the pressure drop increases with increasing pore density (PPI). This is due to the increase in the specific surface area with respect to PPI (Ref. Table 4.1), i.e., a higher PPI results in a denser packing of struts. The pressure drop in the ideal Kelvin structures follows a predictable trend, where it decreases with increasing porosity as in Figure 4.7. This effect is primarily due to the reduction in the strut diameter (d_{strut}), which caused a decrease in specific surface area when the porosity is increased, keeping PPI constant. The same effect of porosity on the specific surface area is the reason for the reduction in pressure drop, even in the case of randomization (Ref. Figure 4.8). It was observed that for low-velocities, the pressure drop is linear with respect to flow velocity i.e., Darcy regime. But for higher velocities, it becomes nonlinear and following the second-order polynomial (i.e., quadratic behavior) because of the transition of the regime from Darcy regime to Darcy –Forchheimer regime.

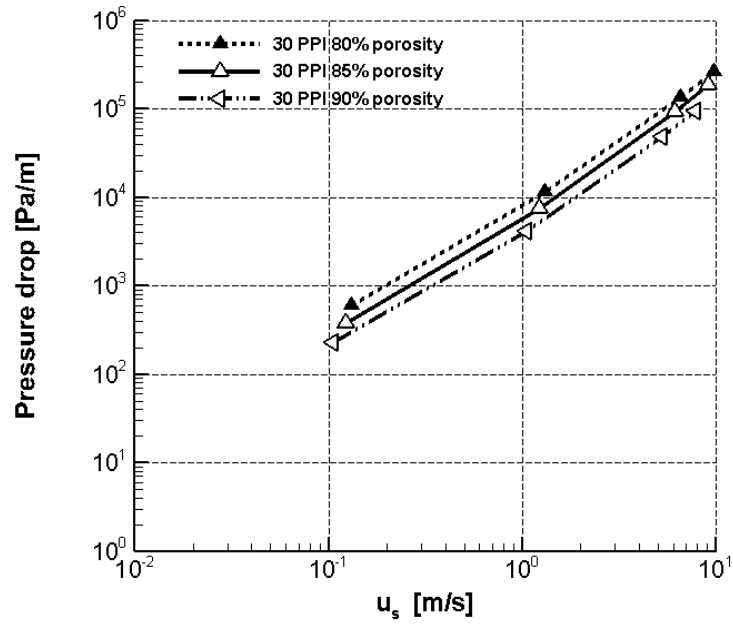


Figure 4.7: Pressure drop versus velocity for ideal structures at 30 PPI with different porosities.

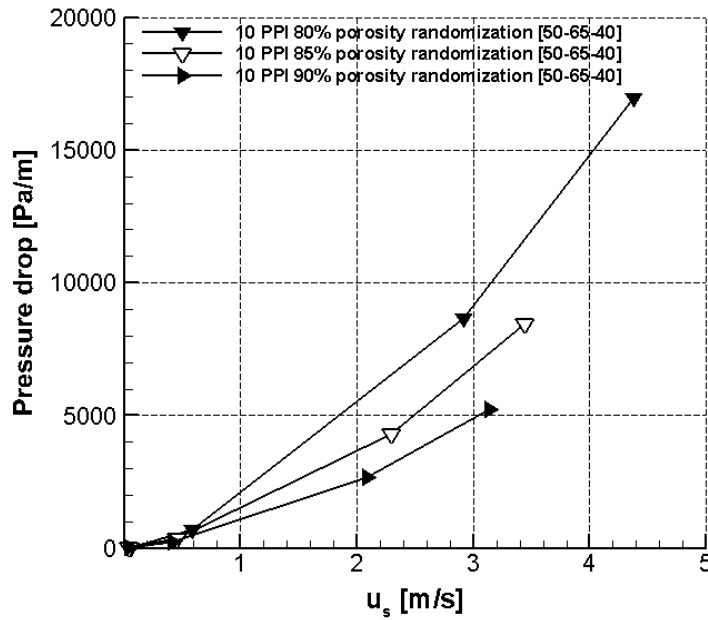


Figure 4.8: Pressure drop versus velocity for randomized structures at 10 PPI with different porosities.

As expected, the pressure drop trends in ideal structure are same as like real structures that are available in the literature (Parthasarathy *et al.* (2016); Kumar and Topin (2017); Dietrich *et al.* (2009); Moreira *et al.* (2004a); Lacroix *et al.* (2007); Liu *et al.* (2006); Richardson *et al.* (2000)). When the Kelvin structure was randomized by scale and centroid factor, it clearly seems to increase pressure drop along with the percentage of randomization (Ref. Figure 4.9) (The percentage of randomization is explained in section 2). From Figure 4.9, it is observed that even if same porosity and PPI is maintained in both ideal & randomized structures, there is a change in pressure drop due to randomization. The specific surface areas of the all structures are maintained to have nearly the same value. (Ref. randomization structure tables in appendix I.4).

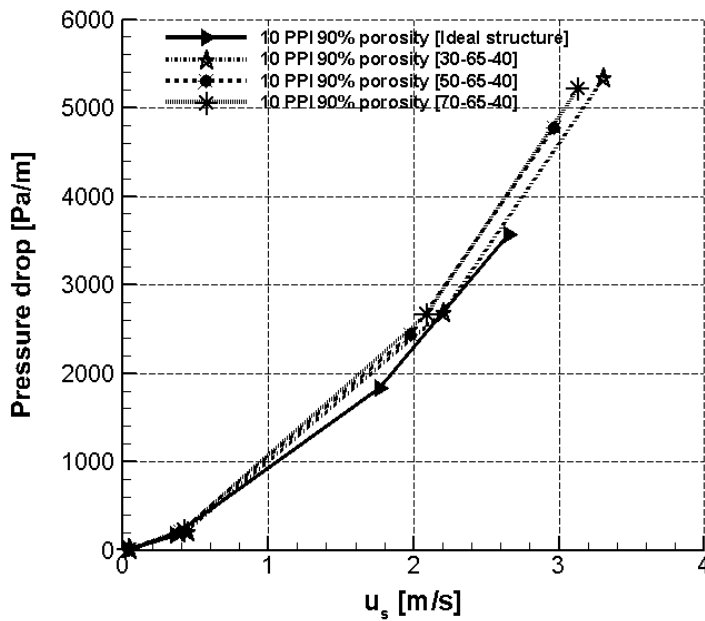


Figure 4.9: Comparison of pressure drop between ideal and randomized structures at 10 PPI 90% porosity.

Figure 4.10, shows the comparison of velocity vector contours between ideal and randomized structures with same porosity 90% and pore density (10 PPI) at $Re=750$. As expected, due to randomization the flow velocity attained higher velocity at narrow passages and preferential flow takes place in large passages. Similarly, in Figure

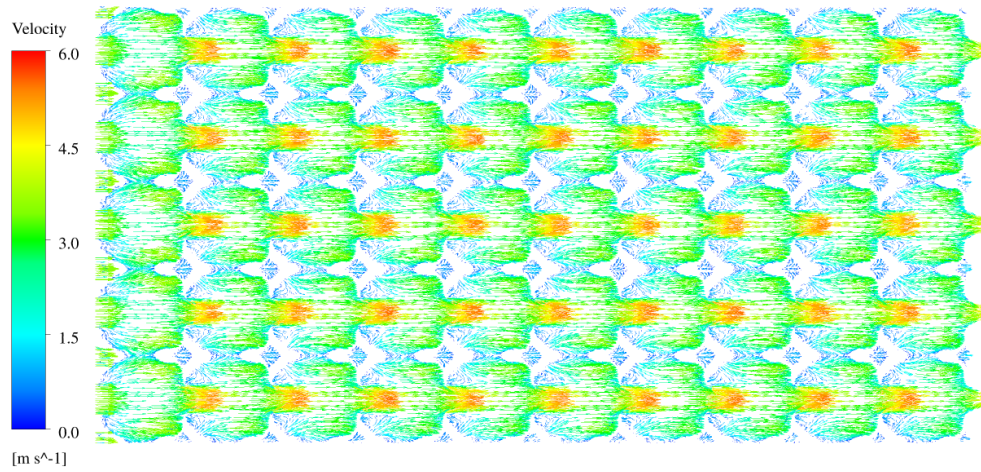
4.11 the pressure contours are plotted and compared between ideal and randomized structures. In Figure 4.11b, higher pressure drop caused due to randomizing the strut geometry and stagnation areas are seen in front of the open-cell foam struts. Figure 4.12, shows that streamlines for the random structure and are wriggling in nature and for the ideal structure, they are smooth in nature. It shows that there are high-velocity fluctuations in the case of the random structure whereas flow is smooth in the ideal structure, which concludes that higher pressure drops for the randomized structure is inevitable.

4.4.2 Determination of permeability, drag coefficient and Ergun constants for ideal Kelvin structure.

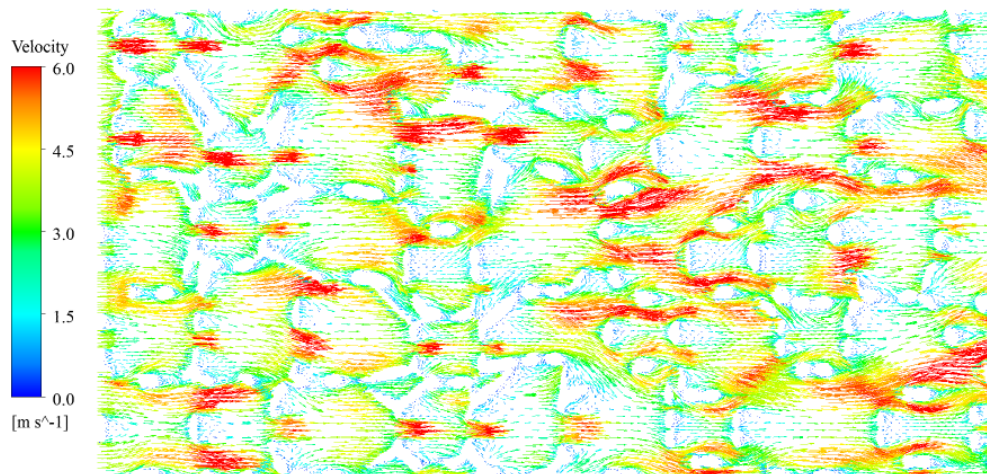
The permeability (K) and drag coefficients (C_F) are determined by comparing coefficients in Eq. (4.6) and Eq. (4.2). One obtains $\zeta = \varepsilon^3/S_v^2K$ and $\eta = \varepsilon^3C_F/S_vK^{0.5}$. While comparing Eq. (4.5) and Eq. (4.6), it was noticed that $A = 16\zeta$ and $B = 4\eta$. Thus, the constants A and B are calculated by fitting the DPLS Hagen number results into Hagen number correlation Eq. (4.5), through minimizing the RMSD (Root mean square deviation).

$$RMSD = 10^{RMSD(ELOG)} - 1; ELOG = \log(Hg_{calc}) - \log(Hg_{sim}) \quad (4.9)$$

Where, Hg_{sim} represents simulated Hagen number with simulated pressure drop results i.e., $Hg_{sim} = (dp/dx)(d_h^3/\rho\nu^2)$ and Hg_{calc} represents calculated values using correlation Eq. (4.5). The values of A & B are found to be 130.29 & 0.99, respectively for the least RMSD of 9.22%. Therefore, the values of $\zeta = 8.14$ and $\eta = 0.24$ are calculated by using A & B constants. However, these values are independent of the geometrical properties (porosity, PPI and specific surface area) of the porous structures, which is the basis behind the possibility of generating a correlation for calculating pressure drop in

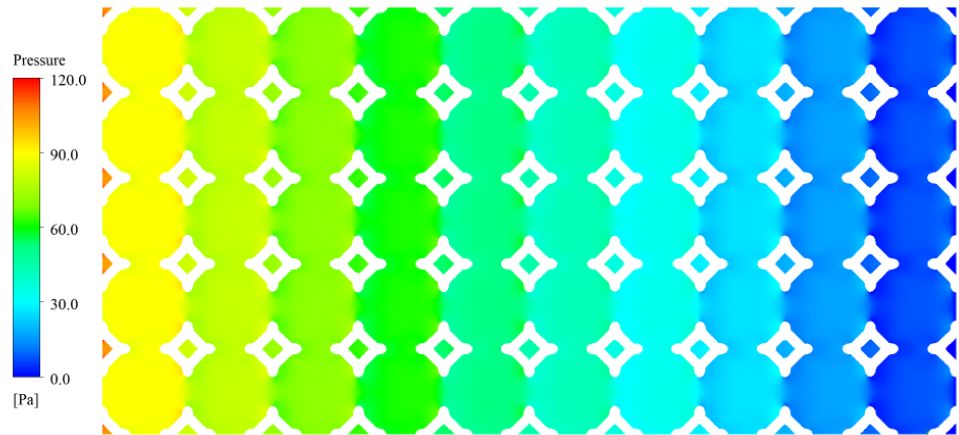


(a)

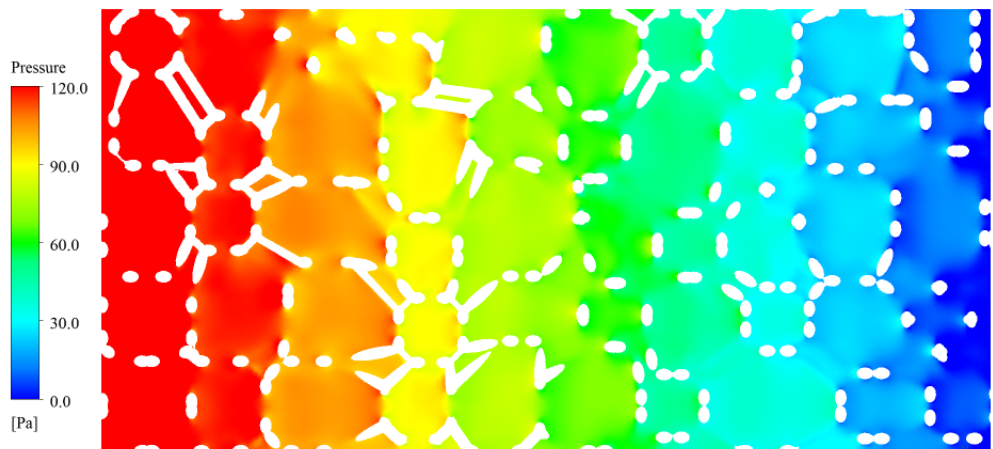


(b)

Figure 4.10: a) Ideal Kelvin structure (b) Randomized Kelvin structure [70-65-40] velocity vector contour plots on a 2-D cut plane with same porosity 90%, pore density 10 PPI and $Re = 750$.

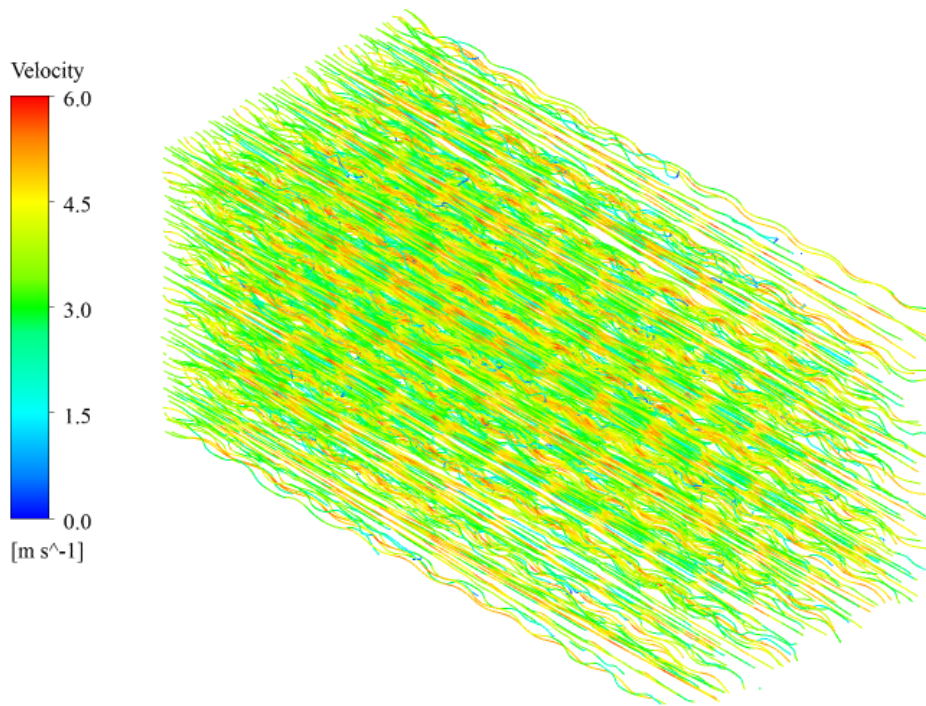


(a)

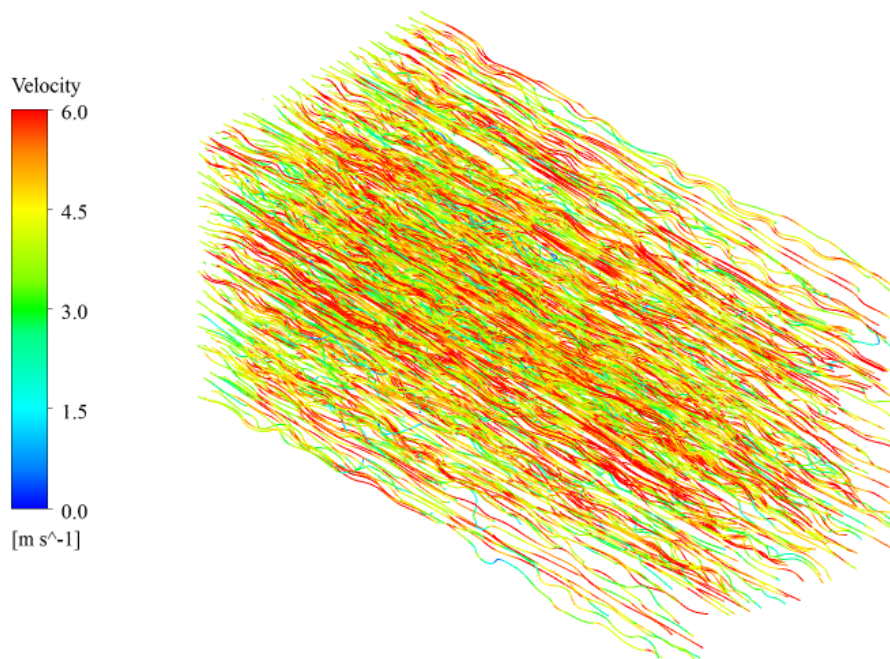


(b)

Figure 4.11: a) Ideal Kelvin structure (b) Randomized Kelvin structure [70-65-40] pressure contour plots on a 2-D cut plane with same porosity 90%, pore density 10 PPI and $Re = 750$.



(a)



(b)

Figure 4.12: Streamlines: (a) Ideal Kelvin structure (b) Randomized Kelvin structure [70-65-40] with same porosity 90%, pore density 10 PPI and $Re=750$.

Table 4.1: Pore densities, porosities, specific surface area, permeability and drag coefficient of ideal structures.

Pore density (PPI)	Nominal open porosity(%)	Specific surface area [m⁻¹]	Permeability K (m²)	Drag constant c_F (-)
10 PPI	80	1369	3.36×10^{-8}	0.1212
	85	1257	4.67×10^{-8}	0.112
	90	1069	7.74×10^{-8}	0.102
20 PPI	80	2722	8.33×10^{-9}	0.122
	85	2470	1.21×10^{-8}	0.112
	90	2123	1.97×10^{-8}	0.102
30 PPI	80	4110	3.68×10^{-9}	0.122
	85	3774	5.25×10^{-9}	0.111
	90	3192	8.69×10^{-9}	0.102

porous media. The pressure drop Eq. (4.5) can be re-written as follows

$$\frac{dp}{dx} = 130.29 \cdot \frac{\mu}{\varepsilon d_h^2} u_s + 0.99 \cdot \frac{\rho}{\varepsilon^2 d_h} u_s^2; Hg = 130.29 \cdot Re + 0.99 \cdot Re^2 \quad (4.10)$$

From the values of ζ and η , the permeability (K) and drag coefficients (C_F) are calculated. As expected, it can be observed that the permeability increases with increasing porosity and drag effect decreases with increasing porosity (Ref. Table 4.1).

4.4.3 Comparison of present simulation results with correlation provided in the present work.

Figure 4.13 shows the DPLS results of dimensionless pressure drop (Hagen number) versus Reynolds number of the ideal Kelvin structure of various PPI and porosities with Eq. (4.10). It is observed that all data (irrespective of PPI and porosity) fall on a single line. The RMSD between the present correlation Eq. (4.10) ($A=130.29$ & $B=0.99$) and the DPLS results is 9.22%. It clearly shows that the correlation (Eq. 4.10) developed in this work is matching with the DPLS results. Even if the structures are randomized as

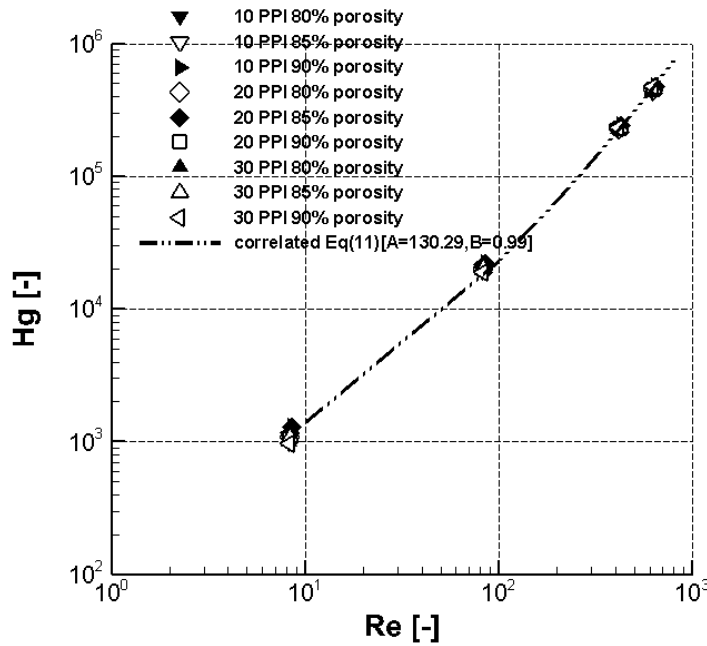


Figure 4.13: Hagen number versus Reynolds number of ideal Kelvin structures compared with present correlation (Eq. 4.10) at different porosities and pore densities.

shown in Figure 4.14 (irrespective of randomization, scale factor, and centroid factor), the Hagen number relation follow as single line tracking Eq. (4.10) and have a RMSD of 10.46%. In Figure 4.13, the ideal structures's DPLS results of 10, 20 & 30 PPI are exactly following Hagen number relation with no detectable deviation. So, in the randomization case, the simulations are performed only for 10 PPI to study the effect of randomization.

Figure 4.15 shows the relation between DPLS and correlated pressure drop results of ideal Kelvin structures having constant porosity 80% with different pore densities (10, 20 and 30 PPI). It is seen that the calculated pressure drop values with Eq. (4.10) matches well with the DPLS pressure drop results. Figures 4.16 shows that even if the structures are randomized with different scale and centroid factors, the correlation Eq. (4.10) matches well with the DPLS results.

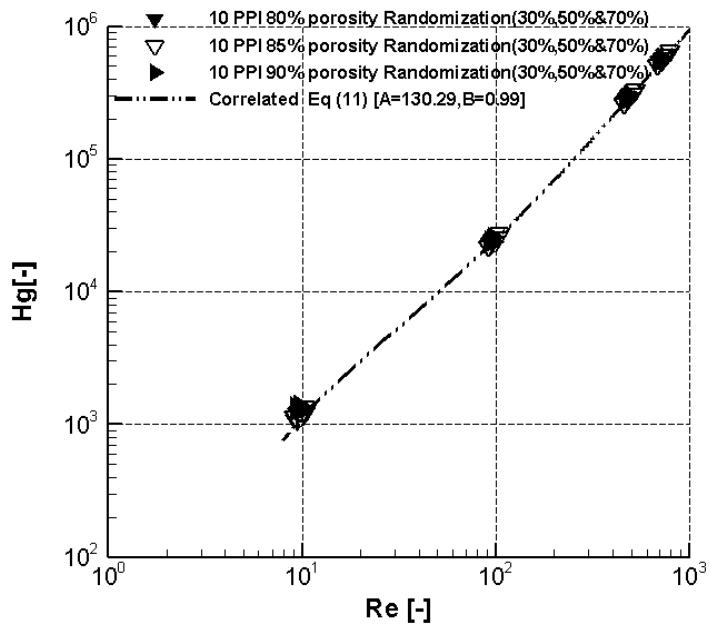


Figure 4.14: Hagen number versus Reynolds number for randomized Kelvin structures compared with present correlation (Eq. 4.10) at different porosities and pore densities (scale factor:65%, centroid factor:40%).

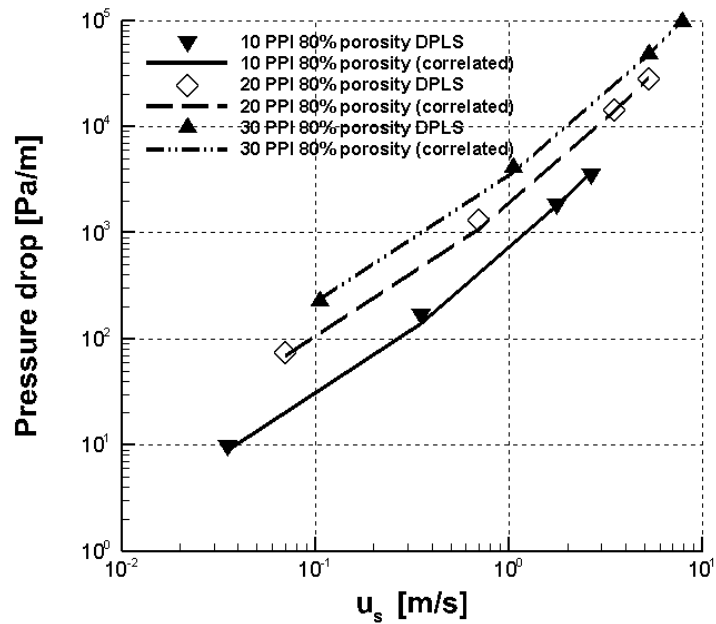


Figure 4.15: Comparison of pressure drop results between DPLS and Eq. (4.10) at 80% porosity of different ideal Kelvin structures.

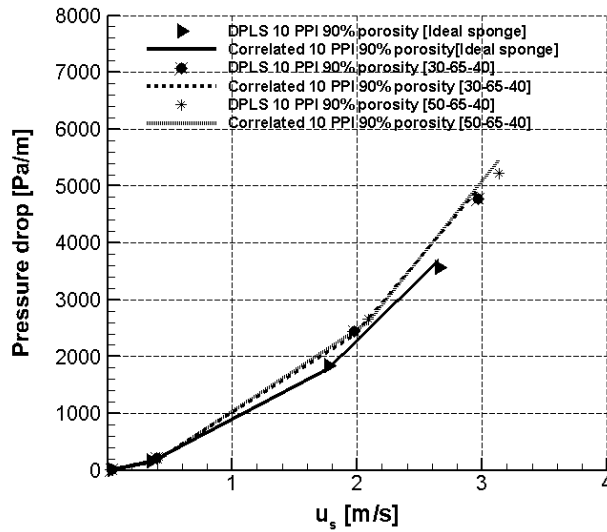


Figure 4.16: Comparison of pressure drop results between DPLS and Eq. (4.10) at 10 PPI 90% porosity of ideal & randomized structures.

4.4.4 Comparison of present correlation with DPLS results of real structures.

Figure 4.17 shows a comparison of pressure drop between present correlation (Eq. 4.10) versus real open-cell foams DPLS results of Parthasarathy *et al.* (2016). From Figure 4.17 it is noticed that around 91% of the pressure drop values of the present correlation (Eq. 4.10) in comparison to the DPLS results of real structures lie within a relative error of 7%. The investigation is done for Reynolds number within the range of 10 to 1000 and 10, 20 & 30 PPI at 80% and 85% porosities (Parthasarathy *et al.* 2016).

Using the constants ($A=129.6$ and $B=1.24$) provided by Parthasarathy *et al.* (2016) in Eq. (4.10) and comparing it with their own simulation results provided RMSD value of 17.64%. Using the same foam properties, DPLS results and comparing it with the constants ($A=130.29$ and $B=0.99$) in Eq. (4.10) reduced the RMSD to 5.7%. This is considerably less than the RMSD of 17.64%. Figure 4.18 shows that all DPLS results of Parthasarathy *et al.* (2016) follow the trend of the present correlation. This indicates that the correlation developed in this study fits well with DPLS results of the real structures.

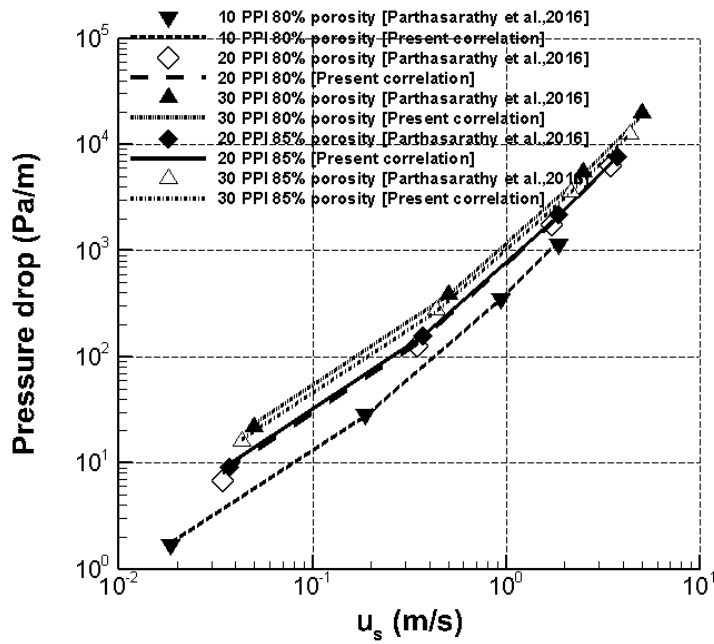


Figure 4.17: Comparison of pressure drop values calculated using Eq. (4.10) with DPLS results of real structures (10, 20 & 30 PPI Al_2O_3 open-cell foams at 80% porosity).

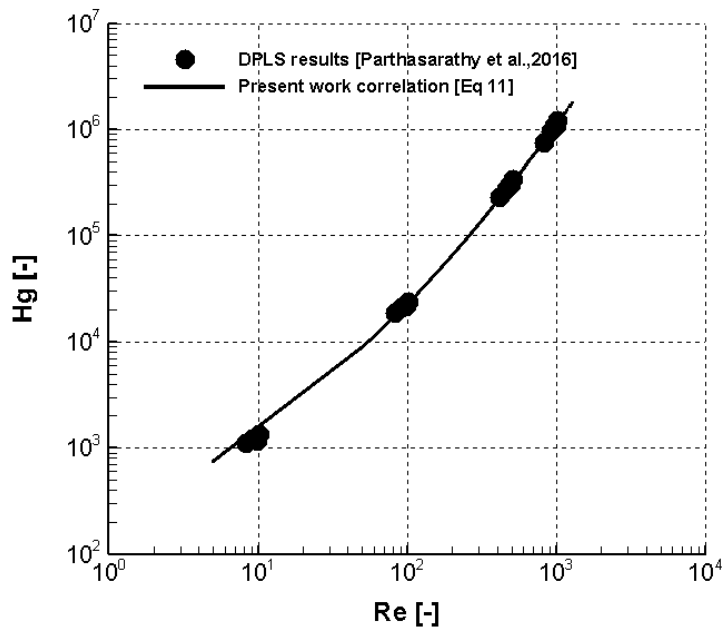


Figure 4.18: Hagen number versus Reynolds number (DPLS results of real structure vs present correlation).

4.4.5 Comparison of present correlation with experimental results of real structures.

Figure 4.19 & Figure 4.20 (ceramic open-cell foams) show a comparison of pressure drop between values calculated using Eq. (4.10) and that of experiments by Dietrich *et al.* (2009) and Inayat *et al.* (2011a). It can be observed that there is a good agreement between experimental pressure drop results with correlation provide in this study. From Figure 4.19, it is noticed that around 76% of pressure drop values from Eq. (4.10) lie within a relative error of 13%. Similarly from Figure 4.20, around 81% of pressure drop values lie within a relative error of 12%.

Figure 4.21 & Figure 4.22 (for metal open-cell foams) show a comparison of pressure drop between Eq. (4.10) and experimental results of Du Plessis *et al.* (1994) with water and glycerol as working fluid in high porosity metallic open-cell foams. It is seen that even for high porosities and pore densities, the developed correlation Eq. (4.10) successfully predicts the pressure drop in open cell foams. From Figure 4.21, it is noticed that nearly 88% of pressure drop values lie within a relative error of 12%. Similarly from Figure 4.22, around 75% of pressure drop values lie within a relative error of 15%. Thus it could be concluded that, the pressure drop in open-cell foams (ceramic or metallic) can be predicted to a very satisfactory level with Eq. (4.10). In most cases, the predicted values have a mean relative error value less than 15%.

Incera Garrido *et al.* (2008), Dietrich *et al.* (2009), Mancin *et al.* (2010), Inayat *et al.* (2011a), and Dukhan (2006) used air as a working fluid and Moreira *et al.* (2004a) used water as a working fluid. Du Plessis *et al.* (1994) conducted experiments by using both water and glycerol as a working fluid. The correlation provided in this study Eq. (4.10) is used to calculate pressure drop values with geometrical parameters provided by authors (Ref. Table 4.2) and are compared with the respective experimental results are shown in Figure 4.23. It is observed that irrespective of working fluid all experimental data followed Eq. (4.10).

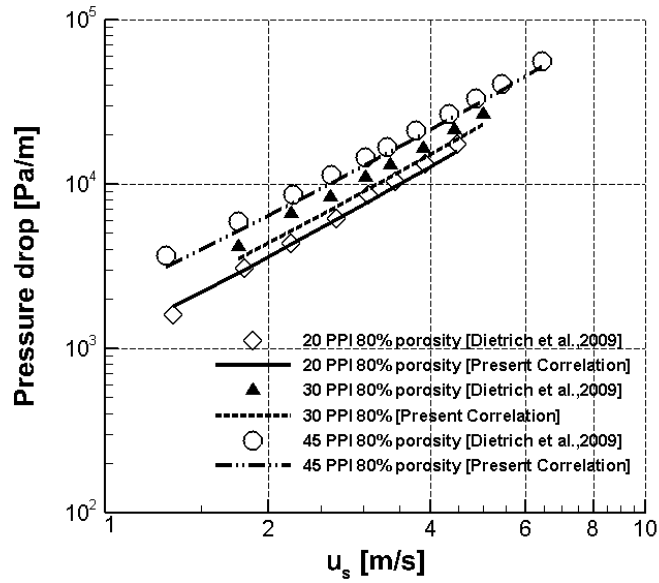


Figure 4.19: Comparison of pressure drop values calculated using Eq. (4.10) with experimental results of real structures (20, 30 & 45 PPI Alumina ceramic open-cell foams with total porosities 80.8, 80.6 and 80.8%, respectively).

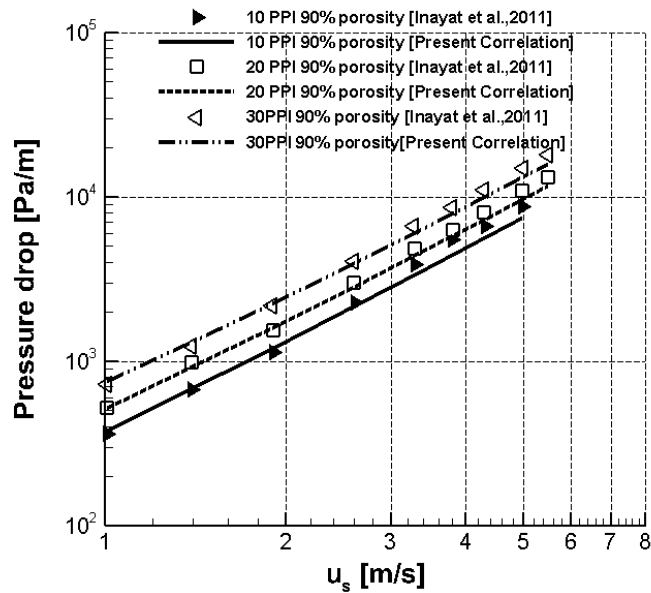


Figure 4.20: Comparison of pressure drop values calculated using Eq. (4.10) with experimental results of real structures (10, 20 & 30 PPI SSiC ceramic open-cell foams with total porosities 87.8, 89.6 and 88.5%, respectively).

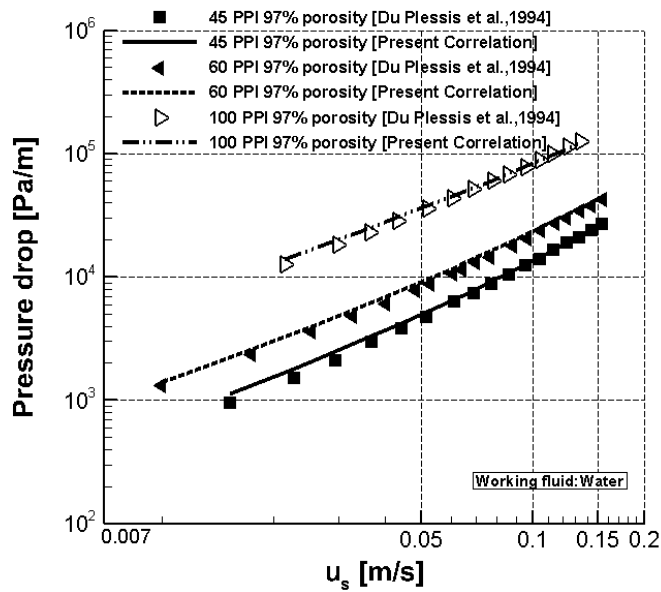


Figure 4.21: Comparison of pressure drop values calculated using Eq. (4.10) with experimental results of real pore structures (45, 60 & 100 PPI Ni metallic open-cell foams with total porosities 97.8, 97.5 and 97.3%, respectively).

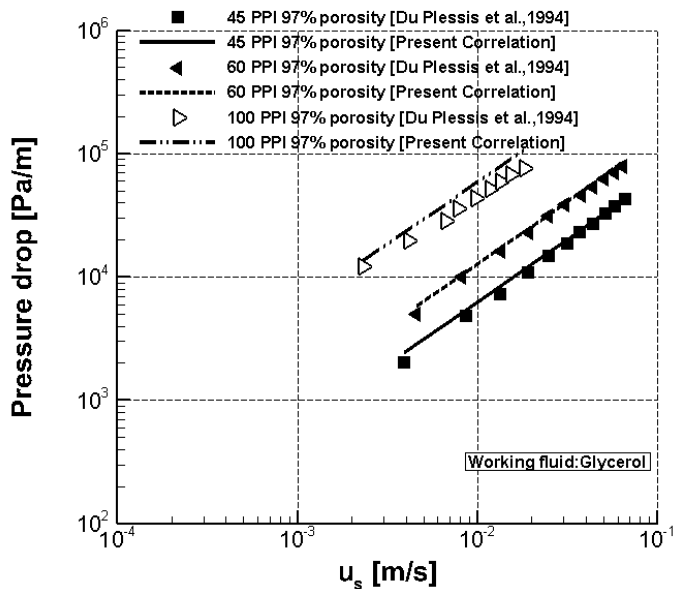


Figure 4.22: Comparison of pressure drop values calculated using Eq. (4.10) with experimental results of real pore structures (45, 60 & 100 PPI Ni metallic open-cell foams with total porosities 97.8, 97.5 and 97.3%, respectively).

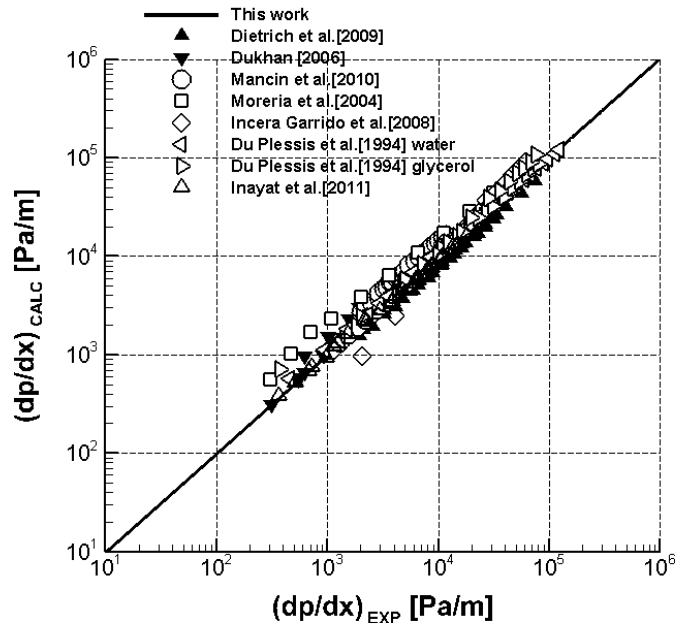


Figure 4.23: Comparison of experimental pressure drop results with calculated pressure drop using Eq. (4.10).

The general correlation (Eq. 4.5) developed by Dietrich *et al.* (2009) with constants, $A = 110$ and $B = 1.45$ in comparison with the results shown in Figure 4.19 have a RMSD of 21%. While the Eq. (4.10) in comparison to the same experimental data provides an RMSD of 12.79%, which is considerably less than 21%. Similarly, the RMSD error was checked for other experimental results of other authors (Ref. Table 4.2), it is noticed that the RMSD values lie within the $\pm 40\%$. But with the results of Moreira *et al.* (2004a) the RMSD is around 61%. The reason might be due to the deviation in the geometrical data provided by the author in comparison with other authors, it is noticed that for the same PPI, the specific surface area was approximately two times high (Ref. Table 4.2). For this reason the results of Moreira *et al.* (2004a) are not considered for further comparison. As reported by Dietrich (2012), the high specific surface area is usually caused by the anisotropy of structure as well as due to the presence of closed pores and it also depends on manufacturing processes. In this study, it can be identified, even with a minor change in the specific surface area there is a greater change in pressure drop. Which shows that the measurement of the geometrical

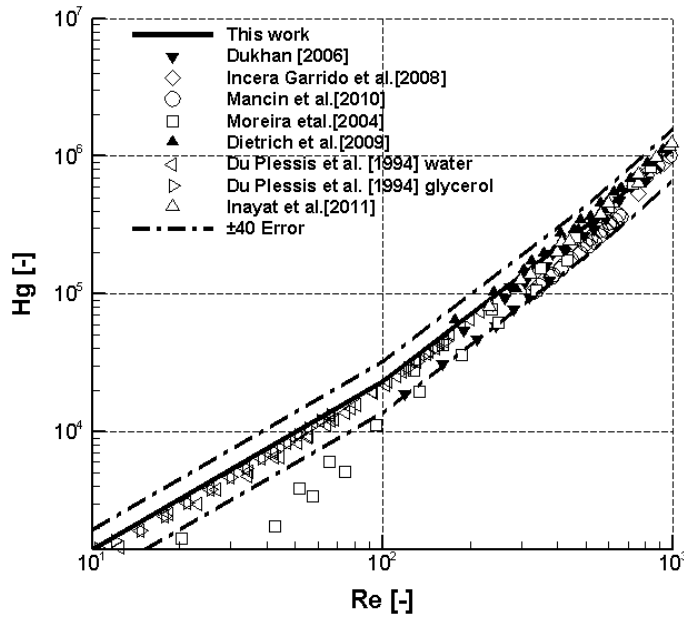


Figure 4.24: Hagen number versus Reynolds number between experimental results of real porous structures and present study correlation.

properties is very important and they should be as precise as possible.

Furthermore, for validation of the current model, the non-dimensional form of Hagen number versus Reynolds data was plotted in Figure 4.24. The graph plotted to compares experimental results available in the literature with the correlation (Eq. 4.10). It can be viewed that all experimental values follows the Eq. (4.10) within a RMSD of $\pm 40\%$ over a wide range of Reynolds numbers. It seems there is a good consistency between the present correlation against experimental results. Thus, it is concluded that the correlation developed for the reticulated Kelvin structure (ideal) is also suitable for real porous structure (non-ideal) within a range of $10^{-1} < Re < 1000$ at higher porosities ($>75\%$).

Table 4.2: Comparison of RMSD values between the correlated Hagen number and experimental investigations (few of the authoress's specific surface area values collected from Dietrich 2012).

Author Reference	Foam material	Fluid	PPI	Total porosity	S_v [m^{-1}]	Re	RMSD
Parthasarathy <i>et al.</i> (2016) (DPLS results)	Al_2O_3	Air	10	0.82	577.5	10-1000	5.70%
			20	0.82	900.9		
			30	0.845	996.3		
			30	0.822	1264.9		
Dietrich <i>et al.</i> (2009)	Alumina	Air	20	0.808	1204	100-1000	12.79%
			30	0.806	1402		
			45	0.809	1884		
Inayat <i>et al.</i> (2011a)	SSiC	Air	10	0.878	651	400-1500	10.30%
			20	0.896	876		
			30	0.885	1122		
Du Plessis <i>et al.</i> (1994)	Ni	Water	45	0.978	2750	10-240	8.96%
			60	0.975	3925		
			100	0.973	8451		
		Glycerol	45	0.978	2750	0.2-12	22.01%
			60	0.975	3925		
			100	0.973	8451		
Dukhan (2006)	Alumina	Air	10	0.919	790	100-1000	29.65%
			20	0.924	1200		
			40	0.923	1800		
Mancin <i>et al.</i> (2010)	Alumina	Air	10	0.934	736	100-1000	35.82%
			20	0.932	1169		
			40	0.93	1721		
Moreira <i>et al.</i> (2004a)	Al_2O_3	Water	8	0.94	1098	10-1000	61.20%
			20	0.88	2150		
Incera Garrido <i>et al.</i> (2008)	$\alpha-Al_2O_3$	Air	20	0.777	1290	100-1000	39.12%

4.5 Conclusion

In this chapter, the numerical study of pressure drop within the reticulated ideal & randomized Kelvin structures were investigated. The 3D open-cell foam geometries for the analysis were constructed using an in-house code along with the use of visualization tool kit (VTK) libraries. In this study, ideal and randomized Kelvin structures geometries with different porosities (80%, 85%, and 90%) and pore densities (10, 20, and 30 PPI) were generated. The grid geometries had been used to perform direct pore level simulations (DPLS) with the aid of commercial CFD software (ANSYS CFX). For each of the structures, the simulations were performed for four different Reynolds numbers, i.e., Re 10, 100, 500, and 750. From the results of numerical simulations, a parametric study was conducted to verify the influence of geometrical parameters on pressure drop. Based on the parametric study, some of the observations were noted as follows.

1. The pressure drop increased with increasing pore density and velocity. This pore density effect is mainly due to an increase in the specific surface area with respect to pore density, i.e., higher pore density results in a denser packing of struts.

2. The increase in porosity leads to decrease the pressure drop for a given pore density. This effect was primarily due to the reduction in strut diameter, which caused a decrease in specific surface area when porosity increased. A similar effect of porosity was noted even in the randomized Kelvin structure.

3. Based on simulation results, a pressure drop correlation was proposed similar to that of the Ergun-type equation. The permeability and drag coefficient values were determined from the values of new viscous and inertial coefficients. As expected, for high porosity, the permeability increased and the drag effect decreased, respectively.

4. Furthermore, the proposed correlation was validated by comparing it with several experimental results of literature data, and it showed that all experimental values follow the Eq. (4.10) within a RMSD of $\pm 40\%$ over a wide range of Reynolds numbers.

5. Finally, it was concluded that the correlation was able to predict the pressure drop in open-cell foams within a range of $10^{-1} < \text{Re} < 1000$ at higher porosities ($>75\%$).

4.6 Closure

The methodology adopted for calculating the pressure drop in open-cell foams was explained in detail in this chapter. From the simulation results, A new pressure drop correlation was proposed and validated with available experimental results. Further, with the same structures, dispersion simulations are presented in the following chapter.

CHAPTER 5

LONGITUDINAL DISPERSION IN RETICULATED KELVIN STRUCTURE

5.1 Introduction

In a porous medium, dispersion theory describes the qualitative and quantitative behavior of miscible fluids displacing one another. When a miscible fluid displaces another, it tends to mix with the displaced fluid; as a result, the mixing zone expands as the displacement process moves along (Ref. Figure 5.1b). This mixing and spreading of the injected fluid is referred to as "hydrodynamic dispersion". The terms dispersion and diffusion are related concepts. However, dispersion occurs at a macroscopic level when fluid flow facilitates the mixing of the tracer molecules with the fluid molecules. But diffusion occurs at the molecular level and it happens when the tracer molecules move randomly across the fluid due to the existence of a tracer concentration gradient.

As an illustration, imagine a porous material enclosed in a cylindrical tube and saturated with clean water. A chemical liquid compound combined with water is fed into the tube at time zero with a concentration of Y_0 . The injection rate is maintained constant, the fluid direction is linear, and no physico-chemical interaction is presumed between the fluids and the solid. At time zero, the profile of concentration is a step function zero (see Figure 5.1a). While increasing time, the concentration of injected fluid varies; as a result, the mixing zone develops and expands as the displacement process moves along, and its concentration profile typically resembles an S-curve see in Figure 5.1. It is a classic dispersion effect, and its quantification gives rise to different dispersion equations.

In the past studies, several researchers investigated the dispersion employing packed

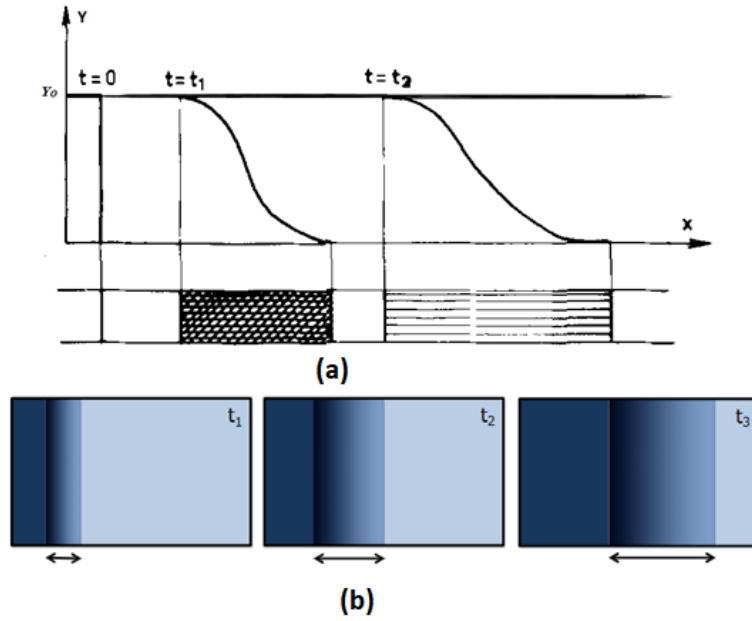


Figure 5.1: (a) Evolution of the transition zone with time (adopted from Fried 1975) (b) mixing and spreading of tracer concentration

bed type porous media. From that, Taylor (1953) quantified the dispersion theory at first and concluded that the spreading of tracer fluid could be characterised with the aid of an ‘apparent diffusion coefficient’. Later Aris and A (1956) added the molecular diffusion effect to Taylor’s expression for ‘dispersion coefficients’. In general, the relation between molecular diffusion and hydrodynamic dispersion of spreading the tracer is defined by the Peclet number, $Pe_m = ud/D_m$, where ‘u’ represents the pore velocity, ‘d’ is the characteristic length of the porous domain and D_m denotes the molecular diffusion coefficient. A higher Peclet number indicates greater hydrodynamic dispersion. Carbonell and Whitaker (1983) presented an advection-dispersion equation by volume averaging in porous media

$$\phi \frac{\partial Y}{\partial t} + \nabla \cdot (\phi u Y) = \nabla \cdot (\phi D \cdot \nabla Y) \quad (5.1)$$

Where ‘Y’ denotes the concentration of tracer, ϕ stands for volume fraction of fluid, and ‘D’ represents the hydrodynamic dispersion tensor. According to Boon *et al.*

(2000), hydrodynamic dispersion is similar to the process of turbulent diffusion, in which porous struts acts as eddies to spread the flow. Delgado (2006) reviewed the dispersion in porous media by analysing the data from several investigations that are available in the literature. In detail, the author discussed the effect of various fluid properties and geometries on the dispersion behavior of porous media. Further, Delgado (2007) proposed an empirical correlation to calculate axial and transverse dispersion coefficients for liquid and gaseous flow. Instead of using the typical representation of the ratio D_L/D_M as a function of Pe_m , the author used to define the macroscopic Peclet number in the axial direction $Pe_L = ud/D_L$ as a function of Pe_m . For gaseous flow, at high $Pe_m (>60)$, a constant value of $Pe_L = 2$ can indicate the data for beds with spherical elements in good agreement.

5.2 Dispersion in RPS

Its well known, RPS are attractive materials defined by higher porosity, lightweight, excellent mixing capabilities and provide minimal pressure drop in contrast to conventional packing materials (packed beds/monoliths). It consists of disordered and interconnected solid phases with continuous void/fluid space. Consequently, it provides a tortuous flow path and leads to augmental mixing and heat/mass transfer. Because of these good mixing properties, these are essential materials for natural and industrial processes such as groundwater treatment, pollutant filters, secondary oil recovery, vaporizers and heat-exchangers (Maier *et al.* 2002). In addition, they have been employed as catalyst supports in fixed-bed reactors because of their large specific surface area (Giani *et al.* 2005; Lucci *et al.* 2014). In light of the above applications, it is essential to analyse dispersion in porous media. This study intends to characterise the longitudinal dispersion coefficient (LDC) in ideal and randomized Kelvin structures using DPLS.

5.3 Problem statement

In the literature, plenty of data exists for the dispersion coefficient in packed beds, where porosity is possible at lower than 45% and noticed very rare data available for high porosity(>90%). In general, high porosity exist in real porous structures like open-cell metallic/ceramic commercial foams, and suppliers do not usually provide such information about dispersion. This is because the dispersion is mainly influenced by the internal structure of the porous geometry, and it is unable to be defined without considering structural parameters. Thus, this research aims to calculate the effective longitudinal dispersion coefficients in highly porous reticulated open-cell foam structures. In this chapter, parametric CFD studies are performed on Kelvin cell structures, and are used to understand the influence of geometrical parameters on dispersion. For that, DPLS is performed for the same structures that are used in pressure drop study of porosities (80%, 85%, and 90%) and PPI (10, 20, and 30 PPI) through CFD-FVM method. Based on the parametric study, a modified characteristic length correlation is developed to evaluate the longitudinal Peclet number(Pe_L), and it was validated with numerical & experimental data of packed beds and real porous foams that are published in the literature.

5.4 Numerical setup

In the numerical simulations, the working fluid is chosen as air and assuming that air is a Newtonian fluid with a fixed density ' ρ '. While considering the un-steady flow condition, the simulations are performed by solving mass and momentum equations:

$$\frac{\partial \rho}{\partial t} + \frac{\partial}{\partial x_j}(\rho u_j) = 0 \quad (5.2)$$

$$\frac{\partial}{\partial t}(\rho u_k) + \frac{\partial}{\partial x_j}(\rho u_j u_k) = -\frac{\partial p}{\partial x_k} + \frac{\partial}{\partial x_j} \left(\mu \frac{\partial u_k}{\partial x_j} \right) \quad (5.3)$$

where p is the pressure, μ denotes the viscosity of mixture, and u_j and x_j represent velocity and Cartesian coordinates in the j -direction, respectively. The boundary conditions are defined as constant velocity at the inlet and specified static pressure with zero gradient conditions at the outlet. The side surfaces are defined with periodic boundary conditions, and structure surfaces are defined as a wall with no-slip boundary conditions. In addition, flow conditions are considered to be laminar for the defined Reynolds numbers and no turbulence models have been discussed in this study.

In order to acquire computational grids, Kelvin cell geometries are imported into commercial meshing tool (ICEM CFD). The resulting grids have 12-37 million tetrahedral cells and 2-7 million grid points. One of the sample of final grid is shown in Figure 5.2. The flow calculations are solved using conventional CFD-finite volume discretization (using ANSYS-CFX solver) with a bounded linear approach, and convergence criteria have been set at 10^{-6} . In addition, to achieve a fully developed flow, the geometry length is maintained maximum of 15 pores in the of flow trajectory, respectively.

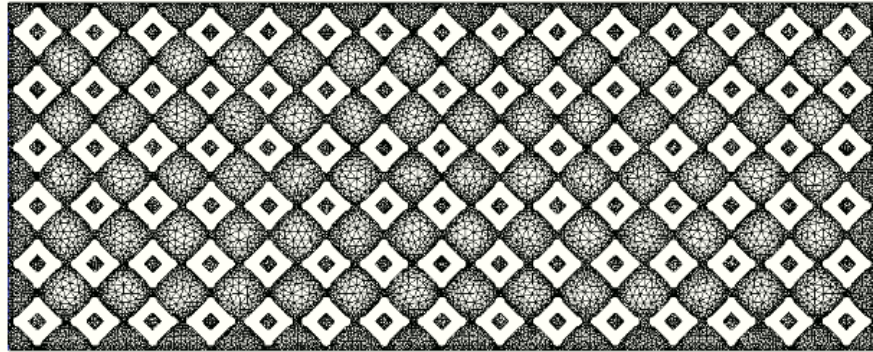


Figure 5.2: Final grid sample of 30 PPI 80% porosity.

5.4.1 Numerical procedure

In this work, steady-state simulations are performed initially for each structure with a stationary flow of air. Later, a transient computation is carried out by employing the converged stationary solution as the initial condition, where the entering fluid is abruptly switched from air to tracer air with air-like qualities and with $D_m = 1.3 \times$

$10^{-5}m^2/s$. Then the tracer air is transported through the porous structure by convection and diffusion.

In order to determine effective LDC, the 3-Dimensional mixture fields are reduced into 1-Dimensional ones by averaging mass flow over N cross-sectional planes.

$$\overline{Y(x_k, t)} = \frac{\sum_{i=1}^G (Y_i(t) \cdot \rho u_i A_i(x_k))}{\sum_{i=1}^G \rho u_i A_i(x_k)} \quad (5.4)$$

$\overline{Y(x_k, t)}$ indicates the mass flow avg. tracer concentration at the K^{th} plane at the location x_k and time t, $\rho u_i A_i(x_k)$ denotes the mass flow in the i^{th} grid cell of the plane, G denotes the no. of grid cells and $Y_i(t)$ represents the tracer concentration value in the i^{th} grid cell at time t. Through this procedure, the 1-Dimensional dispersion field in time can be determined from the the 3D simulations. Figure 5.3 depicts the locations of surfaces where the tracer mass fraction is constant $Y = 0.5$ at different flow times. The methodology used in this study is similar to that of Maier *et al.* (2002) & Parthasarathy *et al.* (2013), where tracer species mass fraction profiles are used to calculate the dispersion coefficients. In contrast to an identical approach employed in Hackert *et al.* (1996) and Pereira *et al.* (2005). In this study, the LDC was estimated through a abrupt jump in concentration at the entry of the flow domain. Further, the transient transport of concentration jump through advection and diffusion is analytically defined with the avg. flow velocity ($x' = x - u.t$) by Fick's law

$$\frac{\partial Y}{\partial t} = D \cdot \frac{\partial^2 Y}{\partial x'^2} \quad (5.5)$$

where D is the dispersion coefficient, and Y represents the tracer concentration, respectively. The analytical solution of the above equation is defined as

$$Y = 1 - erf\left(\frac{x'}{2\sqrt{D.t}}\right) \quad (5.6)$$

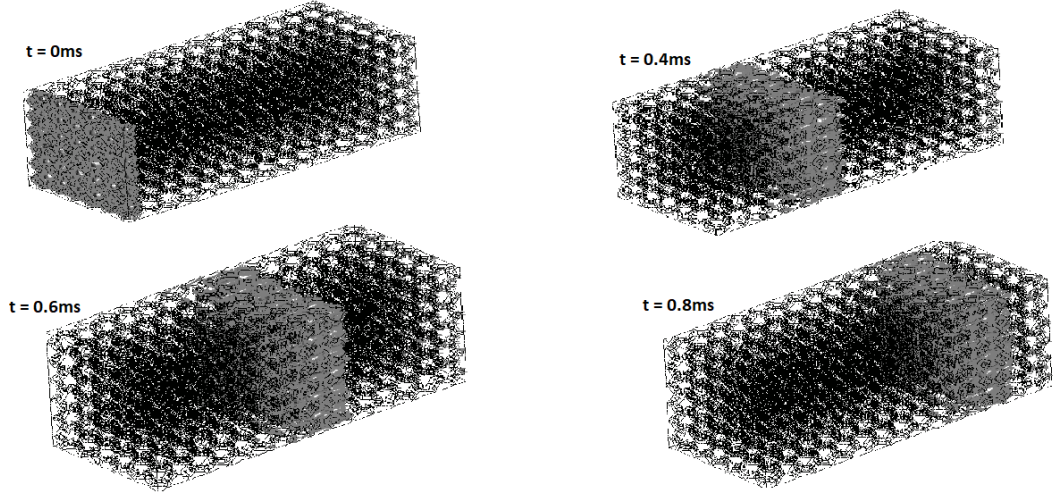


Figure 5.3: Constant tracer concentration at $Y = 0.5$ (light gray) pass on into a foam geometry (dark gray).

As an illustration, in Figure 5.4, the computed mass fraction profiles for the dispersion in both ideal and randomized Kelvin structures of 30 & 10 PPI 80% are shown at different time step intervals. Further, considering the gradient of concentration profiles ($\partial Y/\partial x$), it is easy to determine the effective LDC.

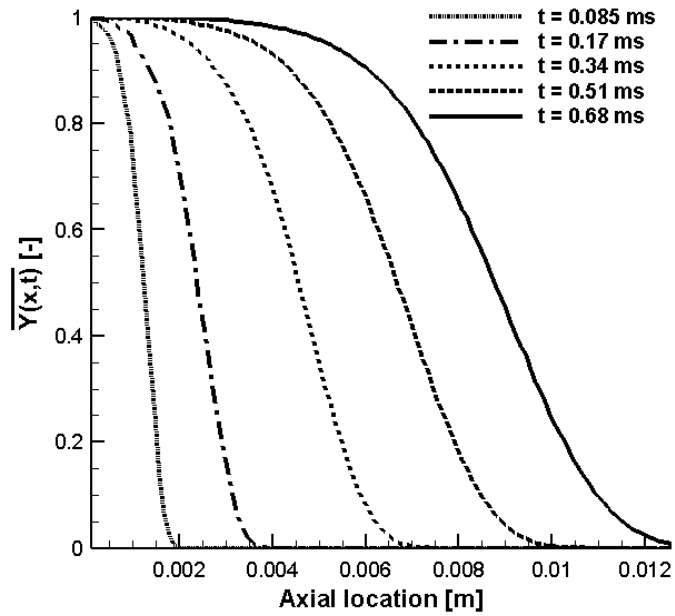
$$\frac{\partial Y}{\partial x} = -\frac{2}{2\sqrt{\pi D.t}} \exp\left(-\frac{x^2}{4tD}\right) \quad (5.7)$$

Here, the simulated gradient of concentration is assumed to be Gaussian type, and then the LDC is calculated by fitting one of the simulation results to a width of the analytical solution's gradient curve, which is approximated by a CDS

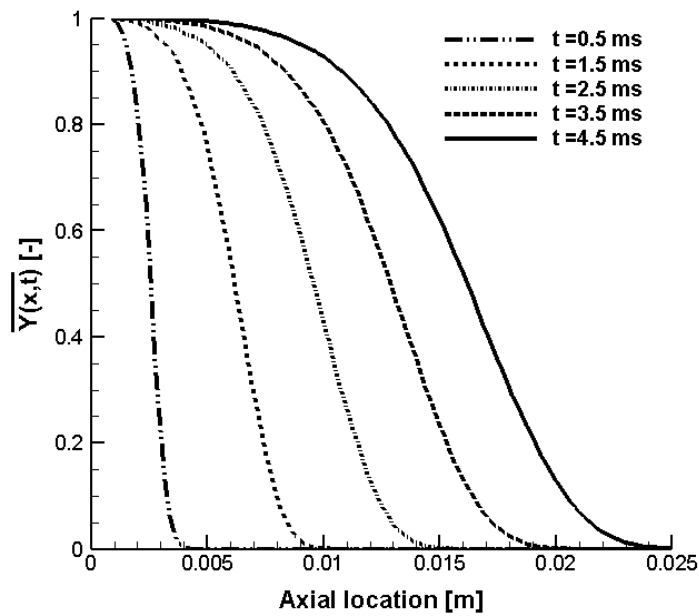
$$\frac{\partial Y(x, t)}{\partial x} = \frac{Y(x_{k+1}, t) - Y(x_{k-1}, t)}{(x_{k+1}) - (x_{k-1})} \quad (5.8)$$

In Figure 5.5, five selected instantaneous of the tracer mass concentration gradient profiles are shown for the dispersion in ideal and randomized Kelvin structures.

Further, to evaluate LDC, the analytic solution gradients are fitted to the simulated gradients by means of variance $\sigma^2 = 2tD_L$, i.e., the width of the Gaussian function

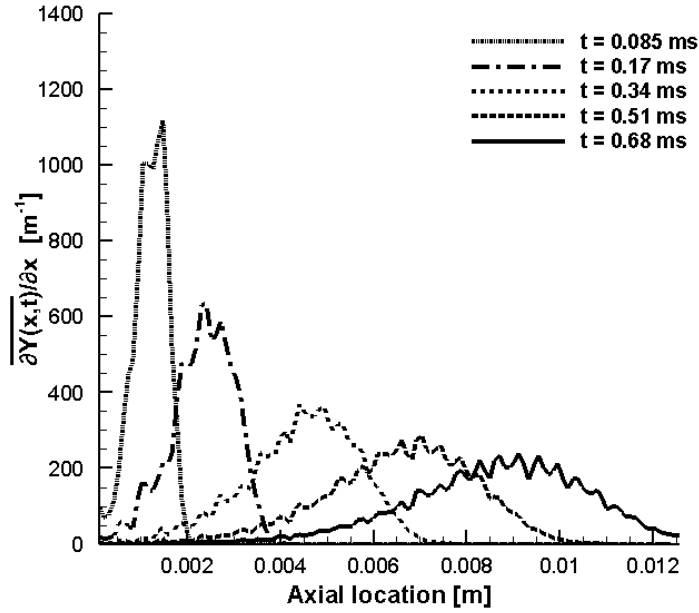


(a)

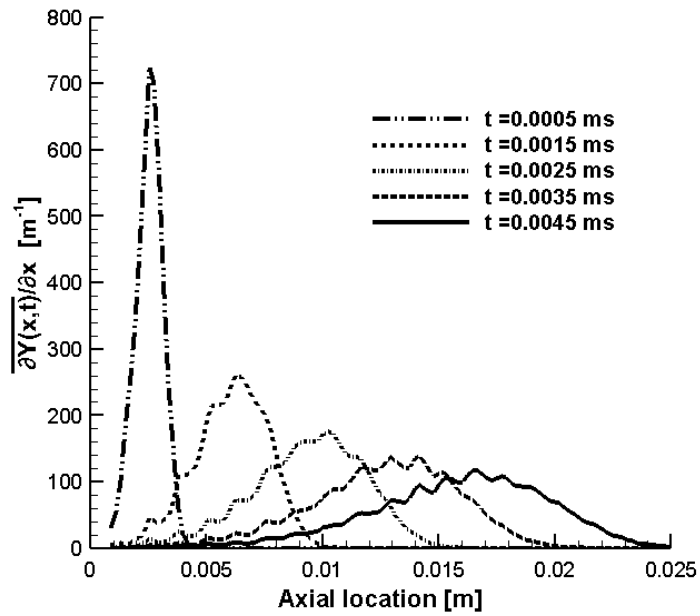


(b)

Figure 5.4: Instantaneous tracer concentration profiles at 5 time steps (a) Ideal structure of 30 PPI and 80% porosity (b) Randomized structure of 10 PPI and 80% porosity.



(a)



(b)

Figure 5.5: Instantaneous tracer concentration gradient profiles at 5 time steps (a) Ideal structure of 30 PPI and 80% porosity (b) Randomized structure of 10 PPI and 80% porosity.

Eq. (5.7) must be modified to account for the second Moment σ_{sim}^2 of the simulated gradient, then it leads to the results in

$$D_L(t) = \frac{\sigma_{sim}^2(t)}{2t} \quad (5.9)$$

Therefore, In order to calculate the time-dependent variances σ_{sim}^2 , It is necessary to assess the concentration gradient profiles' first and second moments.

$$\overline{x_{sim}(t)} = \sum_{k=1}^N \left(\frac{\overline{\partial Y(x_k, t)}}{\partial x} \cdot x_k(t) \cdot \frac{x_{k+1}(t) - x_{k-1}(t)}{2} \right) \quad (5.10)$$

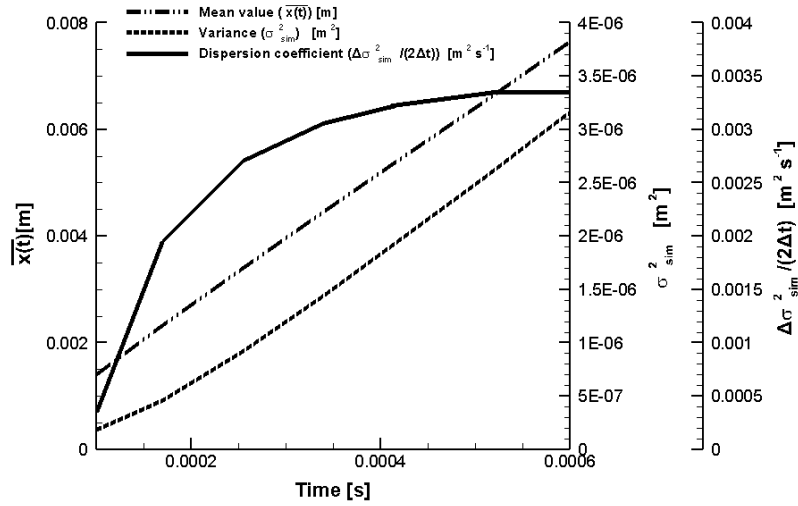
$$\sigma_{sim}^2(t) = \sum_{k=1}^N \left(\frac{\overline{\partial Y(x_k, t)}}{\partial x} \cdot (x_k(t) - \overline{x_{sim}(t)})^2 \cdot \frac{x_{k+1}(t) - x_{k-1}(t)}{2} \right) \quad (5.11)$$

As an example, Figure 5.6a and b show the first ($\overline{x_{sim}(t)}$) and second moments ($\sigma_{sim}^2(t)$) respectively for the ideal and randomized structures besides the resulting LDC $D_L(t)$ as a function of time. It is noticed that after a short interval of time (0.3 ms), both ideal and random structures reach an almost constant value.

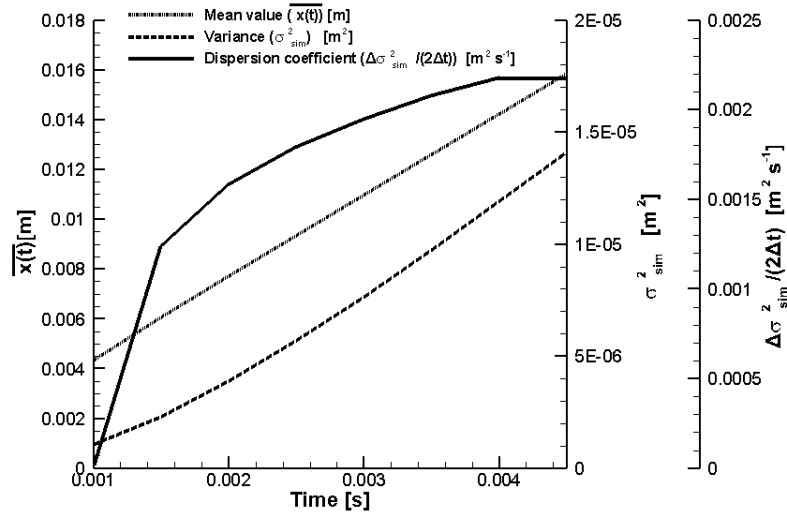
5.5 Results and discussions

5.5.1 Simulation results

In order to assess the longitudinal dispersion coefficient, in this study, high porosity reticulated structures of ideal and randomized Kelvin structures are used. The DPLS is carried out for various foam structures of various porosity, PPI and flow rates at Re of 10, 100, 500, and 750. Figure 5.7 (a-c) illustrates the effect of flow rate and porosity on the D_L/D_m ratio of ideal and randomized Kelvin structures. In general, it is observed that for the same PPI, the D_L/D_m ratio increases with decreasing porosity. Due to reduction in porosity; the pore-scale model shows greater velocity fluctuations, resulting in greater mixing in the pores. In addition, it is also noted that the LDC increases with increasing the fluid velocity. This is presumably due to mixing occurring



(a)



(b)

Figure 5.6: Dispersion coefficients and the time evolution of the mass fraction gradients (a) Ideal structure of 30 PPI and 80% porosity (b) Randomized structure of 10 PPI and 80% porosity.

more readily when fluid velocity increases due to more pore velocity variations. i.e., while increasing fluid velocity in porous media, the velocity fluctuations are high due to the high drag experienced by the carrier fluid from the cylindrical struts. When pore velocity is small, velocity variations within the pores are also small, and mixing takes place mainly due to the result of diffusion. A Similar kind of trend is observed in the literature (Parthasarathy *et al.* 2013; V. Chandra *et al.* 2019; Garmeh *et al.* 2009).

Similarly, Figure 5.8 plotted the effect of PPI on the longitudinal dispersion coefficient. It can be seen that for the same porosity, the LDC decreases while increasing pore density. It is mainly due to a reduction in pore diameter while increasing PPI. In the literature, Hutter *et al.* (2011) and Parthasarathy *et al.* (2013) reported the same kind of trend in real porous structures.

In order to investigate the randomization effect, a comparison is made between ideal Kelvin structures and randomized Kelvin structures, as shown in Figure 5.9. In contrast to ideal structures, the LDC increases in randomized structures even if maintaining the same PPI and porosity (maintained similar flow conditions and S_v for the both structures).

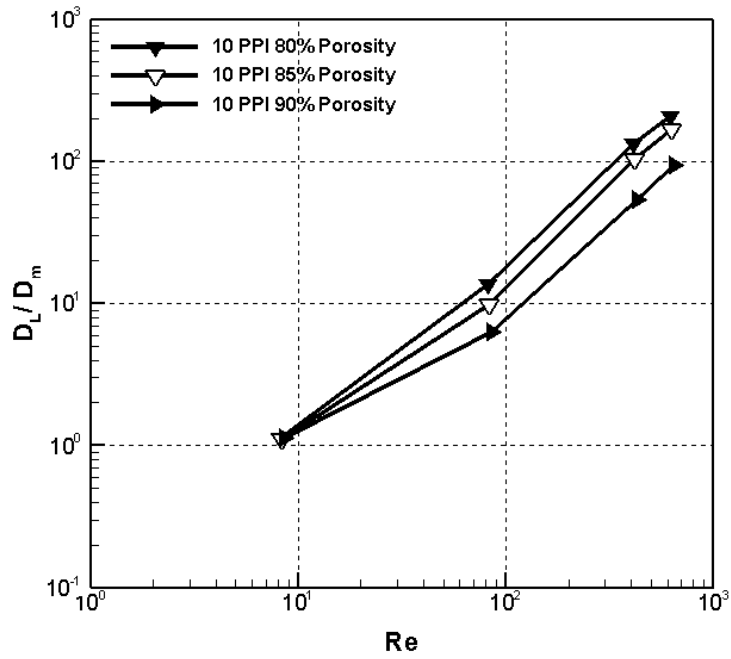
In packed beds, it was noted that the longitudinal dispersion primarily depends on the particle packing shape irrespective of the particle size. Therefore, this dependence on particle packing form in packed beds implies that there may be a substantial variation in the longitudinal dispersion between packed beds and open-cell foams. In Figure 5.10, the ratio of calculated D_L/D_m results versus the molecular Peclet number of present work is plotted and compared with data of packed beds and real porous structures. It can be seen that the D_L/D_m ratio of both ideal and randomized Kelvin structures follows a linearly increasing trend similar to that of packed beds, but small ratio values are noticed. Taylor (1953) and Prausnitz (1958) explained the reason that in porous media, when a fluid element comes into contact with a solid obstacle in its flow direction, it undergoes radial mixing as a result of lateral movement. To avoid that solid structure, the fluid is compelled to follow a long circuitous route. During the process, the fluid

element enters a region with different longitudinal velocities, causing longitudinal dispersion as a result of radial mixing as well as lateral velocity gradients. In the case of Kelvin structures, the strut diameter is very small (see Table 5.1) and allows less fluid to move laterally compared to a packed bed structure. Therefore, less longitudinal dispersion is found in the Kelvin structures.

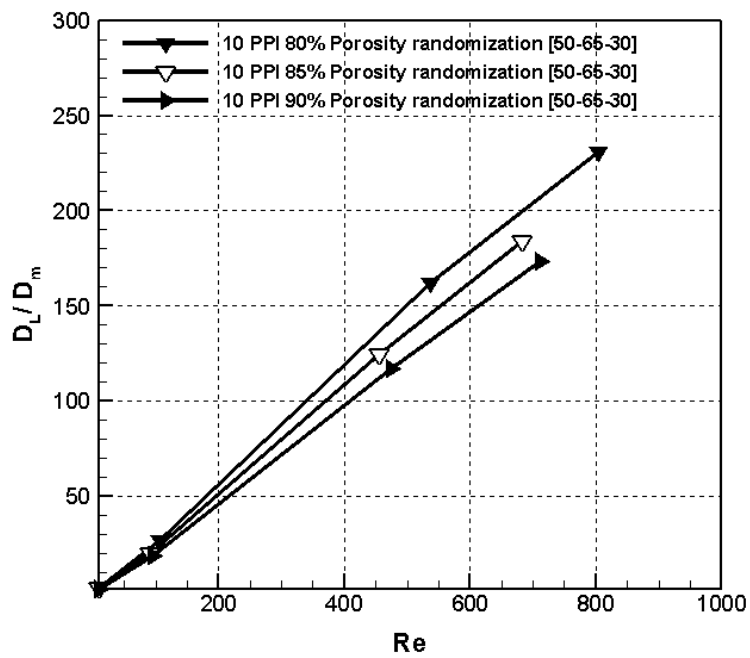
Figure 5.11 contains the plots of DPLS results where the longitudinal dispersion as a function of molecular Peclet number of different foam structures used in this study. Similar to packed bed structures, Kelvin structures have linearly increasing longitudinal dispersion values with increasing molecular Peclet numbers. In this study, strut diameter is used as a characteristic length to determine the Peclet number. The strut diameter and geometrical properties of of particular structures are shown in Table 5.1.

In a porous media, dispersion is caused by two main mechanisms: one is molecular diffusion, and the other one is mixing arising from channel flow. When Peclet numbers are low, the former will be more significant, and when Peclet numbers are high, the latter will be more important. But, in the intermediate zone, both mechanisms will contribute an important role. Most of the studies in packed beds reported that (Delgado 2006, Delgado 2007; Edwards 1968; Evans and Kenney 1966; Perkins and Johnston 1963; Hiby 1962) at low Pe number, the contribution of longitudinal mixing is diminished by virtue of the tortuous nature taken by fluid particles. Thus, the LDC (D_L) is dependent on molecular diffusivity (D_m) by Eq. (5.12). Where τ defines the tortuosity

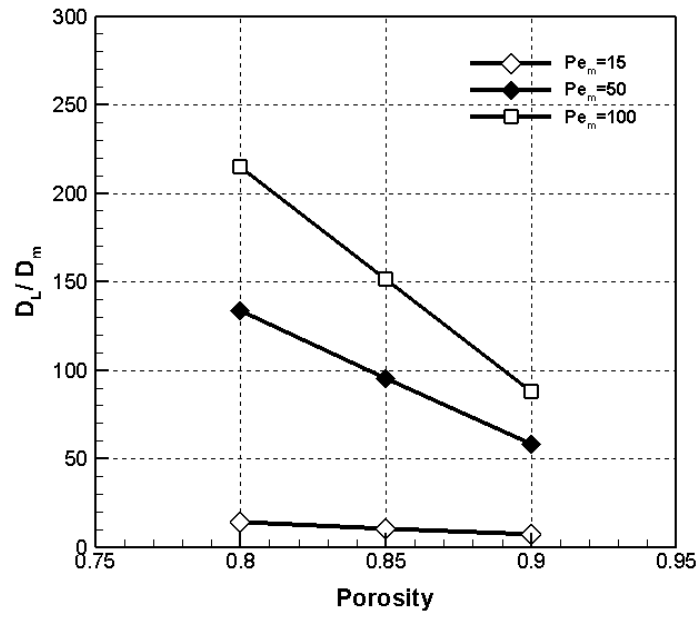
$$D_L = \frac{D_m}{\tau} \quad (5.12)$$



(a)



(b)



(c)

Figure 5.7: (a) & (b) Ideal & randomized structure of 10 PPI with different porosities (c) Comparison of longitudinal dispersion coefficient with porosity and molecular Peclet number.

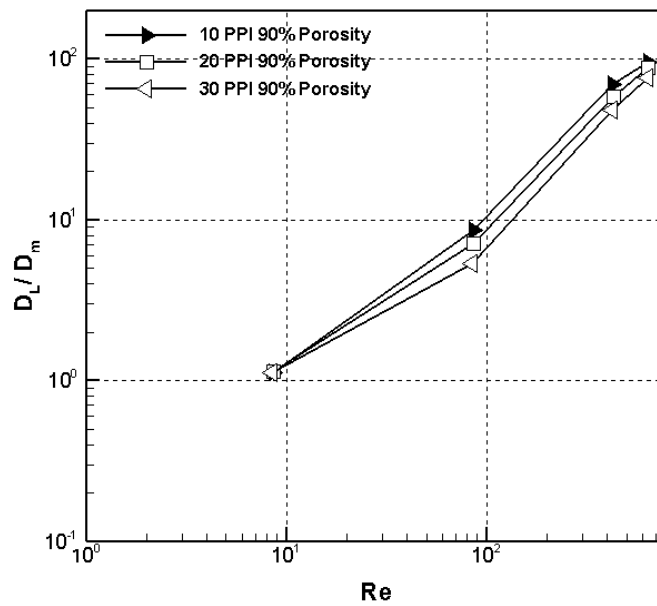


Figure 5.8: Ideal Kelvin structures of 10, 20, 30 PPI with constant (90%) Porosity.

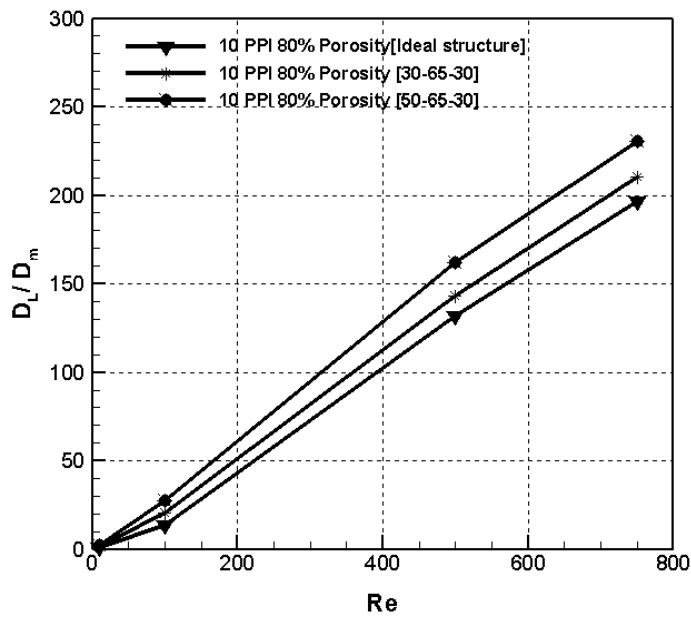


Figure 5.9: The LDC Comparison of ideal and randomized Kelvin structures at 10 PPI 80% porosity.

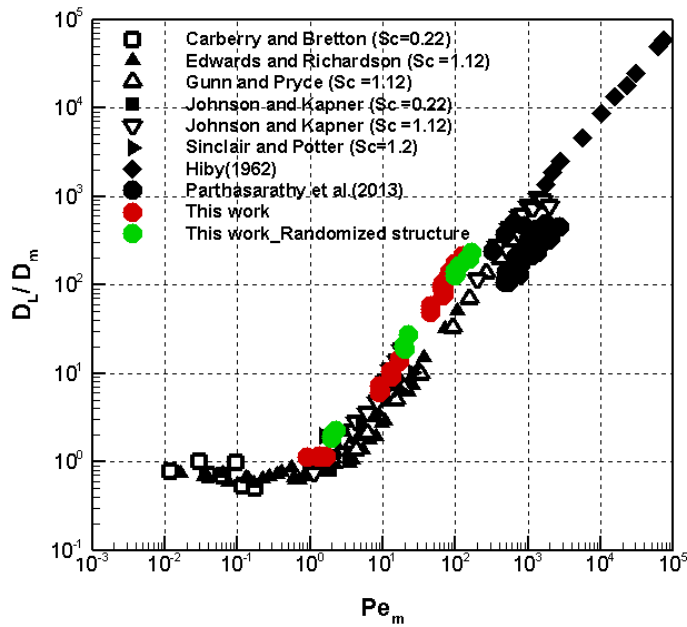


Figure 5.10: Longitudinal dispersion between Kelvin structures vs packed beds (gaseous flow data adopted from Delgado 2006).

Table 5.1: The simulated LDC results of various structures used in this study.

Structure name	Open porosity [-]	strut dia[m]	S_v [m^{-1}]	Pe_m	D_L/D_m	Pe_L
IDEAL 10 PPI 80% porosity	0.8006	0.000502	1369.806	1.68	1.12	1.49
				16.78	13.74	1.22
				83.92	139.38	0.60
				125.89	214.59	0.59
IDEAL 10 PPI 85% porosity	0.8438	0.000425	1257.771	1.33	1.12	1.19
				13.25	10.46	1.27
				66.28	104.32	0.64
				99.42	172.56	0.58
IDEAL 10 PPI 90% porosity	0.8957	0.000339	1069.004	0.92	1.12	0.82
				9.21	8.66	1.06
				46.04	69.07	0.67
				69.05	94.97	0.73
IDEAL 20 PPI 80% porosity	0.7946	0.000251	2722.175	1.67	1.14	1.47
				16.71	14.34	1.17
				83.54	131.89	0.63
				125.31	204.02	0.61
IDEAL 20 PPI 85% porosity	0.8433	0.000212	2470.175	1.30	1.14	1.14
				12.98	9.92	1.31
				65.52	95.20	0.69
				98.36	168.74	0.58
IDEAL 20 PPI 90% porosity	0.8968	0.000169	2123.001	0.91	1.14	0.80
				9.15	7.14	1.28
				45.76	58.23	0.79
				68.65	87.84	0.78
IDEAL 30 PPI 80% porosity	0.7969	0.000167	4110.683	1.67	1.15	1.46
				16.74	14.35	1.17
				83.72	133.83	0.63
				125.58	214.94	0.58
IDEAL 30 PPI 85% porosity	0.847	0.000142	3774.329	1.33	1.16	1.14
				13.28	9.01	1.47
				66.40	75.02	0.89
				99.61	164.87	0.60
IDEAL 30 PPI 90% porosity	0.8962	0.000113	3192.442	0.91	1.12	0.82
				9.14	5.31	1.72
				45.72	48.05	0.95
				68.58	76.92	0.89

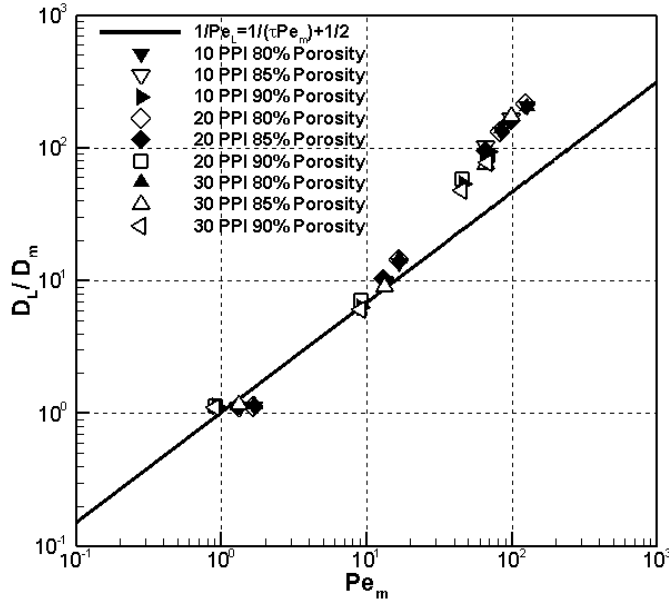


Figure 5.11: The DPLS results of longitudinal dispersion of all foam structures used in this study.

At high Pe number, numerous investigations have found that the axial Pe number (Pe_L) of packed beds attaining an asymptotic value of 2 for gas dispersion in packed beds (Edwards and Richardson 1968; Prausnitz 1958; Aris and Amundson 1957). Therefore

$$D_L = 0.5ud_p \quad (5.13)$$

In the intermediate zone, Edwards and Richardson (1968) defined the D_L by sum of the diffusion coefficient and the random mixing

$$D_L = \frac{D_m}{\tau} + 0.5ud_p \quad (5.14)$$

The above Eq. (5.14) states that, at low Peclet numbers, D_L is directly proportional to the molecular diffusivity, and at high Peclet numbers, it is independent of molecular

diffusivity. Gunn and Pryce (1969) rewritten Eq. (5.14) in the dimensionless form as

$$\frac{D_L}{D_m} = \frac{1}{\tau} + \frac{1}{2} \frac{ud}{D_m} \quad \text{or} \quad \frac{1}{Pe_L} = \frac{1}{\tau Pe_m} + \frac{1}{2} \quad (5.15)$$

The above Eq. (5.15) is anticipated to provide the correct asymptotic behavior in gas and liquid flow through packed beds at both high and low values of Pe_m . For gases, it is shown in Figure 5.12 the Pe_L of the DPLS results is plotted against the Pe_m and is compared with results available in the literature (Delgado 2006) on packed beds (in packed beds, the Peclet number is calculated based on the particle diameter). It can be observed that the Pe_L obtained is lower than the value of 2, and significant deviation is found compared to Eq. (5.15). This deviation is corrected by introducing modifying characteristic length.

As discussed earlier, the longitudinal dispersion in packed beds mainly depends on the packing particle shape and size, so that, the characteristic length is used as particle diameter. Similarly, in this study, the longitudinal dispersion dependency in Kelvin structure is verified using pore diameter and strut diameter as characteristic length. Among the two, the strut diameter shows good agreement with Eq. (5.15) (refer Figure 5.13) and also with literature data (refer Figure 5.12).

In order to represent the Pe_L of the Kelvin structure with that of the packed bed, a modified characteristic length correlation (Eq. 5.16) is proposed as a function of strut dia and flow tortuosity by fitting a linear curve to meet the value of 2. A similar concept is noted in Parthasarathy *et al.* (2013), but the author correlated with respect to pore dia. where the calculation of flow tortuosity is discussed in the next section.

$$d = d_s(-5.2 + 6.7\tau) \quad (5.16)$$

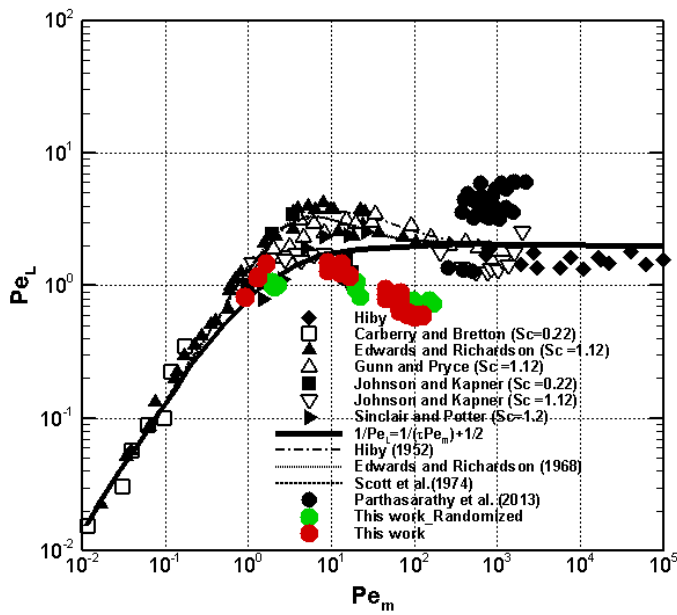


Figure 5.12: Comparison of longitudinal Peclet number in ideal and randomized Kelvin structures versus correlation provided for packed beds, where Pe calculated based on strut diameter (data adopted from Delgado 2006).

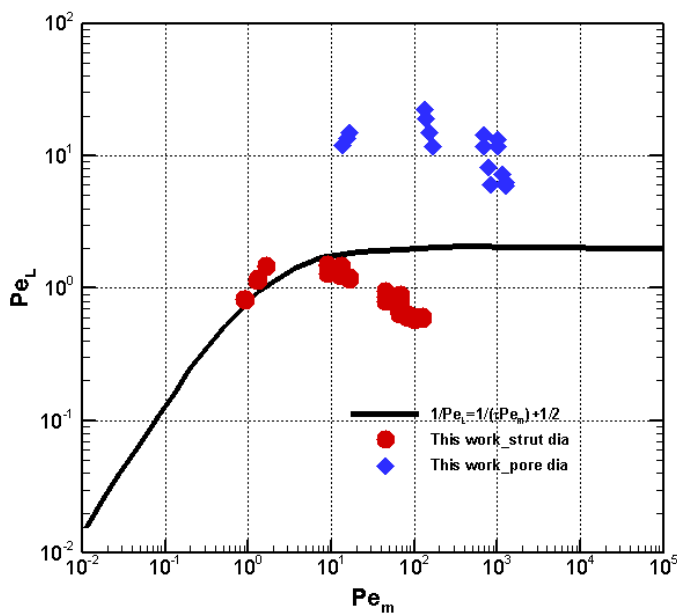


Figure 5.13: Comparison of longitudinal Peclet number with pore and strut diameter.

5.5.2 Determination of flow tortuosity

The complete transport phenomenon in open-cell foams describes not only by porosity, pore density (PPI), and a specific surface area along by another essential parameter as required, i.e. tortuosity. In recent years, the behaviour of tortuosity flow in porous media has attracted considerable attention. Moreira and Coury (2004a) determined the tortuosity by measuring the electric resistivity of the medium. In this study, the influence of flow tortuosity is calculated by the approach used by Habisreuther *et al.* (2009) and Parthasarathy *et al.* (2016). The authors suggested a simple procedure for determining tortuosity in DPLS by tracing a particle trajectory within the investigated structure. The integration of particle tracking will give directly results in the extended flow path L_P . According to the definition of tortuosity; $\tau = L_p/L$ where L is the porous domain length. Using the Lagrangian particle tracking (LPT) method, the particle is tracked in the Eulerian fluid phase flow. i.e. individual particles are tracked from the inlet to outlet of the domain. The Euler integration forward algorithm is used to calculate each particle's traveling distance. This is the common most algorithm for fluid flow solvers. Nearly 30,000 particles are analyzed in each simulation with the size all most mass-free particles of $1\mu\text{m}$ diameter with a density of $2000\text{ Kg}/\text{m}^3$. Due to this, the particle velocity will easily reach the flow velocity. In this study, only the drag force experienced by the particle was considered, and the drag coefficient was calculated using Schiller and Naumann (1935) model, with a limiting value of 0.44 in the inertial regime. Thus, the mean tortuosity values are tabulated in Table 5.2.

Therefore while incorporating the flow tortuosity and strut diameter, a modified characteristic length scale correlation is proposed and calculated the Peclet number. Figure 5.14 depicts the results of D_L/D_m versus modified Pe_m . It is evident that the modified characteristic length scale works well with literature data. Similarly, in Figure 5.15, the modified Peclet number of Kelvin structures are compared with the Eq. (5.15). It is seen that in the intermediate zone (i.e., $5 < Pe_m < 40$), the calculated Pe_L values are just higher than predicted by Eq.(5.15). After the intermediate zone, the Pe_L reaches an

Table 5.2: Tortuosity values of different foam structures determined using DPLS.

Foam description	Nominal porosity (%)	Tortuosity(τ)
Ideal 10 PPI	80%	1.0931
	85%	1.0748
	90%	1.0503
Ideal 20 PPI	80%	1.0859
	85%	1.062
	90%	1.0385
Ideal 30 PPI	80%	1.0712
	85%	1.0481
	90%	1.0268

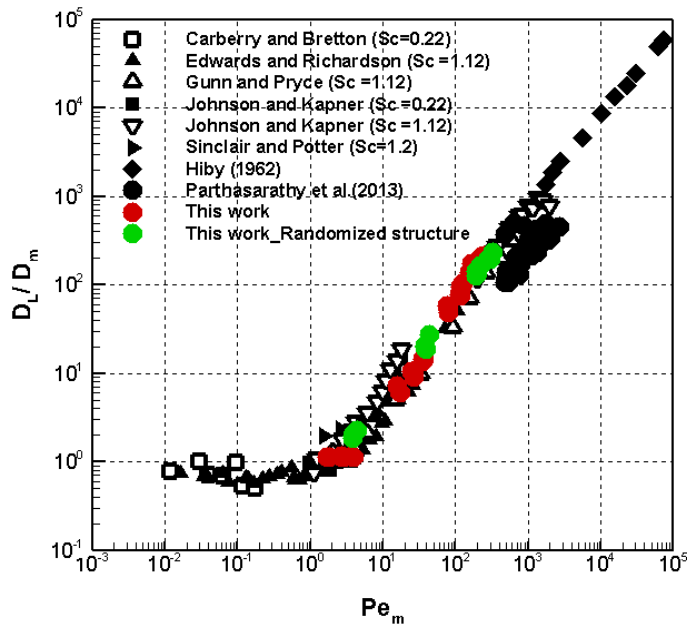


Figure 5.14: Comparison of modified molecular Peclet number versus longitudinal dispersion of gaseous flow in ideal and randomized Kelvin structures.

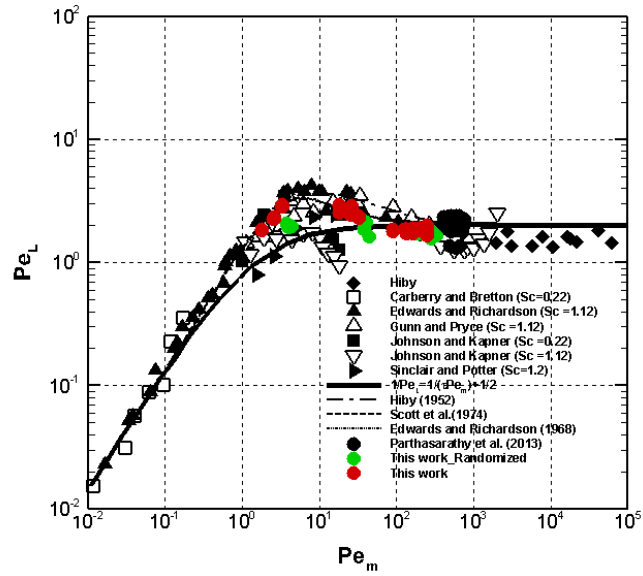


Figure 5.15: Modified longitudinal Peclet number versus modified molecular Peclet number of ideal and randomized Kelvin structures (using correlated characteristic length given by Eq. 5.16).

almost constant value of 2 and follows Eq. (5.15) at high Peclet numbers. A similar kind of observation is noted in the packed bed structure's literature (Hiby 1962; Edwards 1968; Scott *et al.* 1974; Gunn and Pryce 1969; Johnson and Kapner 1990; Sinclair and Potter 1965; Carberry and Bretton 1958). It is also seen that in the intermediate zone, the present study values fit well with existing correlations data of Hiby (1962), Edwards (1968), and Scott *et al.* (1974). Thus it is concluded that, with the correlated characteristic length scale (Eq. 5.16), the Pe_L of the ideal and randomized Kelvin structures are nearly equal to the packed bed data that are reported in the literature.

5.5.3 Comparison of Kelvin porous structures with real porous structures

In Figure 5.12, the Pe_L results of real porous structures Parthasarathy *et al.* (2013) are plotted and compared with Eq. (5.15). It is observed that the Pe_L value is much higher than the value of 2. The reason is noticed that pore diameter is used as a char-

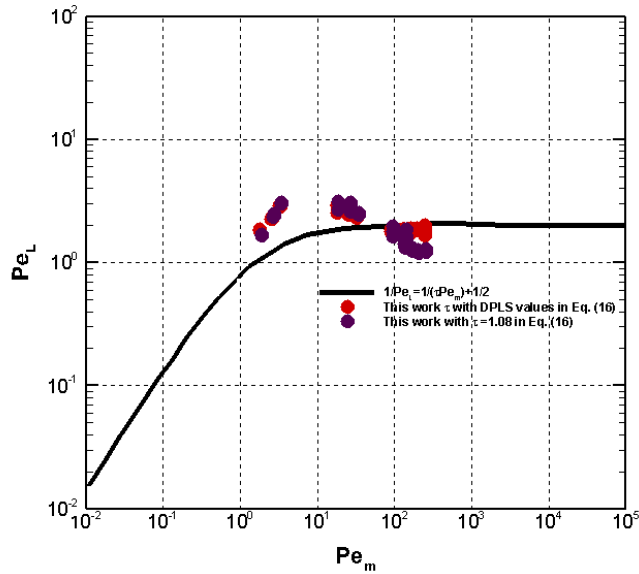


Figure 5.16: Peclet number calculated with the modified characteristic length correlation (Eq. 5.16) using present study tortuosity values (refer Table 5.2) and Habisreuther *et al.* 2009 tortuosity value ($\tau = 1.08$).

characteristic length to calculate Pe_L . Then the author modified the characteristic length and formulated a new correlation to estimate the Pe_L . Therefore, the modified Pe_L values approximately match the value of 2 shown in Figure 5.15. i.e. it is seen that the real porous structures can also exhibit a similar dispersion trend with packed beds and Kelvin structures. Due to the complexity of real porous geometry, it is difficult to describe exact geometrical properties, leading to different results in different studies.

However, as it is known, it is challenging to calculate flow tortuosity experimentally, and even numerical calculations require high computational power. So, Habisreuther *et al.* (2009) suggested a unique mean tortuosity value for ordered Kelvin structures as 1.08. In this study $\tau = 1.08$ is used to calculate the Pe_L with modified characteristic length correlation (Eq. 5.16) and compared with present study values and plotted in Figure 5.16. It is observed that the Pe_L values are approximately equal to the literature data as well as present study data.

5.6 Conclusion

In this chapter, numerical simulations were performed to evaluate the LDC values in reticulated Kelvin structures. The 3D foam geometries were used the same as that of the pressure drop study of porosities 80%, 85%, and 90% and 10, 20, and 30 PPI. The flow simulations were performed at different flow rates, using the standard CFD-finite volume discretization approach (using ANSYS-CFX solver), and the flow calculations were solved using conventional Navier-stroke equations. A parametric study was conducted to verify the influence of porosity, pore density, and mass flow rate on LDC and noted the following observations.

1. The LDC enhances with increasing flow velocity and decreasing porosity. i.e., due to decreasing porosity, the pore-scale model showed greater velocity fluctuations, resulting in greater mixing in the pores attained.
2. For the same porosity, the LDC decreases while increasing PPI. i.e., this is primarily due to a reduction in pore diameter with an increase in PPI.
3. The randomized structure showed higher LDC compared to ideal structures due to the randomization effect.
4. In addition, a new correlation was presented to evaluate the characteristic length scale based on strut diameter and flow tortuosity. With the correlated characteristic length scale, the Peclet number of the ideal and randomized Kelvin structures was nearly equal to the packed bed data as well as real porous data that are reported in the literature.

Therefore, this study helps to evaluate effective LDC in highly porous reticulated open-cell foam structures.

5.7 Closure

The numerical procedure to characterize the longitudinal dispersion coefficients in various open-cell porous structures was dealt in this chapter. A detailed parametric study was performed and a new characteristic length based correlation is proposed to determine the longitudinal Peclet number. The calculated Peclet number values were in good agreement with the literature results of the packed bed and real porous structures. The heat transfer analysis was explained in the next chapter.

CHAPTER 6

CONVECTIVE HEAT TRANSFER COEFFICIENT IN RETICULATED KELVIN STRUCTURE

6.1 Introduction

The heat transfer in porous media involved two phases, i.e., a solid phase (struts or ligaments or fibres) and a fluid phase (flow within the porous domain). In some cases, the solid temperature is in equilibrium with the flowing fluid, which is described as local thermal equilibrium (LTE). But in the case of a single-phase fluid flow, the presumption of LTE is not valid in all thermal applications. For example, when porous media are used in combustors, there is enough amount of heat liberated in the fluid phase, which prevents the local solid and fluid volumes from being in thermal equilibrium. Furthermore, when interstitial fluid flow within the porous structure differs significantly from the thermal properties of the solid phase, the local temperature change between the two phases will be different. As a result, there is a temperature gradient at the point where the solid obstruction meets the nearby fluid; this scenario is called as local thermal non-equilibrium (LTNE). Therefore, to determine heat transfer in such applications, 2-phase energy equations are needed: one for solid and one for fluid, respectively.

However, to solve the 2-phase energy equations, the solid and fluid phases must need effective heat transport properties. Where, the convective heat transfer between solid and fluid phases is described using an interfacial convective HTC to couple the two energy equations. Thus, the measurement of effective HTC is crucial for obtaining accurate results in the 2-phase model.

A detailed overview of the 2-phase model or 2-equation model is provided by Wakao and Noriaki (1982):

For fluid:

$$\frac{\partial \bar{T}_f}{\partial t} + \bar{u} \frac{\partial \bar{T}_f}{\partial x} = \frac{1}{\varepsilon} \left(\frac{\bar{k}_f}{(\rho c_p)_f} + D_L \right) \frac{\partial^2 \bar{T}_f}{\partial x^2} + \frac{h_{sf} S_V}{\varepsilon (\rho c_p)_f} (\bar{T}_s - \bar{T}_f) \quad (6.1)$$

For solid:

$$\frac{\partial \bar{T}_s}{\partial t} = \frac{\bar{k}_s}{(1 - \varepsilon) (\rho c_p)_s} \frac{\partial^2 \bar{T}_s}{\partial x^2} - \frac{h_{sf} S_V}{(1 - \varepsilon) (\rho c_p)_s} (\bar{T}_s - \bar{T}_f) \quad (6.2)$$

where k_s and k_f referred to as the thermal conductivity of solid and fluid, D_L is the longitudinal dispersion coefficient (Ref: 5), S_V is the specific surface area and h_{sf} is the interfacial HTC.

In open-cell foam materials, the HTC is defined in two ways, such as the wall or global HTC (h_w) and the local interfacial (h) or volumetric HTC (h_v). As the solid matrix has a significant impact on the fluid HTC in porous media, significant effort is required to determine these parameters. The wall HTC measures the overall augmentation of heat transfer from the wall surfaces to the attached porous geometry. This coefficient can be used to design cooling applications for electronic devices (Calmidi and Mahajan 2000a; Bhattacharya and Mahajan 2002; Bianchi *et al.* 2013). The local interfacial or VHTC defines the heat exchange between the solid phase and the flowing fluid. It can be used for thermal energy absorbers, radiant porous burners, building thermal insulation, compact heat exchangers, packed cryogenic micro sphere insulation, combustors, chemical and biological reactors (Kaviany 1995, Rashidi *et al.* 2017; Sertkaya *et al.* 2012, Mujeebu *et al.* 2010). In the literature, due to non availability of the specific surface area of foams, many authors (Younis and Viskanta 1993; lin Xia *et al.* 2017; Wu *et al.* 2011, Kamiuto and Yee 2005) analyzed heat transfer in foam material by adopting the VHTC. Because of the complexity of porous morphology, it is difficult to measure the specific surface area values. In this study, the interfacial and volumetric HTCs are used to study the comparative effects with literature data. The VHTC (h_v) can be calculated from the following equation:

$$h_v = h \cdot s_v \text{ with } h_v = W.m^{-3}.K^{-1} \quad (6.3)$$

6.2 Problem statement

In this chapter, DPLS are performed to measure the interfacial and VHTC in the same structures that are used in the pressure drop study of porosities (80%, 85%, and 90%) and PPI (10, 20, and 30 PPI) under various working fluids (air, water and saltwater). Based on simulation outcomes, the Nusselt number correlation are to be proposed in terms of the Reynolds number and Hagen number. In the literature, many researchers have proposed HTC correlation using the Nu-Re analogy but have not found much research on estimating HTC from pressure drop data. This research intends to provide HTC prediction using the existing pressure drop data in reticulated porous structures. The proposed correlations are validated with existing literature data.

6.3 Numerical setup and post-processing

6.3.1 Governing equations and boundary conditions

As reported earlier in the literature, the HTC in open-cell foam examined through the steady-state method and transient method. In both methods, the results are global and lead to averaged coefficients. So, to keep computational cost at a minimum, in this study, the simulations are performed by assuming a steady-state method. Additionally, working fluids are assumed as Newtonian fluid and in-compressible having constant densities and viscous dissipation is neglected. The simulations are accomplished by solving governing equations of mass (4.7), momentum (4.8) and energy

$$\frac{\partial}{\partial x_j}(\rho u_j c_p T) = \frac{\partial}{\partial x_j} \left(k_f \frac{\partial T}{\partial x_j} \right) \quad (6.4)$$

where ρ denotes the density of the fluid, u_j and x_j represents velocity and spatial coordinate in the j-direction, T represents the fluid temperature, c_p indicates the specific heat of fluid, and k_f is the fluid thermal conductivity, respectively. The governing equations are solved using the standard CFD-FVM method (using ANSYS-CFX software) with a

high-resolution scheme and convergence criterion has been set at 10^{-6} . The boundary conditions defined for the present work are shown in Figure 6.1 and are explained below

1. The inlet of the porous domain specified as uniform velocity and temperature (300K).
2. The outlet boundary specified with static pressure with zero gauge pressure condition.
3. The structure surfaces are defined as wall(no-slip) with fixed strut temperature ($T_w=1000$ K).
4. The four side surfaces are specified with translational periodic boundary conditions.

Additionally, to obtain a fully developed flow, the domain size has been maintained a minimum of 10 pores and utmost of 15 pores in the flow passage as suggested in Diani *et al.* (2014).

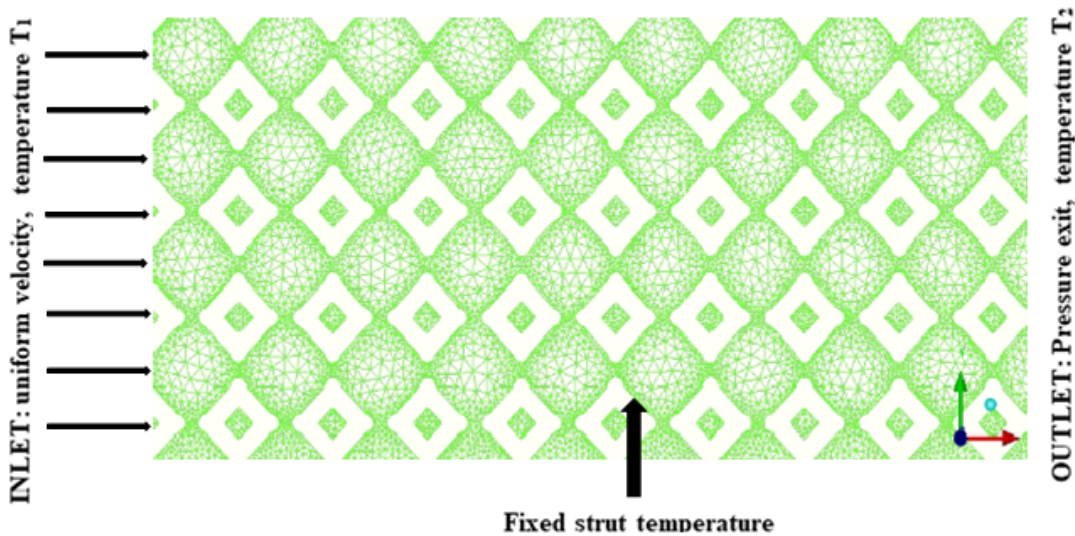


Figure 6.1: The grid of an ideal Kelvin structure was created using ICFM CFD and boundary conditions applied.

6.3.2 Numerical procedure

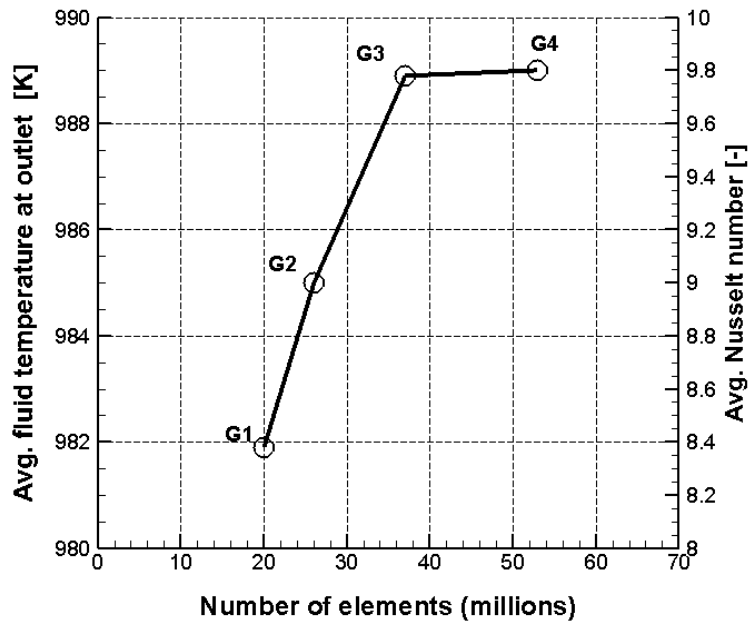
In the present work, the strut surfaces are maintained at constant temperature (T_W) which is higher than that of entering fluid. The heat from the strut surfaces is then transported by convection and diffusion. In order to determine the interfacial HTC from the simulations, the 3-Dimensional temperature fields are minimized to 1-Dimensional temperature fields by averaging mass flow over N perpendicular cross-sectional planes to the primary flow direction.

$$\overline{T(x_k)} = \frac{\sum_{i=1}^G (T_i \cdot \rho u_i A_i(x_k))}{\sum_{i=1}^G \rho u_i A_i(x_k)} \quad (6.5)$$

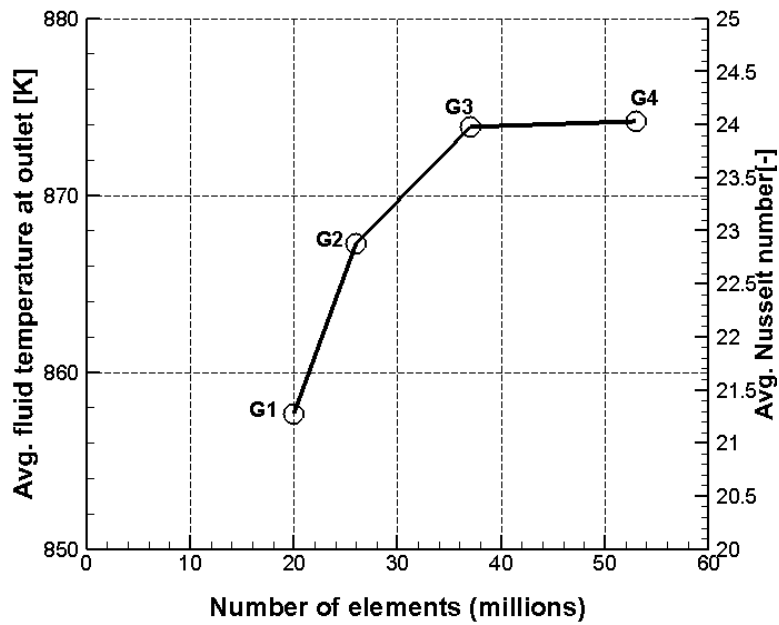
$\overline{T(x_k)}$ indicates the mass flow avg. temperature at the $K - th$ cross-sectional plane at the location x_k , $\rho u_i A_i(x_k)$ denotes the mass flow in the plane with the $i - th$ grid cell, G is the no. of grid cells and T_i is the temperature value in the $i - th$ grid cell.

6.3.3 Grid generation

The modelled Kelvin geometries are imported to a commercial grid generating software (ICEM CFD) to acquire computational grids. In order to achieve accurate results and minimizing the computational time & errors, the grid-independent studies are performed for four different sizes of grids (G1, G2, G3, and G4) at different Reynolds numbers (100 and 750) that are shown in Figure 6.2a and 6.2b . In Figure 6.2a and 6.2b, the grid study shown with respect to average fluid temperature (outlet) and average Nusselt number. With increase in number of grid elements, the average fluid temperature and Nusselt number difference approach the minimum. Comparing four grids, the G3 & G4 grid results seem to be independent of mesh resolution, indicating grid independency. But compare to G3 & G4, G3 has 37 million grid elements, and G4 has 53 million grid elements, respectively. So, to minimise the computational time in this study, a less number of grid elements (G3), i.e., 37 million grid size is used for



(a)



(b)

Figure 6.2: Grid study of 30 PPI 80% (a) Re=100 (b) Re=750

further analysis.

6.4 Results and discussions

6.4.1 Determination of heat transfer coefficient(HTC)

In this study, reticulated porous structures that are ideal and randomized Kelvin structures are used to analyze heat transfer with the help of DPLS. The Analysis is carried out at Re of 10, 100, 500 and 750 for different fluid properties, including air (Pr=0.7, $k_f = 0.0261 \text{ W/mK}$) saltwater (Pr=2, $k_f = 0.671 \text{ W/mK}$) and water (Pr=6, $k_f = 0.6069 \text{ W/mK}$). The Reynolds numbers ($Re = \rho d_h u_s / \varepsilon \mu$) are determined by using hydraulic diameter ($d_h = 4\varepsilon / S_V$) as the characteristics length.

According to the equation below, the local HTC between axial locations x_k and ($x_k + \Delta x_k$) is defined as:

$$h_l(x_k) = \frac{\int_{x_k}^{x_k + \Delta x_k} \dot{q} dA_{s_f}}{A_{s_f} \Delta T_{lm}} \quad (6.6)$$

where $\Delta T_{lm} = \frac{\Delta T_{x_k} - \Delta T_{(x_k + \Delta x_k)}}{\ln(\Delta T_{x_k} / \Delta T_{(x_k + \Delta x_k)})}$ is the LMTD, while $\Delta T_{x_k} = T_w - \overline{T(x_k)}$, \dot{q} is the heat flux and T_w is the wall temperature which is a constant. Post processing is done by dividing the total flow domain along the flow into multiple sections and calculated the ΔT_{LMTD} and (\dot{q}) for each section. From which, the heat transfer coefficients are determined.

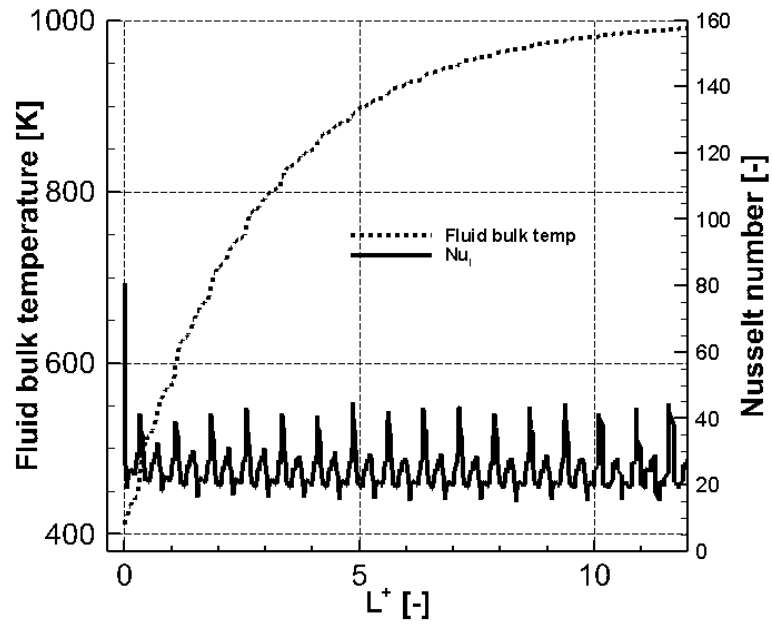
From Figure 6.3 (a & b), the local Nusselt number ($Nu_l = \frac{h_l d_h}{k_f}$) and fluid bulk temperature of ideal and randomized Kelvin structures at $Re = 500$ plotted against the normalized axial length ($L^+ = \frac{L}{d_h}$). It is seen that, the Nusselt number is very high at the entrance due to the air accelerating at the windward side of the porous domain and directly hits the surface of solid. i.e., except for the entrance, the Nu values are approximately constant in the axial direction. A similar tendency was reported in Wu *et al.* (2011) and Parthasarathy (2016). In Figure 6.3b, because the fluid is slowed down

by the randomization of the geometry, it observe that Nusselt number fluctuations are not regular in randomized structure. Therefore, by ignoring the peak Nusselt numbers at the entrance, the arithmetic average of the Nusselt number along the axial direction is considered as average Nusselt number (Nu) of the porous domain.

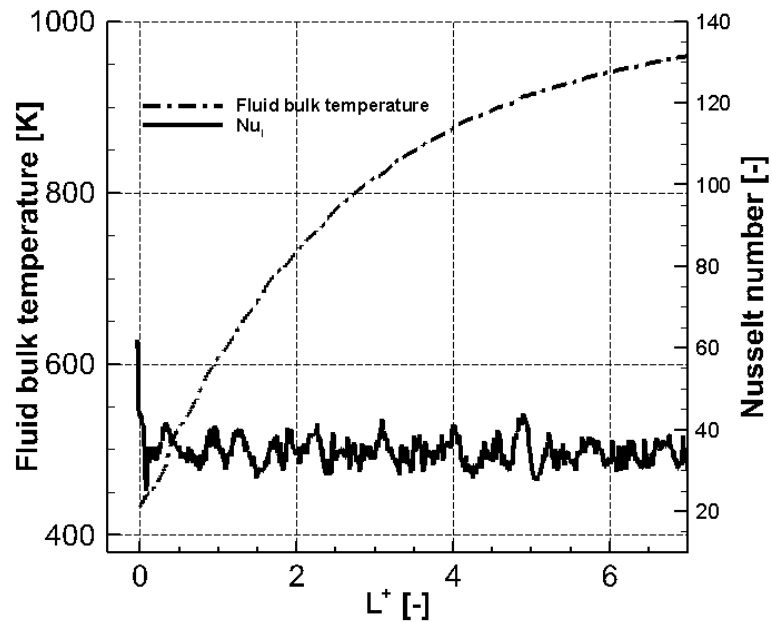
Figure 6.4 (a-c) illustrate PPI's effect on the VHTCs at different working fluids. It is revealed that the VHTC increase as the pore density increases. The same trends as those in the literature are observed (Dietrich 2013; Younis and Viskanta 1993; Parthasarathy 2016; lin Xia *et al.* 2017). It is discussed in Younis and Viskanta (1993), that the increase in PPIs decreases the pore diameter, which in turn increase the specific surface area of foams at the same porosities (Ref. Table 4.1). It is evident that the VHTC increases with the specific surface area.

Figure 6.5 (a-d) plotted the effect of porosity on VHTC in ideal and randomized Kelvin structures for various working fluids. It can be observed that the VHTC decreases with increasing porosity with keeping PPI constant. It is mainly a result of the depletion in the strut diameter, which led to a decrease in the specific surface area while the porosity is increased. A similar kind of tendency is reported in lin Xia *et al.* (2017). From Figures 6.4 and 6.5, it can also be observed that the VHTC increase gradually with the increase of velocity.

To study the effect of randomization, the ideal Kelvin structures are compared with randomized structures and it illustrated in Figure 6.6. It is seen that in comparison to ideal structures the VHTC increases even if the same porosity & PPI are maintained because of randomization of the foam (both specific surface area values are keeping close to the same value). Figure 6.7 illustrates the interfacial HTC's of various foams used in this study as they relate to the superficial flow velocity u_s . It is found that the geometrical properties (PPI and porosity) of the foam have no significant impact on the HTC. There are similar observations found in the literature (Dietrich 2013; Garrido *et al.* 2008 and Parthasarathy 2016). In Figure 6.7, one exception is observed in 30 PPI 80% porosity foam. Here, the HTC's are higher than other foams because of the higher specific surface area exposed in that foam (see. Table 4.1).

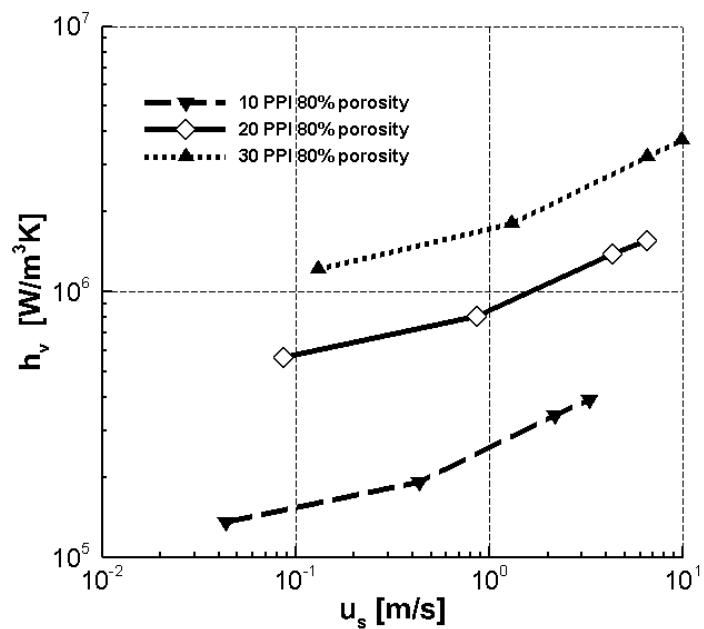


(a)

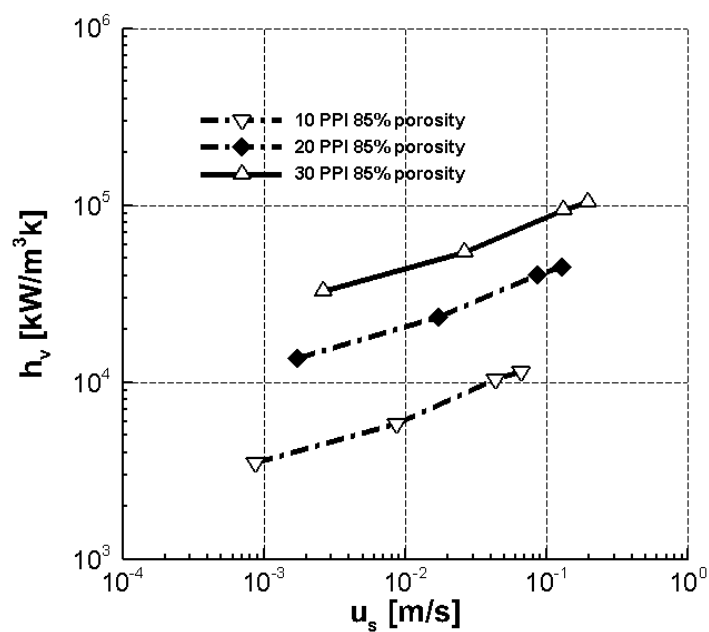


(b)

Figure 6.3: Local Nusselt numbers and fluid bulk temperature distribution along the flow direction (a) Ideal Kelvin structure 30 PPI 90% porosity (b) Randomized Kelvin structure 10 PPI 90% porosity[50-75-40] at $Re = 500$ and $Pr = 0.7$



(a)



(b)

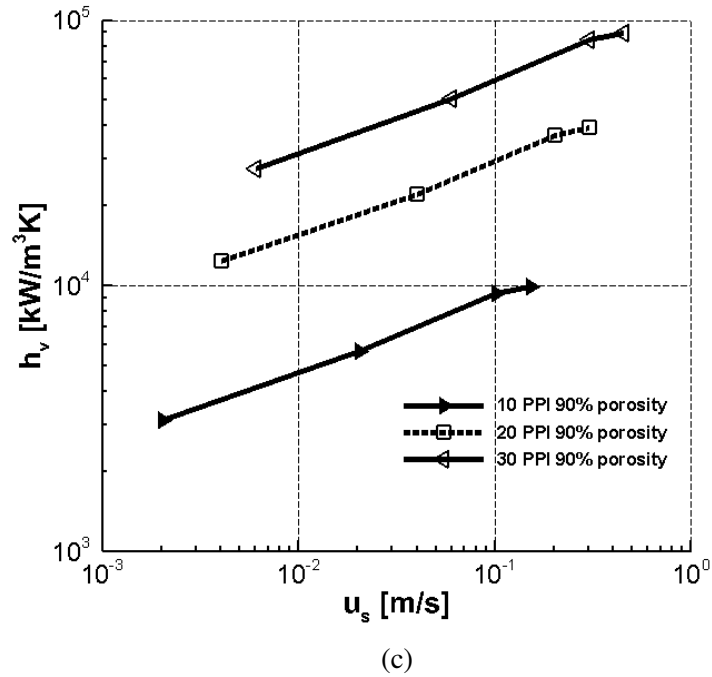
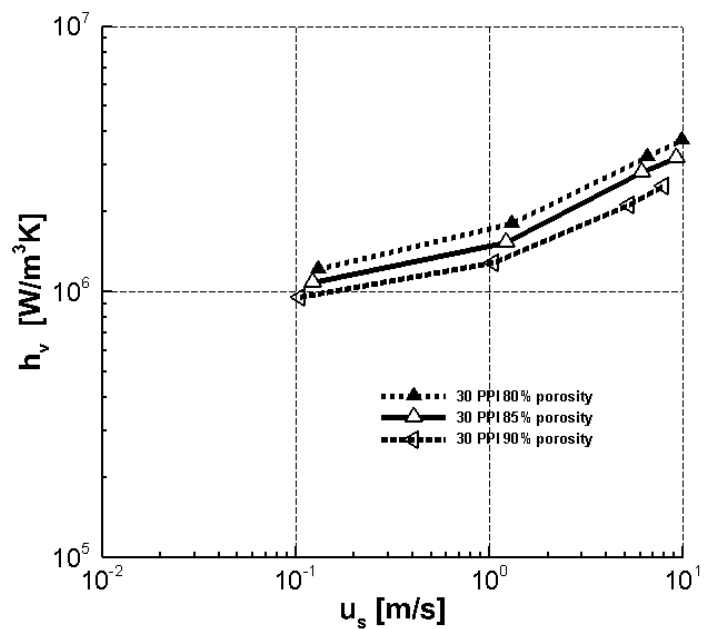


Figure 6.4: Effect of PPI (a) Pr=0.7, (b) Pr = 2 (c) Pr =6

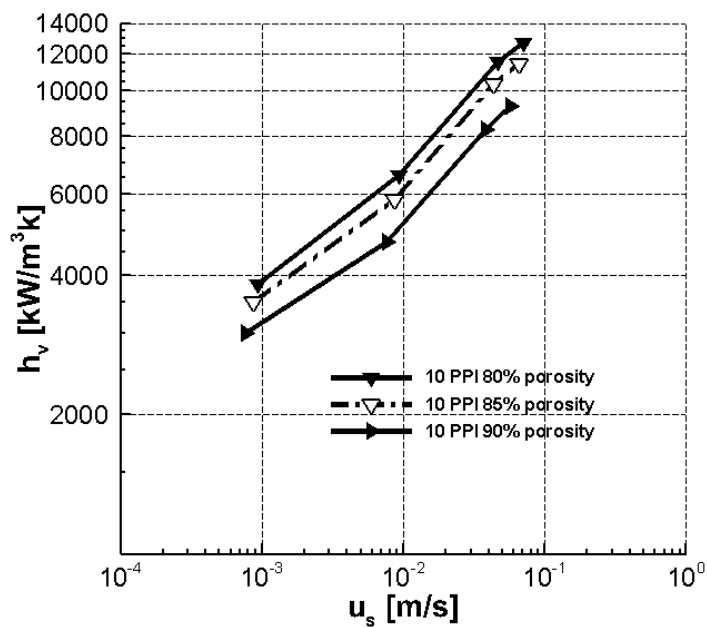
The flow field temperature contours at different Reynolds numbers (10 & 750) compared in Figure 6.8 (a-c) and Figure 6.9 (a-c). At the low Reynolds number (Re =10) cases, the fluid temperature reached thermal equilibrium within a short interval distance compared to Re =750. The reason is presumably that at a lower Reynolds number, the fluid flows at very low velocities, nearly 0.002 to 0.03 m/s. Due to this low velocity, the fluid has enough time to reach solid temperature. Besides, a higher Reynolds number results in a higher fluid velocity and a higher HTC. The same kind of results are observed in both ideal as well as randomized structures.

6.4.2 Heat transfer correlation based on Re

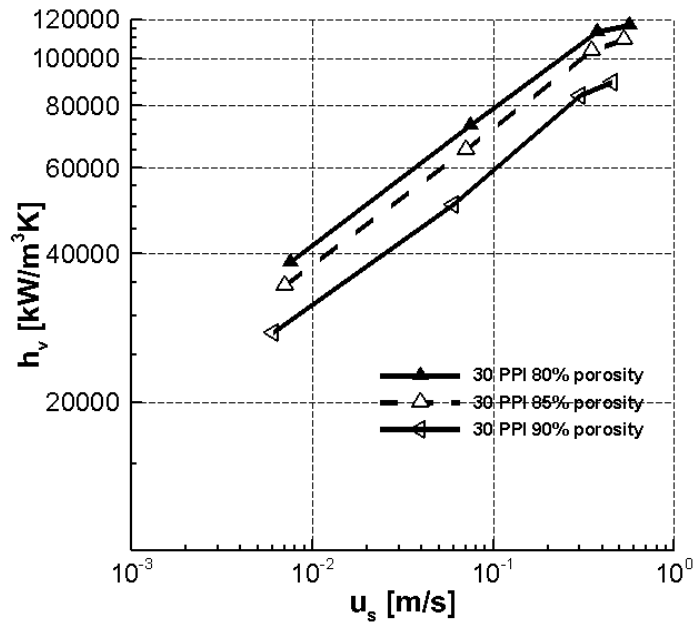
The Nusselt number and Reynolds number are computed using the hydraulic diameter as characteristic length and plotted in Figure 6.10. It is seen that the Nusselt number of ideal Kelvin structures with the same PPI and different porosities, foams with higher porosities have higher Nusselt numbers compared with low porosities. It



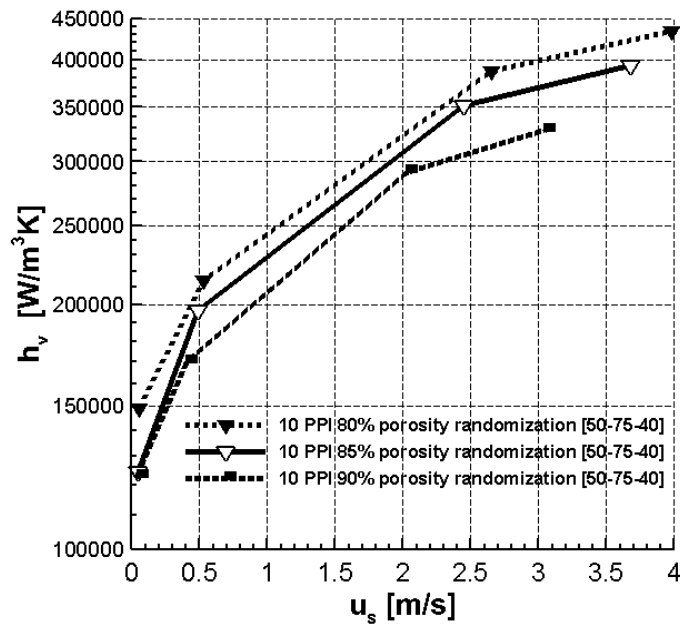
(a)



(b)



(c)



(d)

Figure 6.5: Effect of porosity (a-d) Ideal Kelvin structure of different working fluids ($\text{Pr}=0.7$, $\text{Pr}=2$ and $\text{Pr}=6$) and (d) randomized Kelvin structure ($\text{Pr}=0.7$)

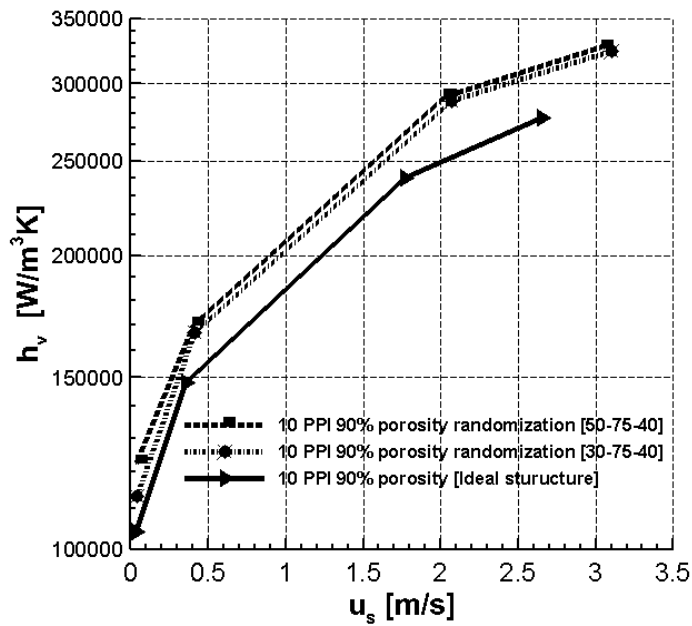


Figure 6.6: The VHTC for the ideal and randomized structure's comparison at 10 PPI 90% porosity ($Pr = 0.7$).

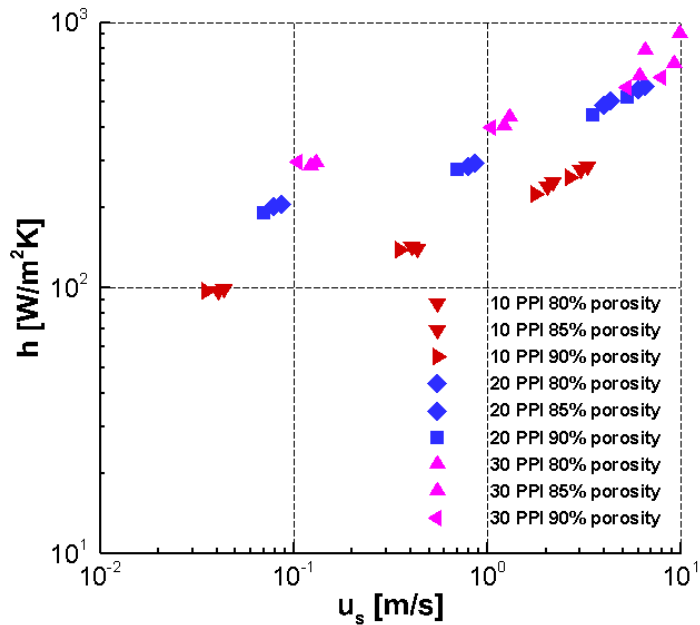
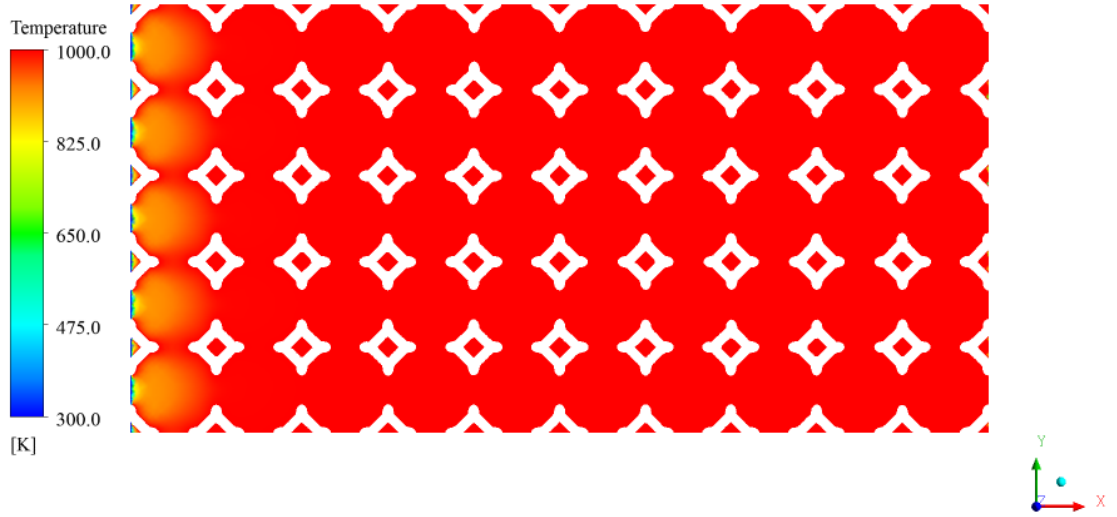
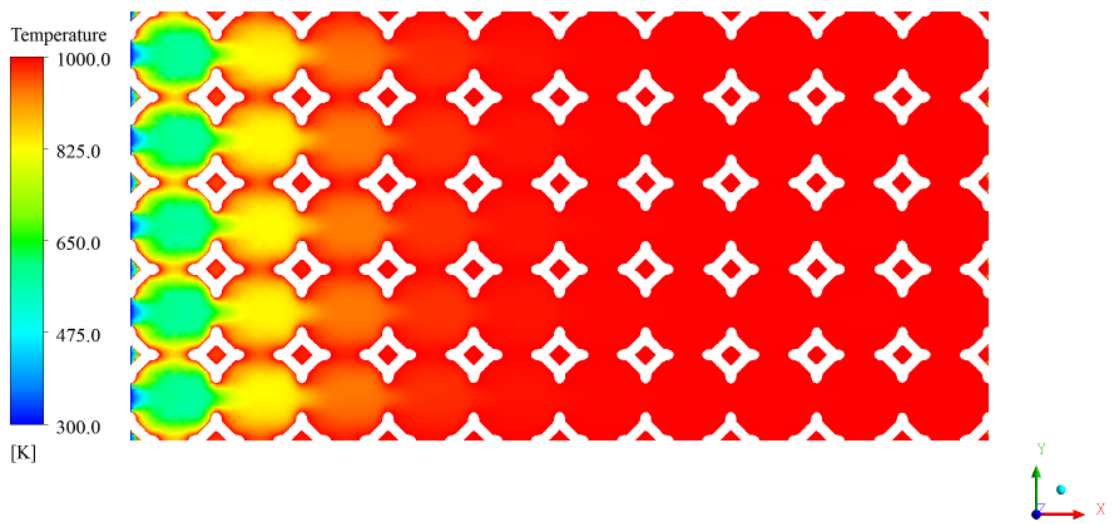


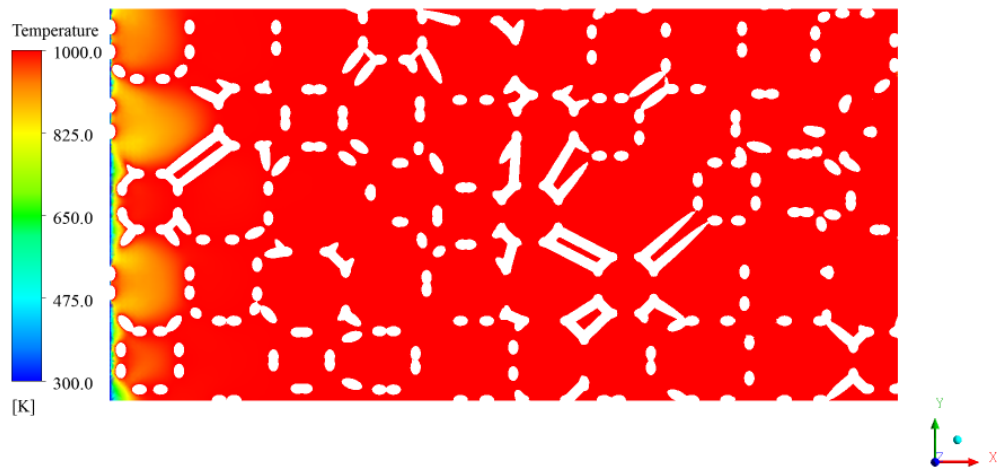
Figure 6.7: The comparison of all foams used in this study according to their DPLS results ($Pr = 0.7$)



(a)

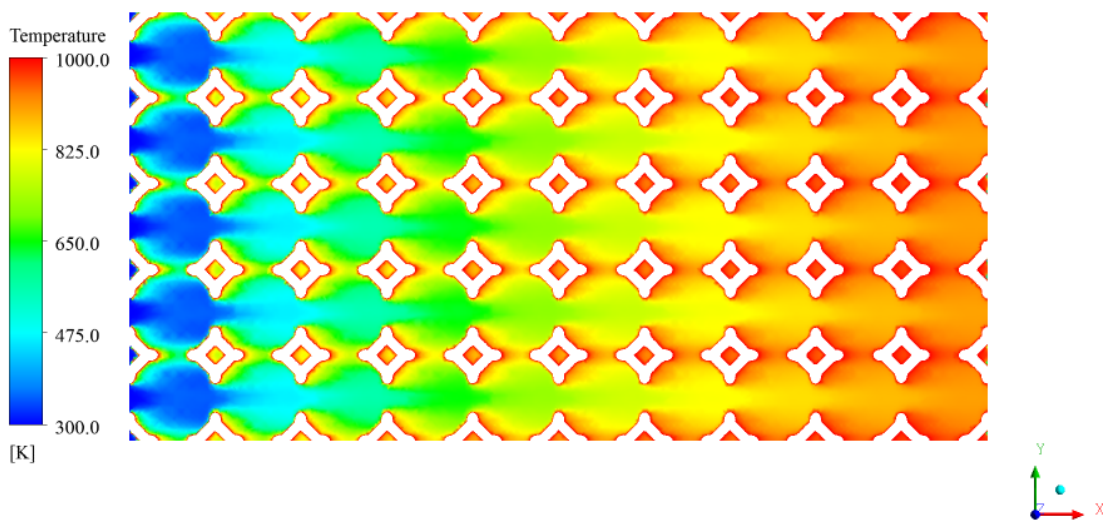


(b)

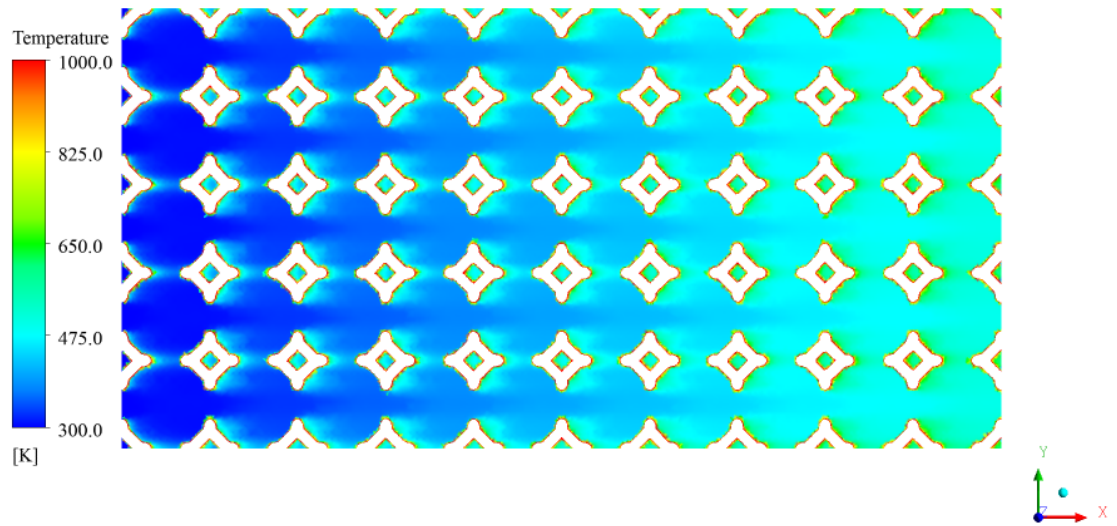


(c)

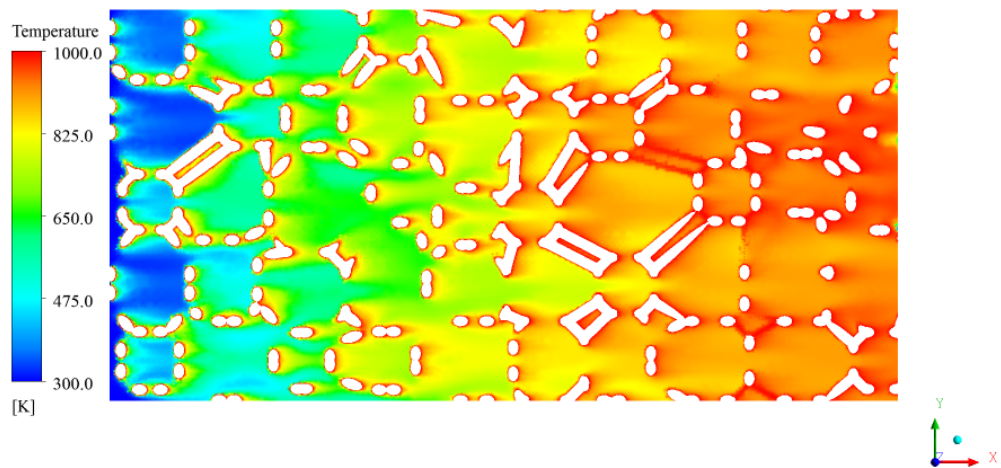
Figure 6.8: Temperature field contours (a) Ideal Pr =0.7 (b) Ideal Pr =6 and (c) Randomized Pr =0.7 of 10 PPI 90 % porosity at Re = 10



(a)



(b)



(c)

Figure 6.9: Temperature field contours (a) Ideal $Pr = 0.7$ (b) Ideal $Pr = 6$ and (c) Randomized $Pr = 0.7$ of 10 PPI 90 % porosity at $Re = 750$

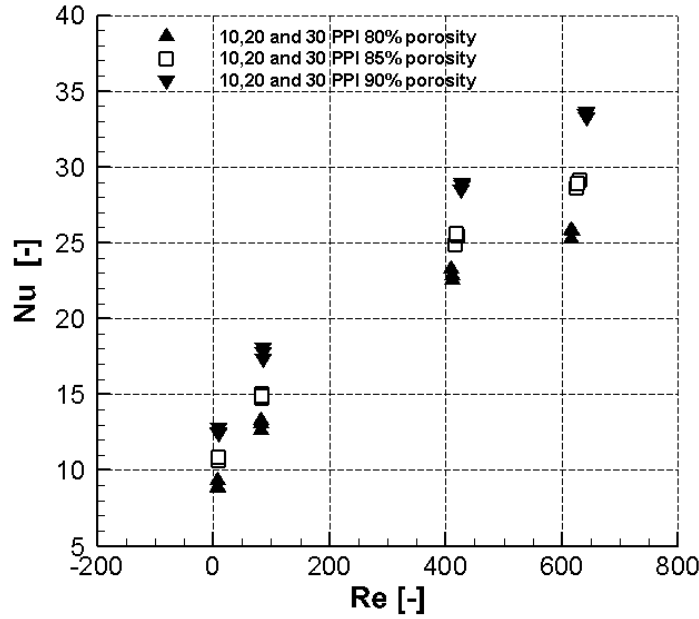


Figure 6.10: Comparing Nusselt number with Reynolds number for different porosities and PPI of ideal Kelvin structures ($Pr = 0.7$)

is also found that for the same porosity, different PPI numbers, the Nusselt numbers are approximately the same, i.e., it seems the Nusselt number is strongly dependent on the porosity. Thus, by incorporating this porosity dependency, the following correlation is established from the DPLS's Nusselt number results of all investigated structures by fitting the curve through minimizing the RMSD.

$$Nu = \frac{h \cdot d_h}{k_f} = 13.109\varepsilon^2 + 0.58\varepsilon^2 Re^{0.6} Pr^{1/3} \quad (6.7)$$

which is in the form of the following heuristic correlation proposed by Wakao and Noriaki (1982)

$$Nu = a + bRe^m Pr^n \quad (6.8)$$

Whitaker (1983) and Kuwahara *et al.* (2001) also proposed similar kinds of correlation that are discussed in the literature. In the present work, the coefficients a and b are obtained for different porosities to investigate the porosity dependency, and for the

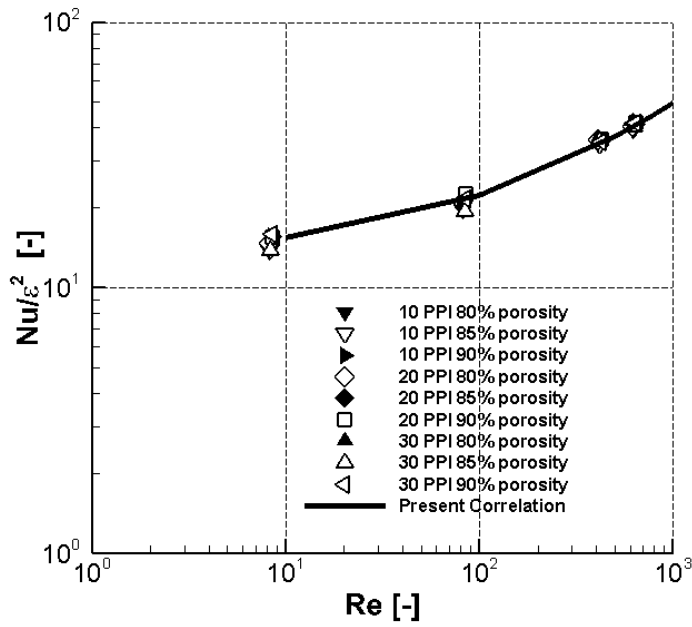
given porosity, the Reynolds number varies in proportion to $Re^{0.6}$ whereas the Prandtl number exponent 'n' can be fixed with 1/3. Thus, the proposed correlation fitted with a minimum RMSD of 4.55%, where RMSD is :

$$RMSD = 10^{RMSD(ELOG)} - 1; ELOG = \log(Nu_{calc}) - \log(Nu_{sim}) \quad (6.9)$$

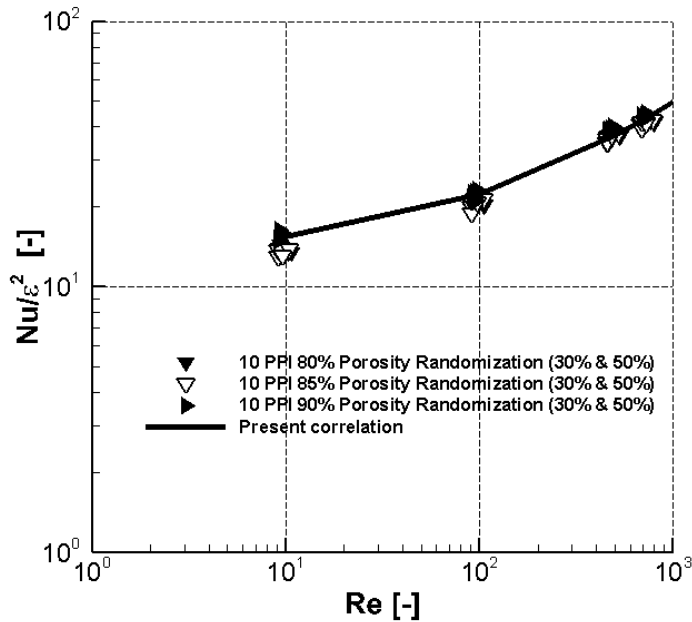
Nu_{sim} denotes the simulated Nusselt number with simulated HTC results, and Nu_{calc} represents the computed values using correlation Eq. (6.7).

6.4.3 Comparison of the proposed correlation with DPLS results.

Figure 6.11 (a & b) illustrates the relationship between the Nusselt number and Reynolds number of the ideal and randomized Kelvin structure of various porosities and pore densities with Eq. (6.7). From Figure 6.11a, It is noticed that irrespective of porosity and pore density, all data falls along one line. The RMSD between the DPLS results ($Pr = 0.7$) and the present correlation (Eq. 6.7) is noted as 4.55%. Although the structures are randomized as shown in Figure 6.11b, irrespective of scale factor, randomization and centroid factor, the DPLS data well fitted with the present study correlation and have an RMSD of 6.75%. In Figure 6.12, the DPLS Nusselt numbers data of different working fluids ($Pr = 2$ and 6) is compared against the present study correlation with Eq. (6.7). Because of scattered results, the arithmetic regression analysis is performed and found an RMSD of $\pm 15\%$ (goodness of fit found $R^2 = 0.97$). Thus it is confirmed that, whatever the porous structure (Ideal or Randomized) and working fluid (air or water or saltwater), the proposed correlation agrees well with the DPLS results. Figure 6.11a, the ideal structure's simulation results of 10, 20 & 30 PPI precisely followed the Nusselt number relation without any deviation. Hence, in the randomized case, the simulations are conducted only for 10 PPIs to investigate the effect of randomization. Figure 6.13 (a-c) presents the comparative results of the HTC in between DPLS and Eq. (6.7). It is seen that the calculated HTC values with Eq. (6.7) match well with the DPLS HTC results of all the working fluids used in this study.



(a)



(b)

Figure 6.11: Comparison of Nusselt number DPLS data with current study correlation (Eq. 6.7) at various porosities and PPI. (a) Ideal structure (b) Randomized structure ($Pr = 0.7$)

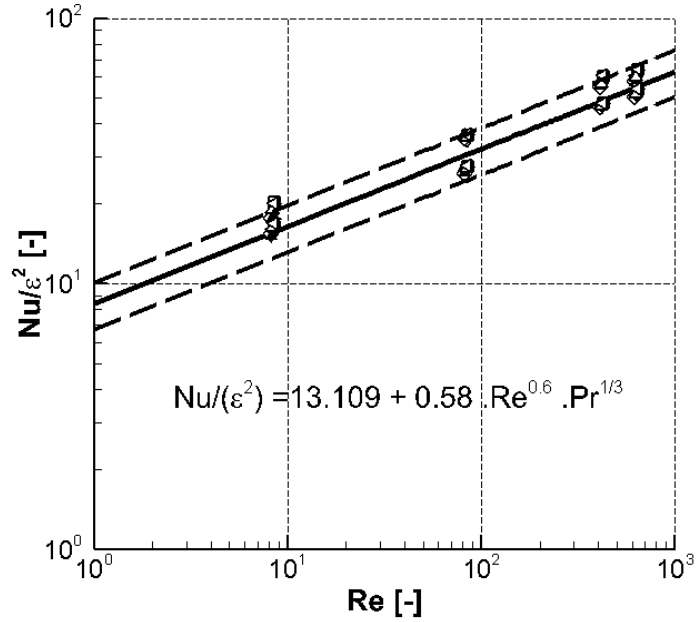
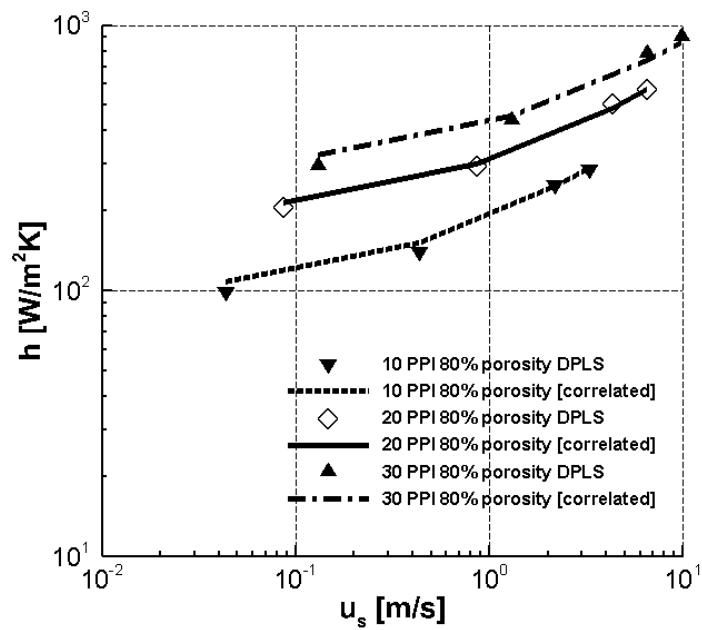


Figure 6.12: Nusselt number comparison with present work correlation at different working fluids ($Pr = 2$, and 6) dashed lines indicates $\pm 15\%$ error band



(a)

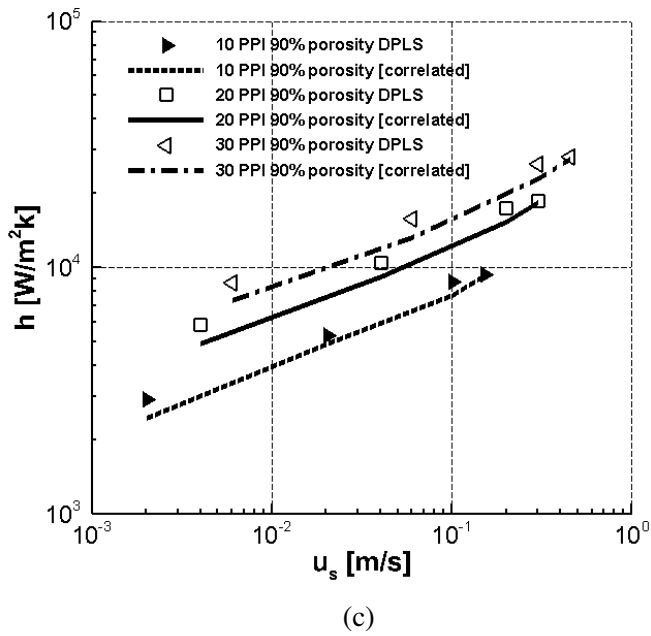
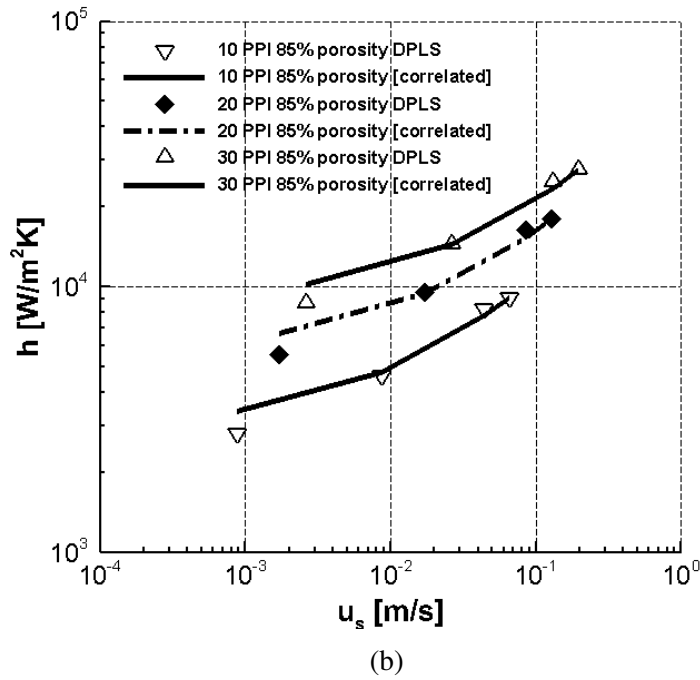


Figure 6.13: Comparison of HTC results between DPLS and Eq. (6.7) for different working fluids (a) Air $Pr = 0.7$, (b) salt water $Pr = 2$ and (c) Water $Pr = 6$

6.4.4 Comparison of the proposed correlation with available experiments in the literature.

Figure 6.14 (metal foams) presents a comparison of HTC between those calculated using Eq. (6.7) and those determined by Mancin *et al.* (2013) experiments. The proposed correlation shows a good agreement with experimental values, and it is noticed that around 85% of HTC values in Eq. (6.7) fall within 15% error margin. In Figure 6.15 (for ceramic foams), the HTC between values calculated using Eq. (6.7) and experimental values of Dietrich (2013) and Kamath *et al.* (2013) are explored. For high porosity and PPI, it can be seen that the developed correlation is consistent with experimental results. In Figure 6.15, from the experimental results of Dietrich (2013), it has been noticed that 77% of HTC with Eq. (6.7) lie within the relative error of 29%. In Figure 6.15, it can also be observed that the calculated HTC of 45 PPI foam has a maximum deviation in comparison with the experimental values. The reason behind that 45 PPI foam has more closed pores compared to other foams that are reported by Dietrich (2013).

In Figure 6.16, the numerical (Diani *et al.* 2015 & Ambrosio *et al.* 2016) and experimental (Mancin *et al.* 2013) HTC results of copper metal foams at 40 PPI with 94% porosity are plotted against the present correlation Eq. (6.7). It is clear that the proposed correlation Eq. (6.7) successfully predicts the HTC in open-cell foams. In Figure 6.17, the calculated HTCs with Eq. (6.7) is compared with experimental and numerical results of real porous structures at different porosities, PPI and materials. It is observed that irrespective of material, and geometrical parameters the proposed correlation fits well with literature data.

Figure 6.18 shows the plot of Nusselt number versus Reynolds number data as a validation of the present correlation. It is seen that, over a broad range of Reynolds numbers, all literature values follow the proposed correlation (Eq. 6.7) within the RMSD of $\pm 40\%$. The RMSD error-checked with different authors data reported in Table 6.1.

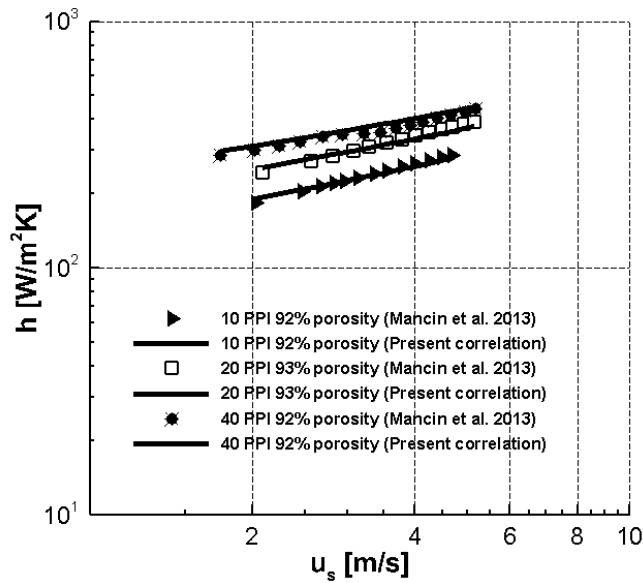


Figure 6.14: Comparison of HTC values computed using Eq. (6.7) against experimental outcomes of real porous structures (10, 20, 30 and 40 PPI Al_2O_3 metal foams with total porosities 0.926, 0.93 and 0.926, respectively).

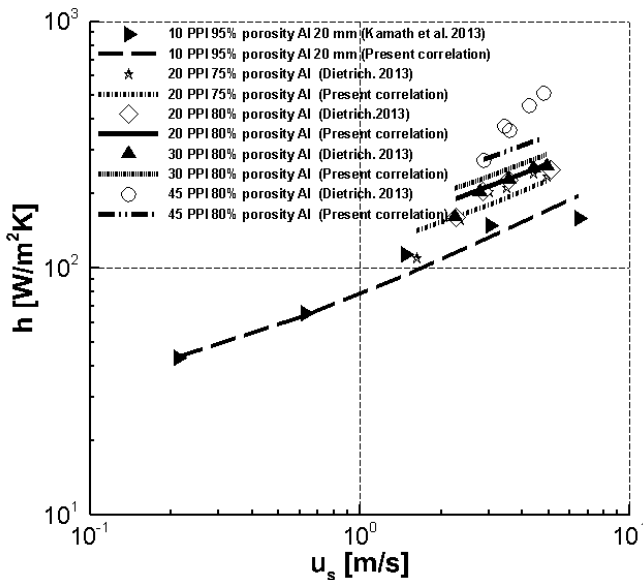


Figure 6.15: Comparison of HTC values computed using Eq. (6.7) against experimental outcomes of real porous structures (10, 20, 30 and 40 PPI Al_2O_3 metal & ceramic foams with different porosities, respectively).

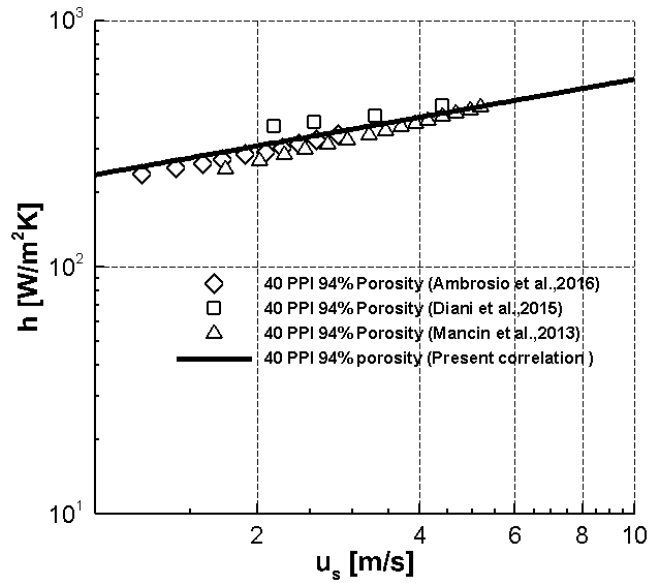


Figure 6.16: Comparison of HTC values computed using Eq. (6.7) against experimental & numerical outcomes of real porous structures at 40 PPI & 94% porosity (Cu metal foams)

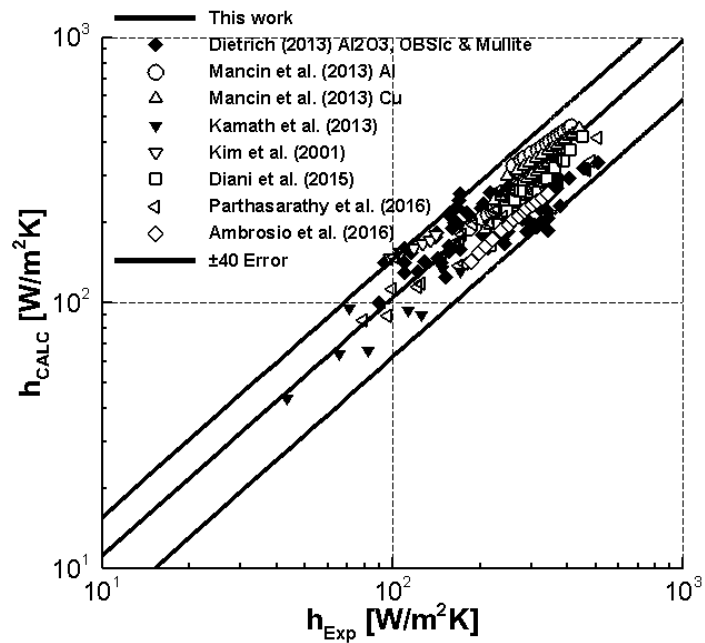


Figure 6.17: Comparison of experimental HTC results with calculated HTC using Eq. (6.7).

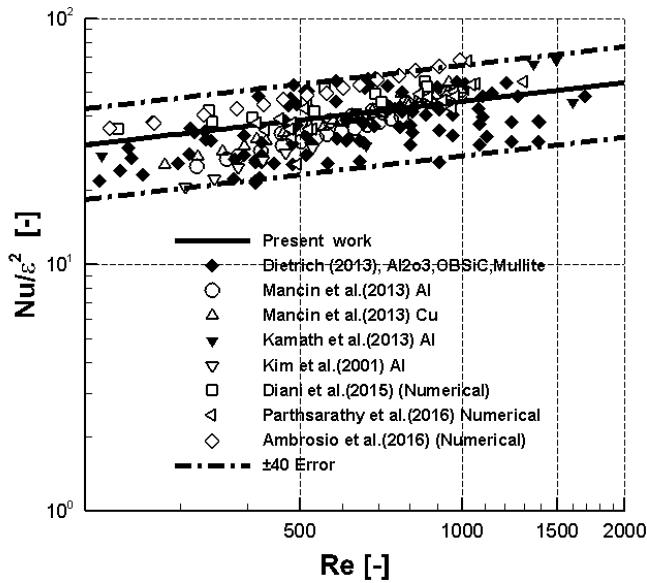


Figure 6.18: Validation of the present work correlation.

It seems that all the data, irrespective of porosity, PPI and material, error having a range of $\pm 40\%$. So, for open-cell foams, due to their complexity in foam morphology and manufacturing difficulty reproducing same structures, error within 38% will be admissible (Goedecke 2011). So, in this comparison, the maximum error noticed that 38% (see Table 6.1). Based on this, it can be concluded that the correlation obtained for the Kelvin structure (ideal) is equally adequate for real porous structures (non-ideal) within an appropriate range of $10 < Re < 1000$ at greater porosities (75% to 95%).

6.4.5 Heat transfer correlation based on Hg

Previously, the simulation data is correlated with a Nusselt–Reynolds approach as it is usually done for heat transfer data. In addition to heat transfer data described above, pressure drop data of the same structures are also necessary. Furthermore, the applicability of the analogy between heat and momentum transfer – Similarly, in the same way, a Nusselt–Hagen correlation (Eq. 6.10) has been developed allowing easy and accurate estimation of heat transfer coefficients for any sponges from the pressure

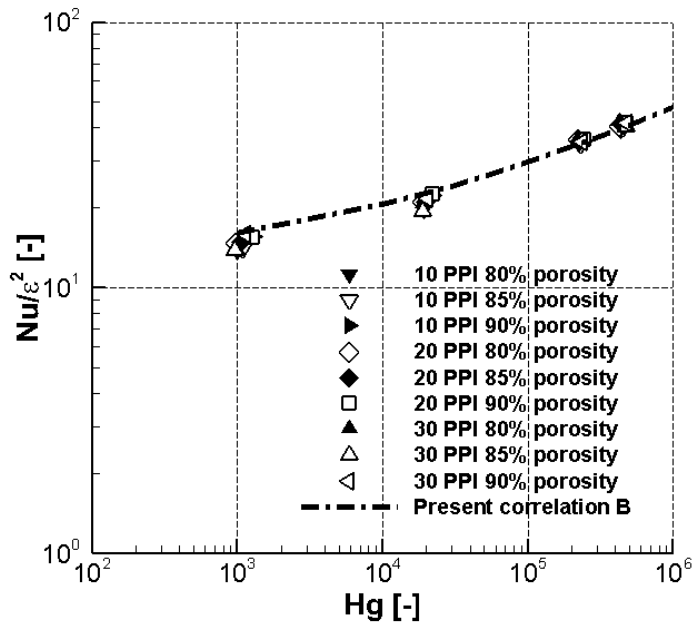
drop data.

$$Nu = \frac{h \cdot d_h}{k_f} = 11.38\varepsilon^2 + 0.58\varepsilon^2 Hg^{0.3} Pr^{1/3} \quad (6.10)$$

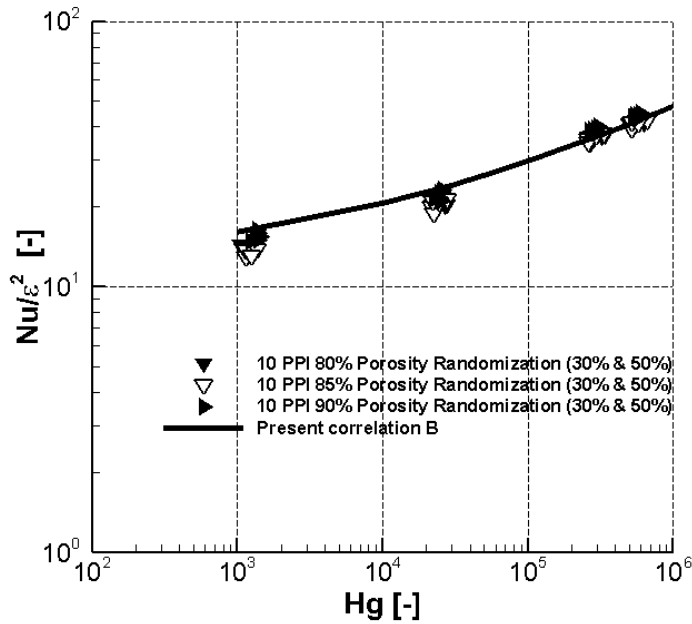
Figure 6.19 (a & b) shows the DPLS results of the Hagen number (Hg) (corresponds to dimensionless pressure drop), the Prandtl number (Pr) and the Nusselt number (Nu) (corresponds to dimensionless heat transfer coefficient) of the ideal and randomized Kelvin structures of various porosities and pore densities with help of Eq. (6.10). From Figure 6.19a, it is observed that irrespective of PPI and porosities, all the data fall on a single line. The RMSD between the DPLS results (Pr=0.7) and the present correlation (Eq. 6.10) is noted as 7.55%. Which is 3% higher than the previous heat transfer correlation (Eq. 6.7). Even if the structures are randomized as shown in Figure (6.19b), regardless of randomization, scale factor and centroid factor the DPLS data well fitted with present correlation (Eq. 6.10) and have an RMSD of 9.77%. In Figure (6.20), different working fluids (Pr = 2 and 6) are compared with the DPLS Nusselt numbers with the present study correlation (Eq. 6.10). Due to scattered results, arithmetic regression is conducted and found an RMSD of $\pm 15\%$ (goodness of fit found $R^2 = 0.97$). Therefore, the proposed correlation agrees well with the DPLS values, regardless of porous structure (ideal or random) and fluid type (air, water, saltwater). The main aim of this proposed correlation is easy estimation of heat transfer coefficients of yet unknown sponges due to the comparatively easy determination of pressure drop data. For validating the present work correlation, the correlation is compared with different experimental data that are available in the literature and plotted in Figure (6.21). It can be viewed that the proposed correlation Eq. (6.10) is well fitted with experimental results within a RMSD of $\pm 40\%$. Here, the pressure drop data of reported authors are estimated using the pressure drop correlation proposed by this study Eq. (4.10) in chapter 4.

6.4.6 Comparison of Heat transfer correlations

In Table 6.1, both the correlation's (Eq. 6.7 and Eq. 6.10) RMSD-errors are compared against the experimental data. It is observed that irrespective of the material,



(a)



(b)

Figure 6.19: Comparison of Nusselt number DPLS data with current study correlation B (Eq. 6.10) at various porosities and PPI. (a) Ideal structure (b) Randomized structure (Pr =0.7)

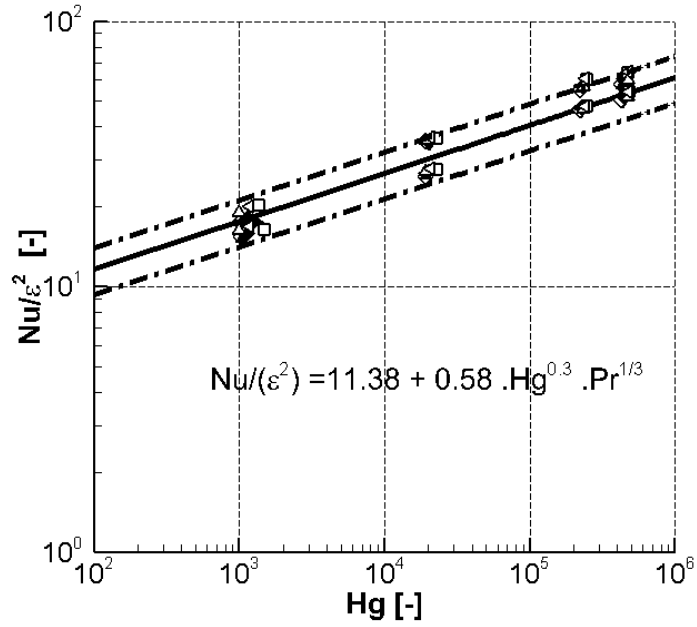


Figure 6.20: Nusselt number comparison with present work correlation at different working fluids (Pr =2, and 6) dashed lines indicates $\pm 15\%$ error band

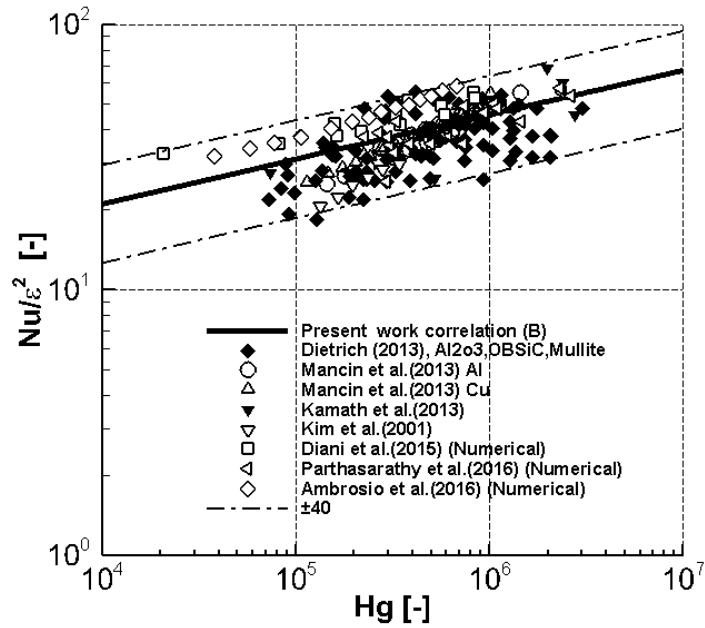


Figure 6.21: Validation of the present work correlation.

geometrical properties and working fluid, all the experimental values, follows the correlation A (i.e. Eq. 6.7) and correlation B (Eq. 6.10) within a RMSD of $\pm 40\%$. It is also noticed that, while comparing both the correlations (A&B), the error difference seems is very low ($< 1\%$) i.e. all most negligible. Therefore, both the correlations are suitable for determine the heat transfer coefficient. However, a peculiar advantage of correlation B is that easy to estimate heat transfer coefficients with only pressure drop data.

Table 6.1: Comparison of Nusselt number RMSD values with numerical and experimental investigations in the literature

Author	Material	PPI	Porosity	Re	RMSD (correlation A)	RMSD (correlation B)	Error Difference
Mancin <i>et al.</i> (2013) (Experimental)	Alumina	10	0.926	400-1600	10.41%	10.49%	0.08%
		20	0.93				
		40	0.926				
	Cu	10	0.934				
		20	0.935				
		40	0.936				
Diani <i>et al.</i> (2015) (Numerical)	Cu	10	0.934	400-1600	15.32%	15.90%	0.58%
		20	0.935				
		40	0.936				
Parthasarathy <i>et al.</i> (2016) (DPLS)	Alumina	10	0.82	400-1500	21%	21.10%	0.53%
		20	0.769				
		30	0.82				
		45	0.845				
	SiC	10	0.744				
		20	0.822				
		30	0.847				
		45	0.791				
Ambrosio <i>et al.</i> (2016) (Numerical)	Alumina	10	0.872	400-1500	11%	11%	0%
		20	0.875				
Dietrich (2013) (Experimental)	Al ₂ O ₃	40	0.94	400-2000	28.64%	27.68%	0.96%
		10	80				
		20	75				
		30	85				
		45	80				
	OBSiC	20	80	200-1000	37.60%	38.10%	0.50%
		30	80				
		40	80				
		20	75				
		20	85				
Mullite	20	75	200-1000	34.90%	35.70%	0.80%	
	20	85					
	20	85					
Kamath <i>et al.</i> (2013) (Experimental)	Alumina	10	0.9481	200-1600	30.99%	31.12%	0.13%
		10	0.9417				
		10	0.9449				
Kim <i>et al.</i> (2001) (Experimental)	Alumina	10	0.92	80-500	38.04%	37.46%	0.58%
		20	0.92				
		40	0.92				

6.5 Conclusion

In this chapter, a numerical study on the heat transfer coefficients of reticulated Kelvin structures has been carried out using the steady-state method. The geometries for this analysis were used the same as that of the pressure drop study of porosities 80%, 85%, and 90% and 10, 20, and 30 PPI. Simulations were conducted using these grids with the assistance of commercial CFD software (ANSYS-CFX). The simulations were carried out for different working fluids, air ($Pr = 0.7$), saltwater ($Pr = 2$) and water ($Pr = 6$) for various Reynolds numbers 10, 100, 500 and 750. The fluid inlet temperature was maintained lower than strut temperature to investigate the heat transfer. Parametric studies were carried with varying porosities, pore densities and velocities. Based on the present investigation, the salient points are summarized below:

1. The VHTC increased with increasing PPI and velocity, i.e., a higher PPI foam has shown higher heat transfer performance because of greater specific surface area.
2. For the same PPI, the VHTC decreased with increasing porosity. This is mainly due to the reduction in the strut diameter and it leads reduction in the specific surface area while the porosity increases.
3. The randomized structure showed higher heat transfer than the ideal structure even if maintained the same PPI and specific surface area.
4. Based on simulation results, the $Nu-Re$ and $Nu-Hg$ correlations were proposed and it was compared with existing results of numerical and experimental data.
5. Over a broad range of Reynolds numbers, all literature values follow the proposed correlations (Eq. 6.7) and (Eq. 6.10) within the RMSD of $\pm 40\%$.
6. Based on this, it can be concluded that the correlation obtained for the Kelvin structure was equally adequate for real porous structures within an appropriate range of $10 < Re < 1000$ at greater porosities (75% to 95%).

Therefore, the proposed correlations were suitable for to design of any work related

to open-cell foam, especially in thermal management applications.

6.6 Closure

This chapter described the detailed procedure for calculating the heat transfer coefficient. Two different correlations were proposed to predict the heat transfer in various open-cell foams. The proposed correlations could predict the heat transfer coefficient within the permissible error.

CHAPTER 7

CONCLUSION AND FUTURE SCOPE

The main aim of this research work was to determine the fluid flow and heat transfer properties of the open-cell reticulated structures and to express them in terms of the known morphological parameters of the foams. The reticulated porous structures were modeled after the Kelvin structure. The 3D foam geometries for the analysis were constructed using an in-house code along with the use of visualization tool kit (VTK) libraries. The ideal and randomized Kelvin structures geometries with different porosities (80%, 85%, and 90%) and pore densities (10, 20, and 30 PPI) were generated. The geometry data of each structure was imported to a commercial grid generating software (ICEM CFD) to obtain the computational grids. These grid geometries had been used to perform direct pore level simulations (DPLS) with the aid of commercial CFD software (ANSYS CFX). For each of the structures, the simulations were performed for four different Reynolds numbers, i.e., Re 10, 100, 500, and 750.

In order to better observe the trends in pressure drop, direct pore level simulations were performed (DPLS) in the ideal and randomized Kelvin structures. The DPLS analysis were carried out for Reynolds numbers 10, 100, 500 and 750 (within the laminar range), where the air was used as working fluid. The Reynolds numbers ($Re = \rho d_h u_s / \varepsilon \mu$) are calculated using the hydraulic diameter ($d_h = 4\varepsilon / S_v$) as the characteristics length. From the simulation results, the Hagen number and Reynolds number relation fall on a seconder order polynomial line and contribute to finding new viscous and inertial coefficient values for the relation. These values were independent of the geometrical properties (PPI, specific surface area, and porosity) of the porous structures. Thus the correlation was proposed for calculating pressure drop in open-cell foams.

$$\frac{dp}{dx} = 130.29 \cdot \frac{\mu}{\varepsilon d_h^2} u_s + 0.99 \cdot \frac{\rho}{\varepsilon^2 d_h} u_s^2; Hg = 130.29 \cdot Re + 0.99 \cdot Re^2$$

The applicability of this correlation for real structures and for a range of porosities and pore densities was examined by comparing it with DPLS results of real structures. The RMSD of the present correlation is found to be 5.7% which is less than the RMSD of 17.64% for the correlation provided by authors in literature. Furthermore, the correlation is validated by comparing it with existing experimental results of different structures made up of ceramic and metallic materials at different flow conditions and for different fluids. It is concluded that the proposed correlation would predict the pressure drop in open-cell foams, and in most cases, the predictions had a mean relative error value less than 15%.

In the next step of this present work, DPLS were performed to characterize the longitudinal dispersion coefficients (LDC) in ideal and randomized Kelvin structures. Using the conventional Navier-Stokes equations, airflow had been determined through various porous structures. Along with the flow, the dispersion of the tracer was traced across the structures and analysed in terms of the effective diffusivity coefficient. To evaluate the LDC, the analytic solution gradients were fitted into the simulated gradients. Further, to study the effect of tortuosity on LDC, the tortuosity values were calculated for each and every structure. The Lagrangian particle tracking (LPT) method was used to track the particle in the Eulerian fluid phase flow, i.e., individual particles were tracked from the inlet to the outlet of the domain. In order to represent the Pe_L of the Kelvin structure with that of the packed bed, a modified characteristic length correlation was proposed as a function of strut dia and flow tortuosity.

$$d = d_s(-5.2 + 6.7\tau)$$

With the correlated characteristic length scale, the Pe_L of the ideal and randomized Kelvin structures are nearly equal to the packed bed data that are reported in the literature.

Finally, in this study, heat transfer coefficients (HTC) were calculated for ideal and

randomized Kelvin structures. The simulations were carried out for different working fluids, air (Pr = 0.7), saltwater (Pr = 2) and water (Pr = 6) for various Reynolds numbers 10, 100, 500 and 750. From the simulation results, the Nusselt number results show strong dependency on the porosity. Based on this, a new correlation (Nu-Re) was proposed to estimate the HTC in open-cell foams. Further, to show that convective heat transfer is a function of pressure drop, a correlation for the non-dimensional form of Nusselt in terms of Hagen number was also proposed.

$$Nu = \frac{h \cdot d_h}{k_f} = 13.109\varepsilon^2 + 0.58\varepsilon^2 Re^{0.6} Pr^{1/3}$$

$$Nu = \frac{h \cdot d_h}{k_f} = 11.38\varepsilon^2 + 0.58\varepsilon^2 Hg^{0.3} Pr^{1/3}$$

However, the main advantage of the Nu-Hg correlation was that it is easy to estimate heat transfer coefficients with only pressure drop data. The predicted HTC values are compared with different experimental results, and it is found most of the values fall within relative error of 15%. Moreover, the proposed correlations were validated by comparing them with existing numerical and experimental data of various materials and working fluids. Regardless of materials and working fluids, the proposed correlation is able to predict HTC in reticulated porous structures within an acceptable RMSD of $\pm 40\%$.

7.1 Future Scope

In the present numerical simulations, the analysis was performed up to the flow rate of $Re < 1000$ and thermal dispersion effects were neglected. The study can be extended by examining the turbulent regime at higher flow rates, and it provides an excellent opportunity to investigate flow behaviour and how its hydraulic parameters are affected in this regime. The study could be extended to examine the effect of thermal conductivity (various materials) and other thermal parameters (thermal dispersion) influence on reticulated structures. The relation between the tortuosity and geometrical parameters was not well correlated. It would be interesting to measure tortuosity with different

geometrical parameters. Continuing from the earlier recommendation, it would be very helpful to have a relation between geometric parameters like pore diameter, porosity, specific surface area, domain length, or any combination of these. Another promising possibility is to increase the specific surface area by modifying the circular strut shape with equilateral triangular, square, diamond, hexagon and star shapes etc.. In this study, the proposed correlations were validated with other experimental results. Future work could focus on conducting experiments, due to the availability of additive manufacturing systems, it is possible to manufacture experimental samples using 3D printing. Further, the study could be extended to study the applicability of proposed correlations in various engineering applications (where porous media are used) such as porous combustors, emission, radiant porous burners and volumetric solar reactors using the volume-averaging model.

7.2 Closure

Finally, the overall conclusion of the present research work was summarized in this chapter. The future scope and extension possibilities of the current work are also reported at the end of this chapter.

APPENDIX I

Numerical results of pressure drop

Table I.1: Pressure drop results of ideal structures.

Structure name	Velocity [m/s]	Pressure drop [Pa/m]
IDEAL 10 PPI 80% porosity	0.0435	22.04
	0.4349	426.97
	2.1746	4946.00
	3.2619	9586.87
IDEAL 10 PPI 85% porosity	0.0406	15.93
	0.4056	292.44
	2.0282	3355.97
	3.0424	6545.39
IDEAL 10 PPI 90% porosity	0.0353	9.76
	0.3535	167.49
	1.7675	1831.21
	2.6512	3562.53
IDEAL 20 PPI 80% porosity	0.0866	174.20
	0.8659	3359.60
	4.3293	39155.00
	6.4940	76012.00
IDEAL 20 PPI 85% porosity	0.0794	119.38
	0.7943	2215.90
	4.0100	25453.00
	6.0200	49696.00
IDEAL 20 PPI 90% porosity	0.0703	74.81
	0.7028	1301.60
	3.5141	14308.00
	5.2712	27883.00
IDEAL 30 PPI 80% porosity	0.1302	599.73
	1.3016	11535
	6.5078	134072
	9.7617	257045
IDEAL 30 PPI 85% porosity	0.1219	377.3

	1.2190	7364.3
	6.0957	91445
	9.1443	184859
	0.1053	227.90
IDEAL 30 PPI 90% porosity	1.0533	4118.30
	5.2664	48008.00
	7.8996	95885.00

Table I.2: Pressure drop and specific surface area results of Randomized structures (10 PPI 80% porosity).

Structure name	S_v (m^{-1})	Velocity [m/s]	Pressure drop [Pa/m]
30_65_30	1392.29	0.0506	25.69
		0.5061	542.35
		2.5305	6692.60
		3.7957	13102.00
30_65_40	1407.21	0.0494	27.95
		0.4937	562.55
		2.4683	6675.08
		3.7025	12972.48
30_75_30	1406.61	0.0504	27.96
		0.5040	572.02
		2.5201	6841.59
		3.7801	13294.60
30_75_40	1424.64	0.0504	29.40
		0.5042	587.91
		2.5207	6937.73
		3.7812	13452.28
50_65_30	1414.86	0.0586	33.90
		0.5862	721.50
		2.9308	8702.36
		4.3962	17074.15
50_65_40	1428.65	0.0583	33.48
		0.5831	712.85
		2.9153	8648.30
		4.3729	16968.92
50_75_30	1414.46	0.0559	29.96
		0.5591	647.36
		2.7957	7898.91

		4.1935	15449.61
50_75_40	1438.20	0.0531	31.10
		0.5306	631.48
		2.6534	7550.23
		3.9801	14622.76
70_65_30	1425.53	0.0580	33.69
		0.5802	715.46
		2.9014	8565.09
		4.3520	16758.81
70_65_40	1428.65	0.0564	33.07
		0.5636	689.74
		2.8180	8185.38
		4.2269	16079.70
70_75_30	1436.48	0.0587	34.45
		0.5865	744.52
		2.9325	8975.03
		4.3988	17589.48
70_75_40	1447.23	0.0540	30.96
		0.5404	650.46
		2.7020	7821.39
		4.0531	15333.12

Table I.3: Pressure drop and specific surface area results of Randomized structures (10 PPI 85% porosity).

Structure name	S_v (m^{-1})	Velocity [m/s]	Pressure drop [Pa/m]
30_65_30	1271.71	0.0460	18.32
		0.4603	354.50
		2.3015	4223.26
		3.4522	8270.30
30_65_40	1299.49	0.0476	18.85
		0.4765	367.75
		2.3826	4438.60
		3.5740	8764.70
30_75_30	1281.12	0.0472	19.26
		0.4716	373.66
		2.3581	4451.68

		3.5372	8716.84
30_75_40	1283.15	0.0450	18.08
		0.4506	342.90
		2.2530	4066.80
		3.3795	7946.27
50_65_30	1302.16	0.0458	18.83
		0.4584	363.47
		2.2918	4312.74
		3.4377	8438.91
50_65_40	1302.13	0.0458	18.83
		0.4584	363.48
		2.2919	4312.72
		3.4377	8438.69
50_75_30	1290.57	0.0522	21.60
		0.5223	437.87
		2.6114	5294.42
		3.9171	10416.14
50_75_40	1312.03	0.0490	20.81
		0.4901	410.37
		2.4506	4895.46
		3.6759	9594.06
70_65_30	1302.16	0.0494	18.92
		0.4946	387.71
		2.4731	4875.25
		3.7096	9625.40
70_65_40	1328.94	0.0539	21.57
		0.5389	445.72
		2.6943	5550.87
		4.0415	10993.53
70_75_30	1295.55	0.0512	21.37
		0.5116	435.85
		2.5580	5239.96
		3.8369	10285.02
70_75_40	1327.63	0.0496	21.45
		0.4966	428.12
		2.4830	5144.10
		3.7244	10096.21

Table I.4: Pressure drop and specific surface area results of Randomized structures (10 PPI 90% porosity).

Structure name	S_v (m^{-1})	Velocity [m/s]	Pressure drop [Pa/m]
30_65_30	1109.36	0.039	10.46
		0.393	191.14
		1.967	2264.88
		2.950	4457.24
30_65_40	1123.78	0.040	11.78
		0.395	210.81
		1.977	2439.42
		2.966	4769.60
30_75_30	1108.94	0.039	11.83
		0.394	209.69
		1.969	2389.17
		2.953	4663.63
30_75_40	1123.91	0.041	12.74
		0.414	226.98
		2.068	2610.52
		3.102	5115.12
50_65_30	1110.94	0.041	11.73
		0.407	216.01
		2.036	2507.86
		3.054	4910.00
50_65_40	1125.37	0.042	12.39
		0.418	228.76
		2.088	2667.90
		3.133	5227.31
50_75_30	1119.88	0.042	12.26
		0.420	227.93
		2.101	2674.68
		3.152	5254.34
50_75_40	1138.33	0.041	12.58
		0.406	226.41
		2.029	2598.31

		3.044	5077.05
70_65_30	1134.30	0.043	12.50
		0.430	232.83
		2.152	2701.49
		3.228	5289.83
70_65_40	1136.53	0.044	11.41
		0.441	219.51
		2.205	2694.08
		3.307	5340.96
70_75_30	1126.45	0.042	12.54
		0.418	232.27
		2.090	2681.25
		3.136	5242.60
70_75_40	1139.17	0.042	13.07
		0.424	239.97
		2.121	2771.01
		3.182	5421.71

APPENDIX II

Numerical results of dispersion coefficient

Table II.1: Longitudinal dispersion coefficient values of ideal structures.

Structure name	Velocity [m/s]	LDC [m^2/s]
IDEAL 10 PPI 80% porosity	0.0435	1.462E-05
	0.4349	1.787E-04
	2.1746	1.812E-03
	3.2619	2.790E-03
IDEAL 10 PPI 85% porosity	0.0406	1.454E-05
	0.4056	1.360E-04
	2.0282	1.356E-03
	3.0424	2.243E-03
IDEAL 10 PPI 90% porosity	0.0353	1.458E-05
	0.3535	1.126E-04
	1.7675	8.979E-04
	2.6512	1.255E-03
IDEAL 20 PPI 80% porosity	0.0866	1.477E-05
	0.8659	1.864E-04
	4.3293	1.715E-03
	6.4940	2.652E-03
IDEAL 20 PPI 85% porosity	0.0794	1.480E-05
	0.7943	1.290E-04
	4.0100	1.238E-03
	6.0200	2.194E-03
IDEAL 20 PPI 90% porosity	0.0703	1.483E-05
	0.7028	9.287E-05
	3.5141	7.570E-04
	5.2712	1.142E-03
IDEAL 30 PPI 80% porosity	0.1302	1.495E-05
	1.3016	1.866E-04
	6.5078	1.740E-03
	9.7617	2.794E-03

IDEAL 30 PPI 85% porosity	0.1219	1.509E-05
	1.2190	1.171E-04
	6.0957	9.753E-04
	9.1443	2.143E-03
IDEAL 30 PPI 90% porosity	0.1053	1.450E-05
	1.0533	6.908E-05
	5.2664	6.247E-04
	7.8996	1.000E-03

Table II.2: Longitudinal dispersion coefficient values of Randomized structure (10 PPI 80% porosity).

Structure	Velocity	LDC [m^2/s]
name	[m/s]	
30_65_30	0.050607	2.517E-05
	0.506068	2.689E-04
	2.530489	1.622E-03
	3.795734	2.527E-03
30_75_40	0.050446	2.367E-05
	0.504175	2.579E-04
	2.52073	1.857E-03
	3.781168	2.525E-03
50_65_30	0.058584	2.929E-05
	0.586172	3.549E-04
	2.930776	2.104E-03
	4.396206	2.999E-03
50_75_40	0.053064	2.993E-05
	0.530641	3.598E-04
	2.653356	2.755E-03
	3.980108	3.153E-03

Table II.3: Longitudinal dispersion coefficient values of Randomized structure (10 PPI 85% porosity).

Structure	Velocity	LDC [m^2/s]
name	[m/s]	
30_65_30	0.04599	1.854E-05
	0.460294	1.564E-04

	2.301468	1.487E-03
	3.452163	2.250E-03
30_75_40	0.045033	2.015E-05
	0.450636	1.655E-04
	2.253026	1.562E-03
	3.379539	2.315E-03
50_65_30	0.045807	2.367E-05
	0.458375	2.579E-04
	2.291797	1.622E-03
	3.437734	2.525E-03
50_75_40	0.049034	2.564E-05
	0.490091	2.771E-04
	2.450619	1.717E-03
	3.675887	2.625E-03

Table II.4: Longitudinal dispersion coefficient values of Randomized structure (10 PPI 90% porosity).

Structure	Velocity	LDC[m^2/s]
name	[m/s]	
30_65_30	0.039338	1.546E-05
	0.393382	1.244E-04
	1.96683	1.099E-03
	2.950286	1.357E-03
30_75_40	0.041351	1.743E-05
	0.413597	1.602E-04
	2.067814	1.115E-03
	3.101764	1.540E-03
50_65_30	0.040745	2.067E-05
	0.407192	2.479E-04
	2.03613	1.522E-03
	3.054238	2.251E-03
50_75_40	0.040591	2.125E-05
	0.405828	2.541E-04
	2.029058	1.752E-03
	3.043587	2.378E-03

APPENDIX III

Numerical results of heat transfer coefficients

Table III.1: Heat transfer coefficient values of ideal structures (fluid of $Pr = 0.7$).

Structure name	Velocity [m/s]	HTC (W/m^2K)
IDEAL 10 PPI 80% porosity	0.0435	98.78
	0.4349	140.65
	2.1746	251.16
	3.2619	286.38
IDEAL 10 PPI 85% porosity	0.0406	97.00
	0.4056	142.97
	2.0282	241.83
	3.0424	278.17
IDEAL 10 PPI 90% porosity	0.0353	97.42
	0.3535	138.75
	1.7675	224.56
	2.6512	259.19
IDEAL 20 PPI 80% porosity	0.0866	207.35
	0.8659	296.01
	4.3293	509.01
	6.4940	574.45
IDEAL 20 PPI 85% porosity	0.0794	202.78
	0.7943	286.93
	4.0100	486.08
	6.0200	555.94
IDEAL 20 PPI 90% porosity	0.0703	191.83
	0.7028	279.64
	3.5141	447.11
	5.2712	520.20
IDEAL 30 PPI 80% porosity	0.1302	295.73
	1.3016	439.56
	6.5078	782.74
	9.7617	903.45
IDEAL 30 PPI 85% porosity	0.1219	287.09
	1.2190	404.39

	6.0957	626.83
	9.1443	695.35
	0.1053	297.90
IDEAL 30 PPI 90% porosity	1.0533	403.06
	5.2664	569.81
	7.8996	622.00

Table III.2: Heat transfer coefficient values of ideal structures (fluid of $Pr = 2$).

Structure name	Velocity [m/s]	HTC (W/m^2K)
	0.0009	2798.40
	0.0093	4797.35
IDEAL 10 PPI 80% porosity	0.0467	8445.01
	0.0701	9257.43
	0.0019	5595.06
	0.0186	9464.61
IDEAL 10 PPI 85% porosity	0.0930	16832.94
	0.1396	18419.19
	0.0028	8222.12
	0.0280	14320.79
IDEAL 10 PPI 90% porosity	0.1399	26050.67
	0.2098	28950.57
	0.0009	2785.83
	0.0087	4634.69
IDEAL 20 PPI 80% porosity	0.0436	8231.84
	0.0654	9105.93
	0.0017	5543.22
	0.0173	9524.61
IDEAL 20 PPI 85% porosity	0.0864	16355.66
	0.1296	18117.10
	0.0026	8663.68
	0.0262	14440.19
IDEAL 20 PPI 90% porosity	0.1310	24901.16
	0.1965	27649.77
	0.0008	2800.84
	0.0076	4417.76
IDEAL 30 PPI 80% porosity	0.0380	7713.03
	0.0570	8678.91
	0.0015	5251.38
IDEAL 30 PPI 85% porosity		

	0.0151	8798.97
	0.0755	15323.45
	0.1133	17303.35
	0.0023	8078.81
IDEAL 30 PPI 90% porosity	0.0226	13419.84
	0.1132	23033.56
	0.1698	26035.03

Table III.3: Heat transfer coefficient values of ideal structures (fluid of $Pr = 6$).

Structure name	Velocity [m/s]	HTC (W/m^2K)
	0.0025	2916.43
IDEAL 10 PPI 80% porosity	0.0250	5814.51
	0.1252	9155.98
	0.1879	9592.42
	0.0050	5810.78
IDEAL 10 PPI 85% porosity	0.0499	11626.75
	0.2493	18123.59
	0.3740	19059.14
	0.0075	8648.98
IDEAL 10 PPI 90% porosity	0.0750	17797.29
	0.3748	27503.00
	0.5622	28378.62
	0.0023	2905.05
IDEAL 20 PPI 80% porosity	0.0235	5621.03
	0.1168	9028.76
	0.1752	9497.92
	0.0046	5781.50
IDEAL 20 PPI 85% porosity	0.0463	11127.50
	0.2315	17979.53
	0.3473	18922.52
	0.0070	9140.93
IDEAL 20 PPI 90% porosity	0.0702	17227.13
	0.3511	27443.06
	0.5267	28950.77
	0.0020	2922.24
IDEAL 30 PPI 80% porosity	0.0204	5282.04
	0.1018	8711.66
	0.1527	9318.09

	0.0040	5825.42
	0.0405	10435.12
IDEAL 30 PPI 85% porosity	0.2024	17408.02
	0.3036	18508.10
	0.0061	8674.41
	0.0607	15824.73
IDEAL 30 PPI 90% porosity	0.3033	26369.14
	0.4550	28033.76

Table III.4: Heat transfer coefficient values of Randomized structure of 10 PPI 80% porosity (fluid of $Pr = 0.7$).

Structure name	Velocity [m/s]	HTC (W/m^2K)
30_65_30	0.0506	70.49
	0.5061	144.61
	2.5305	263.73
	3.7957	296.98
30_65_40	0.0494	76.32
	0.4937	141.75
	2.4683	261.39
	3.7025	294.63
30_75_30	0.0504	78.06
	0.5040	152.82
	2.5201	269.01
	3.7801	301.87
30_75_40	0.0504	77.74
	0.5042	148.12
	2.5207	268.53
	3.7812	301.56
50_65_30	0.0586	62.42
	0.5862	148.58
	2.9308	270.94
	4.3962	304.68
50_65_40	0.0583	65.91
	0.5831	147.81
	2.9153	269.10
	4.3729	302.59
50_75_30	0.0559	62.56
	0.5591	151.42

	2.7957	273.76
	4.1935	306.20
50_75_40	0.0531	67.51
	0.5306	148.90
	2.6534	269.15
	3.9801	301.91

Table III.5: Heat transfer coefficient values of Randomized structure of 10 PPI 85% porosity (fluid of $Pr = 0.7$).

Structure name	Velocity [m/s]	HTC (W/m^2K)
30_65_30	0.0460	67.88
	0.4603	140.60
	2.3015	254.32
	3.4522	286.91
30_65_40	0.0476	70.00
	0.4765	143.58
	2.3826	259.68
	3.5740	292.88
30_75_30	0.0472	77.33
	0.4716	151.16
	2.3581	262.62
	3.5372	295.57
30_75_40	0.0450	71.20
	0.4506	141.77
	2.2530	255.06
	3.3795	287.03
50_65_30	0.0458	68.18
	0.4584	135.22
	2.2918	249.64
	3.4377	283.25
50_65_40	0.0458	68.18
	0.4584	150.10
	2.2919	249.65
	3.4377	299.67
50_75_30	0.0522	68.35
	0.5223	151.90
	2.6114	269.20
	3.9171	301.95

	0.0490	74.75
	0.4901	150.10
50_75_40	2.4506	267.43
	3.6759	299.67

Table III.6: Heat transfer coefficient values of Randomized structure of 10 PPI 90% porosity (fluid of $Pr = 0.7$).

Structure	Velocity	HTC
name	[m/s]	(W/m^2K)
	0.0393	79.91
	0.3934	138.47
30_65_30	1.9668	248.70
	2.9503	281.44
	0.0396	73.62
	0.3954	140.50
30_65_40	1.9770	250.03
	2.9655	282.27
	0.0394	80.74
	0.3938	145.65
30_75_30	1.9689	252.68
	2.9533	284.67
	0.0414	76.03
	0.4136	148.44
30_75_40	2.0678	256.43
	3.1018	288.45
	0.0407	75.14
	0.4072	137.60
50_65_30	2.0361	245.15
	3.0542	277.36
	0.0418	70.47
	0.4177	137.61
50_65_40	2.0884	249.88
	3.1326	282.16
	0.0420	76.58
	0.4203	150.20
50_75_30	2.1013	260.12
	3.1519	291.84
	0.0406	82.93
	0.4058	149.33
50_75_40	2.0291	255.81
	3.0436	287.58

REFERENCES

- Achenbach, E. (1995). Heat and flow characteristics of packed beds. *Experimental Thermal and Fluid Science*, 10(1), 17–27. ISSN 08941777.
- Ackermann, S., J. R. Scheffe, J. Duss, and A. Steinfeld (2014). Morphological characterization and effective thermal conductivity of dual-scale reticulated porous structures. *Materials*, 7(11), 7173–7195. ISSN 19961944.
- Afshari, S., S. H. Hejazi, and A. Kantzas (2018). Longitudinal dispersion in heterogeneous layered porous media during stable and unstable pore-scale miscible displacements. *Advances in Water Resources*, 119(April), 125–141. ISSN 03091708. URL <https://doi.org/10.1016/j.advwatres.2018.06.005>.
- Ambrosio, G., N. Bianco, W. K. Chiu, M. Iasiello, V. Naso, and M. Oliviero (2016). The effect of open-cell metal foams strut shape on convection heat transfer and pressure drop. *Applied Thermal Engineering*, 103, 333–343. ISSN 13594311.
- Antohe, B. V., J. L. Lage, D. C. Price, and R. M. Weber (1997). Experimental Determination of Permeability and Inertia Coefficients of Mechanically Compressed Aluminum Porous Matrices. *Journal of Fluids Engineering*, 119(2), 404–412. ISSN 0098-2202. URL <https://doi.org/10.1115/1.2819148>.
- Aris, R. and P. R. S. L. A (1956). On the dispersion of a solute in a fluid flowing through a tube. *Proceedings of the Royal Society of London. Series A. Mathematical and Physical Sciences*, 235(1200), 67–77. ISSN 0080-4630.
- Aris, R. and N. R. Amundson (1957). Some remarks on longitudinal mixing or diffusion in fixed beds. *AIChE J*, 3, 280–282.

Azzi, W., W. L. Roberts, and A. Rabiei (2007). A study on pressure drop and heat transfer in open cell metal foams for jet engine applications. *Materials and Design*, 28, 569–574.

Baril, B. E., A. Mostafid, L.-p. Lefebvre, and M. Medraj (2008). Experimental Demonstration of Entrance / Exit Effects on the Permeability Measurements of Porous Materials. (9), 889–894.

Bear, J., *Dynamics of Fluids in Porous Media*. Dover Publications, Inc., New York, 1988.

Bejan, B. and D. Poulikakos (1984). CONVECTION IN A POROUS MEDIUM.

Bernsdorf, J., G. Brenner, and F. Durst (2000). Numerical analysis of the pressure drop in porous media flow with lattice boltzmann (bgk) automata. *Computer Physics Communications*, 129, 247 – 255.

Bhattacharya, A., V. V. Calmidi, and R. L. Mahajan (2002). Thermophysical properties of high porosity metal foams. *International Journal of Heat and Mass Transfer*, 45, 1017–1031.

Bhattacharya, A. and R. L. Mahajan (2002). Finned Metal Foam Heat Sinks for Electronics Cooling in Forced Convection . *Journal of Electronic Packaging*, 124(3), 155–163. ISSN 1043-7398. URL <https://doi.org/10.1115/1.1464877>.

Bianchi, E., T. Heidig, C. G. Visconti, G. Groppi, H. Freund, and E. Tronconi (2013). Heat transfer properties of metal foam supports for structured catalysts: Wall heat transfer coefficient. *Catalysis Today*, 216, 121–134. ISSN 09205861. URL <http://dx.doi.org/10.1016/j.cattod.2013.06.019>.

Bird, R., *Transport phenomena*. J. Wiley, New York, 2002. ISBN 0-471-41077-2.

Boomsma, K. and D. Poulikakos (2002). The effects of compression and pore size variations on the liquid flow characteristics in metal foams. *Journal of Fluids Engineering- transactions of The Asme*, 124, 263–272.

Boomsma, K., D. Poulikakos, and Y. Ventikos (2003). Simulations of flow through open cell metal foams using an idealized periodic cell structure. *International Journal of Heat and Fluid Flow*, 24(6), 825–834.

Boon, J. P., E. V. Eijnden, and D. Hanon (2000). A lattice gas automaton approach to ‘turbulent diffusion’. *Chaos Solitons Fractals*, 11, 187.

Braconni, M., M. Ambrosetti, O. Okafor, V. Sans, X. Zhang, X. Ou, C. P. Da Fonte, X. Fan, M. Maestri, G. Groppi, and E. Tronconi (2019). Investigation of pressure drop in 3D replicated open-cell foams: Coupling CFD with experimental data on additively manufactured foams. *Chemical Engineering Journal*, 377(October 2018), 120123. ISSN 13858947. URL <https://doi.org/10.1016/j.cej.2018.10.060>.

Calmidi, V. and R. Mahajan (2000a). Forced convection in high porosity metal foams. *TRANSACTIONS-AMERICAN SOCIETY OF MECHANICAL ENGINEERS JOURNAL OF HEAT TRANSFER*, 122(3), 557–565.

Calmidi, V. V., *Transport phenomena in high porosity fibrous metal foams / by Varaprasad V. Calmidi.*. UMI, Ann Arbor, Mich., 1998.

Calmidi, V. V. and R. L. Mahajan (2000b). Forced convection in high porosity metal foams. *Journal of Heat Transfer*, 122, 557–565.

Carberry, J. J. and R. H. Bretton (1958). Axial dispersion of mass in flow through fixed beds. *AIChE J*, 4, 367–375.

Carbonell, R. G. and S. Whitaker (1983). Dispersion in pulsed systems-ii: Theoretical developments for passive dispersion in porous media. *Chemical engineering science*, 38, 1795–1802.

Chen, S. and G. D. Doole (1998). Lattice boltzmann method for fluid flows. *A. Rev. Fluid Mech*, 30, 329–364.

Coles, M., R. Hazlett, P. Spanne, W. Soll, E. Muegge, and K. Jones (1998). Pore level imaging of fluid transport using synchrotron x-ray microtomography. *Journal of Petroleum Science and Engineering*, 19, 55 – 63.

Cunsolo, S., M. Iasiello, M. Oliviero, N. Bianco, W. K. S. Chiu, and V. Naso (2015). Lord Kelvin and Weaire–Phelan Foam Models: Heat Transfer and Pressure Drop. *Journal of Heat Transfer*, 138(2), 022601.

Darcy, H., *Les Fontaines Publiques de la ville de Dijon*. Dalmont, Paris, 1856.

Das, S., S. Sneijders, N. G. Deen, and J. A. Kuipers (2018). Drag and heat transfer closures for realistic numerically generated random open-cell solid foams using an immersed boundary method. *Chemical Engineering Science*, 183, 260–274. ISSN 00092509. URL <https://doi.org/10.1016/j.ces.2018.03.022>.

de Carvalho, T. P., H. P. Morvan, D. M. Hargreaves, H. Oun, and A. Kennedy (2017). Pore-Scale Numerical Investigation of Pressure Drop Behaviour Across Open-Cell Metal Foams. *Transport in Porous Media*, 117, 311–336.

Delgado, J. M. P. Q. (2006). A critical review of dispersion in packed beds. *Heat Mass Transfer*, 42, 279–310.

Delgado, J. M. P. Q. (2007). Longitudinal and transversal dispersion in porous media. *Trans IChemE Part A, Chemical Engineering Research and Design*, 85, 1245–1252.

Della Torre, A., G. Montenegro, G. R. Tabor, and M. L. Wears (2014). CFD characterization of flow regimes inside open cell foam substrates. *International Journal of Heat and Fluid Flow*, 50, 72–82. ISSN 0142727X.

Diani, A., K. K. Bodla, L. Rossetto, and S. V. Garimella (2014). Numerical Analysis of Air Flow Through Metal Foams. *Energy Procedia*, 45, 645–652. ISSN 1876-6102. URL <http://dx.doi.org/10.1016/j.egypro.2014.01.069>.

Diani, A., K. K. Bodla, L. Rossetto, and S. V. Garimella (2015). Numerical investigation of pressure drop and heat transfer through reconstructed metal foams and

comparison against experiments. *International Journal of Heat and Mass Transfer*, 88, 508–515. ISSN 00179310. URL <http://dx.doi.org/10.1016/j.ijheatmasstransfer.2015.04.038>.

Dietrich, B. (2012). Pressure drop correlation for ceramic and metal sponges. *Chemical Engineering Science*, 74, 192–199. ISSN 00092509. URL <http://dx.doi.org/10.1016/j.ces.2012.02.047>.

Dietrich, B. (2013). Heat transfer coefficients for solid ceramic sponges-Experimental results and correlation. *International Journal of Heat and Mass Transfer*, 61(1), 627–637.

Dietrich, B., W. Schabel, M. Kind, and H. Martin (2009). Pressure drop measurements of ceramic sponges-Determining the hydraulic diameter. *Chemical Engineering Science*, 64, 3633–3640.

Du Plessis, J. P. (1994). Analytical quantification of coefficients in the Ergun equation for fluid friction in a packed bed. *Transport in Porous Media*, 16, 1189–207.

Du Plessis, P., A. Montillet, J. Comiti, and J. Legrand (1994). Pressure drop prediction for flow through high porosity metallic foams. *Chemical Engineering Science*, 49, 3545–3553.

Dukhan, N. (2006). Correlations for the pressure drop for flow through metal foam. *Experiments in Fluids*, 41, 665–672.

Dukhan, N. and K. P. Patel (2010). Entrance and exit effects for fluid flow in metal foam. *AIP Conference Proceedings*, 1254, 299–304.

Dukhan, N. and P. Patel (2008). Equivalent particle diameter and length scale for pressure drop in porous metals. *Experimental Thermal and Fluid Science*, 32, 1059–1067.

Edouard, D., M. Lacroix, C. P. Huu, and F. Luck (2008). Pressure drop modeling on solid foam: State-of-the art correlation. *Chemical Engineering Journal*, 144, 299–311.

Edouard, D., T. Truong Huu, C. Pham Huu, F. Luck, and D. Schweich (2010). The effective thermal properties of solid foam beds: Experimental and estimated temperature profiles. *International Journal of Heat and Mass Transfer*, 53(19), 3807–3816. ISSN 0017-9310. URL <https://www.sciencedirect.com/science/article/pii/S0017931010002309>.

Edwards, M. and J. Richardson (1968). Gas dispersion in packed beds. *Chemical Engineering Science*, 23(2), 109–123.

Edwards, R. J., M.F. (1968). Gas dispersion in packed beds. *Chem Eng Sci*, 23, 109–123.

Ergun, S. (1952). Fluid flow through packed column. *Chem. Eng. Prog.*, 48, 89–94.

Ergun, S. and A. Orning (1949). Fluid flow through randomly packed columns and fluidized beds. *Industrial & Engineering Chemistry*, 41, 1179–1184.

Evans, E. and C. Kenney (1966). Gaseous dispersion in packed beds at low Reynolds numbers. *TRANSACTIONS OF THE INSTITUTION OF CHEMICAL ENGINEERS AND THE CHEMICAL ENGINEER*, 44(6), T189.

Fourie, J. G. and J. P. Du Plessis (2002). Pressure drop modelling in cellular metallic foams. *Chemical Engineering Science*, 57(14), 2781–2789.

Fried, J. J. (ed.), *Groundwater Pollution* volume 4 of *Developments in Water Science*. Elsevier, 1975. URL <https://www.sciencedirect.com/science/article/pii/S0167564808710396>.

Fu, X., R. Viskanta, and J. P. Gore (1998). Prediction of effective thermal conductivity of cellular ceramics. *International Communications in Heat and Mass Transfer*, 25, 151–160.

Fuller, A. J., T. Kim, H. P. Hodson, and T. J. Lu (2005). Measurement and interpretation of the heat transfer coefficients of metal foams. *Proceedings of the Institution*

of Mechanical Engineers, Part C: Journal of Mechanical Engineering Science, 219(2), 183–191.

Garmeh, G., R. T. Johns, and L. W. Lake (2009). Pore-scale simulation of dispersion in porous media. *SPE Journal*, 14(4), 559–567. ISSN 1086055X.

Garrido, G. I., F. C. Patcas, S. Lang, and B. Kraushaar-Czarnetzki (2008). Mass transfer and pressure drop in ceramic foams: A description for different pore sizes and porosities. *Chemical Engineering Science*, 63, 5202–5217.

Ghosh, I. (2009). Heat transfer correlation for high-porosity open-cell foam.

Giani, L., G. Groppi, and E. Tronconi (2005). Mass-transfer characterization of metallic foams as supports for structured catalysts. *Industrial and Engineering Chemistry Research*, 44(14), 4993–5002. ISSN 08885885.

Goedecke, R., *Fluidverfahrenstechnik Grundlagen, Methodik, Technik, Praxis* volume 1. Wiley-VCH, Weinheim, Bergstr, 2011.

Grenstedt, J. L. and K. Tanaka (1999). Influence of cell shape variations on elastic stiffness of closed cell cellular solids. *Scripta Mater*, 40, 71–77.

Grosse, J., B. Dietrich, G. I. Garrido, P. Habisreuther, N. Zarzalis, H. Martin, M. Kind, and B. Kraushaar-Czarnetzki (2009). Morphological characterization of ceramic sponges for applications in chemical engineering. *Ind. Eng. Chem. Res.*, 48, 10395–10401.

Gunn, D. and C. Pryce (1969). Dispersion in packed beds. *Trans IChemE*, 47, T341–T350.

Habisreuther, P., N. Djordjevic, and N. Zarzalis (2009). Statistical distribution of residence time and tortuosity of flow through open-cell foams. *Chemical Engineering Science*, 64, 4943–4954.

Hackert, C. L., J. L. Ellzey, O. A. Ezekoye, and M. J. Hall (1996). Transverse dispersion at high peclet numbers in short porous media. *Experiments in Fluids*, 21, 286–290.

Han, N. W., J. Bhakta, and R. G. Carbonell (1985). Longitudinal and lateral dispersion in packed beds: effect of column length and particle size distribution. *AIChE J*, 31, 277–288.

Hiby, J. W. (1962). Longitudinal dispersion in single-phase liquid flow through ordered and random packings. *Interaction between Fluids and Particles, London Instn Chem Engrs*, 312–325.

Hsieh, W. H., J. Y. Wu, W. H. Shih, and W. C. Chiu (2004). Experimental investigation of heattransfer characteristics of aluminum-foam heat sinks. *Int. J. Heat Mass Transfer*, 47, 5149–5157.

Huang, J.-S. and L. Gibson (2003). Creep of open-cell voronoi foams. *Materials Science and Engineering: A*, 339, 220 – 226.

Humby, S., M. Biggs, and U. Tüzün (2002). Explicit numerical simulation of fluids in reconstructed porous media. *Chemical Engineering Science*, 57, 1955 – 1968.

Hutter, C., A. Zenklusen, R. Lang, and P. von Rohr. (2011). Axial dispersion in metal foams and streamwise-periodic porous media. *Chemical Engineering Science*, 66, 1132–1141.

Hwang, G. J., C. C. Wu, and C. H. Chao (1995). Investigation of Non-Darcian Forced Convection in an Asymmetrically Heated Sintered Porous Channel. *Journal of Heat Transfer*, 117(3), 725–732. ISSN 0022-1481. URL <https://doi.org/10.1115/1.2822636>.

Hwang, J. J., G. J. Hwang, R. H. Yeh, and C. H. Chao (2002). Measurement of interstitial convective heat transfer and frictional drag for flow across metal foams. *Journal of Heat Transfer*, 124(1), 120–129.

Ichimiya. (1999). A new method for evaluation of heat transfer between solid material and fluid in a porous medium. *ASME J. Heat Transfer*, 121, 978–983.

Inayat, A., H. Freund, A. Schwab, T. Zeiser, and W. Schwiger (2011a). Predicting the specific surface area and pressure drop of reticulated ceramic foams used as catalyst support. *Advanced Engineering Materials*, 13, 990–995.

Inayat, A., M. Klumpp, M. Lämmermann, H. Freund, and W. Schwieger (2016). Development of a new pressure drop correlation for open-cell foams based completely on theoretical grounds: Taking into account strut shape and geometric tortuosity. *Chemical Engineering Journal*, 287, 704–719. ISSN 13858947.

Inayat, A., J. Schwerdtfeger, H. Freund, C. Körner, R. F. Singer, and W. Schwiger (2011b). Periodic open-cell foams: Pressure drop measurements and modeling of an ideal tetrakaidecahedra packing. *Chemical Engineering Science*, 66, 2758–2763.

Incera Garrido, G., F. C. Patcas, S. Lang, and B. Kraushaar-Czarnetzki (2008). Mass transfer and pressure drop in ceramic foams: A description for different pore sizes and porosities. *Chemical Engineering Science*, 63, 5202–5217.

Innocentini, M. D., V. R. Salvini, A. Macedo, and V. C. Pandolfelli (1999). Prediction of ceramic foams permeability using Ergun's equation. *Materials Research*, 2(4), 283–289.

Johnson, G. W. and R. S. Kapner (1990). The dependence of axial dispersion on non-uniform flows in beds of uniform packing. *Chem Eng Sci*, 45, 3329–3339.

Kamath, P. M., C. Balaji, and S. P. Venkateshan (2013). Convection heat transfer from aluminium and copper foams in a vertical channel - An experimental study. *International Journal of Thermal Sciences*, 64, 1–10.

Kamiuto, K. and S. S. Yee (2005). Heat transfer correlations for open-cellular porous materials. *International Communications in Heat and Mass Transfer*, 32(7), 947–953.

Kaviany, M., *Principles of Heat Transfer in Porous Media*. Springer-Verlag, New York, 1995, second edition.

Kim, S. Y., B. H. Kang, and J. H. Kim (2001). Forced convection from aluminum foam materials in an asymmetrically heated channel. *International Journal of Heat and Mass Transfer*, 44(7), 1451–1454.

Kopanidis, A., A. Theodorakakos, E. Gavaises, and D. Bouris (2010). 3D numerical simulation of flow and conjugate heat transfer through a pore scale model of high porosity open cell metal foam. *International Journal of Heat and Mass Transfer*, 53(11-12), 2539–2550.

Krishnan, S., J. Y. Murthy, and S. V. Garimella (2006). Direct simulation of transport in open-cell metal foam. *Journal of Heat Transfer*, 128(8), 793–799.

Kumar, P. and F. Topin (2014a). The geometric and thermo-hydraulic characterization of ceramic foams: An analytical approach. *Acta Materialia*, 75, 273–286.

Kumar, P. and F. Topin (2014b). Investigation of fluid flow properties in open cell foams: Darcy and weak inertia regimes. *Chemical Engineering Science*, 116, 793–805. ISSN 00092509. URL <http://dx.doi.org/10.1016/j.ces.2014.06.009>.

Kumar, P. and F. Topin (2014c). Micro-structural Impact of Different Strut Shapes and Porosity on Hydraulic Properties of Kelvin-Like Metal Foams. *Transport in Porous Media*, 105, 57–81. ISSN 01693913.

Kumar, P. and F. Topin (2017). Predicting pressure drop in open-cell foams by adopting Forchheimer number. *International Journal of Multiphase Flow*, 94, 123–136. ISSN 03019322.

Kusner, R., John, and M. Sullivan, Comparing the weaire-phelan equal-volume foam to kelvin's foam. *In in [5]*. 1996.

- Kuwahara, F., M. Shirota, and A. Nakayama (2001). A numerical study of interfacial convective heat transfer coefficient in two-energy equation model for convection in porous media. *International Journal of Heat and Mass Transfer*, 44, 1153–1159.
- Lacroix, M., P. Nguyen, D. Schweich, C. P. Huu, S. Savin-Poncet, and D. Edouard (2007). Pressure drop measurements and modeling on sic foams. *Chemical Engineering Science*, 62, 3259–3267.
- lin Xia, X., X. Chen, C. Sun, Z. huan Li, and B. Liu (2017). Experiment on the convective heat transfer from airflow to skeleton in open-cell porous foams. *International Journal of Heat and Mass Transfer*, 106, 83–90.
- Liu, J. F., W. T. Wu, W. C. Chiu, and W. H. Hsieh (2006). Measurement and correlation of friction characteristic of flow through foam matrixes. *Experimental Thermal and Fluid Science*, 30, 329–336.
- Lu, T. J., H. A. Stone, and M. F. Ashby (1998). A-1998-(180)Heat transfer in open-cell metal foams .pdf. 46(10), 3619–3635.
- Lucci, F., A. Della Torre, J. von Rickenbach, G. Montenegro, D. Poulikakos, and P. Dimopoulos Eggenschwiler (2014). Performance of randomized Kelvin cell structures as catalytic substrates: Mass-transfer based analysis. *Chemical Engineering Science*, 112, 143–151. ISSN 00092509. URL <http://dx.doi.org/10.1016/j.ces.2014.03.023>.
- Maier, R. S., D. M. Kroll, R. S. Bernard, S. E. Howington, J. F. Peters, and H. Davis (2002). Enhanced dispersion in cylindrical packed beds. *Philos Trans R Soc Lond A*, 360, 497–506.
- Mancin, S., C. Zilio, A. Cavallini, and L. Rossetto (2010). Pressure drop during air flow in aluminum foams. *International Journal of Heat and Mass Transfer*, 53, 3121–3130. URL <http://dx.doi.org/10.1016/j.ijheatmasstransfer.2010.03.015>.

Mancin, S., C. Zilio, A. Diani, and L. Rossetto (2012). Experimental air heat transfer and pressure drop through copper foams. *Experimental Thermal and Fluid Science*, 36, 224–232. ISSN 08941777. URL <http://dx.doi.org/10.1016/j.expthermflusci.2011.09.016>.

Mancin, S., C. Zilio, A. Diani, and L. Rossetto (2013). Air forced convection through metal foams: Experimental results and modeling. *International Journal of Heat and Mass Transfer*, 62, 112–123. ISSN 00179310. URL <http://dx.doi.org/10.1016/j.ijheatmasstransfer.2013.02.050>.

Meinicke, S., T. Wetzel, and B. Dietrich (2017). Scale-resolved CFD modelling of single-phase hydrodynamics and conjugate heat transfer in solid sponges. *International Journal of Heat and Mass Transfer*, 108, 1207–1219. ISSN 00179310. URL <http://dx.doi.org/10.1016/j.ijheatmasstransfer.2016.12.052>.

Moon, C., H. D. Kim, and K. C. Kim (2018). Kelvin-cell-based metal foam heat exchanger with elliptical struts for low energy consumption. *Applied Thermal Engineering*.

Moreira, E. and J. Coury (2004a). The influence of structural parameters on the permeability of ceramic foams. *Brazilian Journal of Chemical Engineering*, 21(1), 23–33.

Moreira, E. A. and J. R. Coury (2004b). The influence of structural parameters on the permeability of ceramic foams. *Brazilian Journal of Chemical Engineering*, 21, 23–33.

Moreira, E. A., M. D. Innocentini, and J. R. Coury (2004a). Permeability of ceramic foams to compressible and incompressible flow. *Journal of the European Ceramic Society*, 24.

Moreira, E. A., M. D. M. Innocentini, and J. R. Coury (2004b). Permeability of ceramic foams to compressible and incompressible flow. *Journal of the European Ceramic Society*, 24, 3209–3218.

- Mujeebu, M. A., M. Z. Abdullah, A. A. Mohamad, and M. Z. Bakar (2010). Trends in modeling of porous media combustion. *Progress in Energy and Combustion Science*, 36(6), 627–650.
- Nakayama, A. (2014). A note on the confusion associated with the interfacial heat transfer coefficient for forced convection in porous media. *International Journal of Heat and Mass Transfer*, 79, 1–2. ISSN 00179310. URL <http://dx.doi.org/10.1016/j.ijheatmasstransfer.2014.07.088>.
- Nie, Z., Y. Lin, and Q. Tong (2017). Numerical investigation of pressure drop and heat transfer through open cell foams with 3D Laguerre-Voronoi model. *International Journal of Heat and Mass Transfer*, 113, 819–839. ISSN 00179310. URL <http://dx.doi.org/10.1016/j.ijheatmasstransfer.2017.05.119>.
- Nieh, T. G., K. Higashi, and J. Wadsworth (2000). Effect of cell morphology on the compressive properties of open-cell aluminum foams. *J. Mater. Sci. Eng.*, A283, 105–110.
- Ortega, J. M. (2013). A porous media model for blood flow within reticulated foam. *Chemical Engineering Science*, 99, 59–66. URL <http://dx.doi.org/10.1016/j.ces.2013.05.025>.
- Pallares, J. and F. X. Grau (2010). A modification of a Nusselt number correlation for forced convection in porous media. *International Communications in Heat and Mass Transfer*, 37(9), 1187–1190. ISSN 07351933. URL <http://dx.doi.org/10.1016/j.icheatmasstransfer.2010.07.014>.
- Parthasarathy, P., *Direct Pore Level Simulation of Heat Transfer in Open Cell Reticulated Porous Ceramics*. KIT Scientific Publishing, 2016.
- Parthasarathy, P., P. Habisreuther, and N. Zarzalis (2013). Evaluation of longitudinal dispersion coefficient in open-cell foams using transient direct pore level simulation. *Chemical Engineering Science*, 90, 242 – 249.

Parthasarathy, P., P. Habisreuther, and N. Zarzalis (2016). A study of pressure drop in reticulated ceramic sponges using direct pore level simulation. *Chemical Engineering Science*, 147, 91–99. ISSN 00092509. URL <http://dx.doi.org/10.1016/j.ces.2016.03.015>.

Parthasarathy, P., P. Talukdar, and V. Ratna Kishore (2009). Enhancement of heat transfer with porous/solid insert for a laminar flow of participating gas in a 3-d square duct. *Numerical Heat Transfer Part A*, 56, 764–784.

Pereira, J. C. F., I. Malico, T. C. Hayashi, and J. Raposo (2005). Experimental and numerical characterisation of transverse dispersion at the exit of a short ceramic foam inside a pipe. *Int. J. Heat Mass Transfer*, 48, 1–14.

Perkins, T. K. and O. C. Johnston (1963). A review of diffusion and dispersion in porous media. *Society of Petroleum Engineers Journal*, 3, 70–84.

Petrasch, J., P. Wyss, and A. Steinfeld (2007). Tomography-based monte carlo determination of radiative properties of reticulate porous ceramics. *J Quant Spectrosc Radiat Transf*, 105, 180–197.

Plessis, J. P. and J. H. Masliyah (1988). Mathematical modeling of flow through consolidated isotropic porous media. *Transp Porous Media*, 3, 145–161.

Prausnitz, J. M. (1958). Longitudinal dispersion in a pecked bed. *AIChE J*, 4, 14M–22M.

Rashidi, S., J. A. Esfahani, and A. Rashidi (2017). A review on the applications of porous materials in solar energy systems. *Renewable and Sustainable Energy Reviews*, 73, 1198–1210. ISSN 18790690. URL <http://dx.doi.org/10.1016/j.rser.2017.02.028>.

Regulski, W., J. Szumbariski, L. Łaniewski-Wołk, K. Gumowski, J. Skibiński, M. Wichrowski, and T. Wejrzanowski (2015). Pressure drop in flow across ceramic

foams—a numerical and experimental study. *Chemical Engineering Science*, 137, 320–337.

Richardson, J. T., Y. Peng, and D. Remue (2000). Properties of ceramic foam catalyst supports: pressure drop. *Applied Catalysis A: General*, 204, 19–32.

Richardson, J. T., D. Remue, and J. K. Hung (2003). Properties of ceramic foam catalyst supports: mass and heat transfer. *Applied Catalysis A: General*, 250, 319–329.

Roberts, A. and E. Garboczi (2001). Elastic moduli of model random three-dimensional closed-cell cellular solids. *Acta Materialia*, 49(2), 189 – 197.

Roberts, A. and E. Garboczi (2002). Elastic properties of model random three-dimensional open-cell solids. *Journal of the Mechanics and Physics of Solids*, 50, 33 – 55.

Sathurusinghe, P., K. Herath, and S. Herath, Elastic properties of open cell metallic foams using finite element analysis and homogenization technique. 2012.

Schiller, L. and Z. Naumann (1935). A drag coefficient correlation. *Ver. Deutsch. Ing.*, 77, 318–320.

Scott, D. S., W. Lee, and J. Papa (1974). The measurement of transport coefficients in gas-solid heterogeneous reactions. *Chem Eng Sci*, 29, 2155–2167.

Sepehri, E. and M. Siavashi (2022). Pore-scale direct numerical simulation of fluid dynamics, conduction and convection heat transfer in open-cell Voronoi porous foams. *International Communications in Heat and Mass Transfer*, 137(July), 106274. ISSN 07351933. URL <https://doi.org/10.1016/j.icheatmasstransfer.2022.106274>.

Sertkaya, A. A., K. Altinisik, and K. Dincer (2012). Experimental investigation of thermal performance of aluminum finned heat exchangers and open-cell aluminum foam heat exchangers. *Experimental Thermal and Fluid Science*, 36, 86–92.

Sinclair, R. J. and O. E. Potter (1965). The dispersion of gas in flow through a bed of packed solids. *Trans IChemE*, 43, T3–T9.

Sinn, C., J. Wentrup, G. R. Pesch, J. Thöming, and L. Kiewidt (2021). Structure-heat transport analysis of periodic open-cell foams to be used as catalyst carriers. *Chemical Engineering Research and Design*, 166, 209–219. ISSN 02638762.

Tadrist, L., M. Miscevic, O. Rahli, and F. Topin (2004). About the use of fibrous materials in compact heat exchangers. *Experimental Thermal and Fluid Science*, 28(2-3), 193–199. ISSN 08941777.

Taylor, G. (1953). Dispersion of soluble matter in solvent flowing slowly through a tube. *roceedings of the Royal Society A*, 219, 186–203.

Topin, F., J. P. Bonnet, B. Madani, and L. Tadrist (2006). Experimental analysis of multiphase flow in metallic foam: Flow laws, heat transfer and convective boiling. *Advanced Engineering Materials*, 8(9), 890–899. ISSN 14381656.

V. Chandra, S. Das, E. A. Peters, and J. A. Kuipers (2019). Direct numerical simulation of hydrodynamic dispersion in open-cell solid foams. *Chemical Engineering Journal*, 358(June 2018), 1305–1323. ISSN 13858947. URL <https://doi.org/10.1016/j.cej.2018.10.017>.

Wakao, N. and S. Noriaki, *Heat and mass transfer in packed beds*. Gordon and Breach Science Publishers, New York, 1982. ISBN 9780677058603.

Weaire, D. and R. Phelan (1996). The physics of foam. *Journal of Physics: Condensed Matter*, 8(47), 9519.

Whitaker, S., *Fundamental principles of heat transfer*. R.E. Krieger Pub. Co, Malabar, 1983. ISBN 0-89874-543-8.

William, T. (1887). On the division of space with minimum partitional area. *Acta Math.*, 11, 121–134.

Wu, Z., C. Caliot, G. Flamant, and Z. Wang (2011). Numerical simulation of convective heat transfer between air flow and ceramic foams to optimise volumetric solar air receiver performances. *International Journal of Heat and Mass Transfer*, 54(7-8), 1527–1537.

Xu, W., H. Zhang, Z. Yang, and J. Zhang (2008). Numerical investigation on the flow characteristics and permeability of three-dimensional reticulated foam materials. *Chemical Engineering Journal - CHEM ENG J*, 140, 562–569.

Yang, H., Y. Li, B. Ma, and Y. Zhu (2021). Review and a theoretical approach on pressure drop correlations of flow through open-cell metal foam. *Materials*, 14(12). ISSN 19961944.

Younis, L. B. and R. Viskanta (1993). Experimental determination of the volumetric heat transfer coefficient between stream of air and ceramic foam. *International Journal of Heat and Mass Transfer*, 36, 1425–1434.

Zafari, M., M. Panjepour, M. D. Emami, and M. Meratian (2015). Microtomography-based numerical simulation of fluid flow and heat transfer in open cell metal foams. *Applied Thermal Engineering*, 80, 347–354. ISSN 13594311. URL <http://dx.doi.org/10.1016/j.applthermaleng.2015.01.045>.

Zhu, H., J. Hobdell, and A. Windle (2000). Effects of cell irregularity on the elastic properties of open-cell foams. *Acta Materialia*, 48, 4893 – 4900.

PUBLICATIONS BASED ON THIS THESIS

Journal Papers

1. **Rambabu, S.**, Sriram, K. K., Chamarthy, S., & Parthasarathy, P. (2021). "A proposal for a correlation to calculate pressure drop in reticulated porous media with the help of numerical investigation of pressure drop in ideal & randomized reticulated structures". *Chemical Engineering Science*, 237, 116518. (**SCI Indexed, IF: 4.889**) [DOI:10.1016/j.ces.2021.116518](https://doi.org/10.1016/j.ces.2021.116518).
2. **Rambabu, S.**, & Parthasarathy, P. (2022). "A numerical study of forced convection in ideal and randomized reticulated porous structures and a proposal for a new correlation". *International Journal of Heat and Mass Transfer*, 184, 122292. (**SCI Indexed, IF:5.431**) [DOI:/10.1016/j.ijheatmasstransfer.2021.122292](https://doi.org/10.1016/j.ijheatmasstransfer.2021.122292).
3. **Rambabu, S.**, & Parthasarathy, P. (2022). "A numerical investigation to determine longitudinal dispersion coefficient in ideal and randomized reticulated porous structures using transient direct pore level simulation". *Chemical Engineering Science*, 274, 118664. (**SCI Indexed, IF: 4.889**) [DOI:10.1016/j.ces.2023.118664](https://doi.org/10.1016/j.ces.2023.118664).

Conference Papers

1. Madhukara S, **Rambabu, S.**, & Parthasarathy, P. "Validation and optimization of generalized porous media property relation for their use in volumetric solar receiver". 5th Indian conference on Applied Mechanics in Mechanical Engineering 2022, NIT Jamshedpur, Jharkhand.

CURRICULUM VITAE

SIDDAM RAMBABU

Guntur, Andhrapradesh, India - 522411

Contact Details: 99 59 57 60 42

Email: ramnitk111@gmail.com



EDUCATIONAL QUALIFICATIONS

(PhD): Mechanical Engineering

NITK, SURATHKAL, 2022

CGPA: 9.25

B.Tech: Mechanical Engg

SR University, Warangal, TG, 2011

81.6%

M.Tech: Mechanical (Thermal Engineering)

BVC Eng.college(A), Odalarevu, AP, 2015

81.50%

Diploma: Mechanical Engg

S.M.V.M.Polytechnic, Tanuku, AP, 2008

73.33%

WORK EXPERIENCE

- Assistant Professor at Aditya Engg. college, Surampalem, Kakinad, Andhrapradesh, India from January 2015 to December 2018

TECHNICAL SKILLS

- Strong technical background in Thermodynamics, Heat transfer, Fluid mechanics and CFD
- Skilled in Modelling software: Auto-CAD, Ansys-Design Modeler/Space claim
- Meshing software: ICEM-CFD and Fluent mesh
- Analytical software: Ansys Fluent and CFX
- Familiar with LINUX, MATLAB and Tec plot.

RESEARCH AREA INTEREST

- Fluid flow and Heat transfer in porous media
- Thermal storage and cooling applications
- Computational Fluid Dynamics

ACHIEVEMENTS

- Secured "Elite" Certificate in NPTEL for the course of "Laws of Thermodynamics".
- Ratified as an ASSISTANT PROFESSOR by Jawaharlal Nehru Technological University of Kakinada (2016-2017) Academic year.
- Qualified the GATE-2012 with a score of 384 .
- Achieved best result award for registering 100% pass percentage in ENGINEERING DRAWING" subject.
- Achieved best result award for registering 94% pass percentage in HEAT TRANSFER" subject.

WORKSHOP/PROGRAMS ATTENDED

- One-week High-End International Workshop on " High-Performance Computing & AI Predictive Tools in Fluid & Thermal" conducted by National Institute of Technology Rourkela in 2022.
- One-day NPTEL Workshop conducted by IIT Madras at IST JNTU Hyderabad in 2018.
- One-day National Workshop on "Recent advancements in mechanical engineering "conducted by JNTU Kakinada in 2017.

LANGUAGES

- Telugu, English and Hindi
-

